

**Vector boson fusion Higgs boson  
fiducial and differential cross-sections  
measured in the  $WW^* \rightarrow \ell\ell\nu\nu$  decay  
channel with the ATLAS detector**

A Dissertation

Presented to

The Faculty of the Graduate School of Arts and Sciences

Brandeis University

Department of Physics

Professor Gabriella Sciolla, Advisor

In Partial Fulfillment  
of the Requirements for the Degree  
Doctor of Philosophy

by

Laura Bergsten

July, 2020

This dissertation, directed and approved by Laura Bergsten's committee, has been accepted and approved by the Graduate Faculty of Brandeis University in partial fulfillment of the requirements for the degree of:

**DOCTOR OF PHILOSOPHY**

Eric Chasalow, Dean of Arts and Sciences

Dissertation Committee:

Professor Gabriella Sciolla, Chair

Craig Blocker

Alessandro Tricoli

©Copyright by

Laura Bergsten

2020

*Dedication*

# Acknowledgments

Thank all the people

# Abstract

**Vector boson fusion Higgs boson fiducial and differential  
cross-sections measured in the  $WW^* \rightarrow \ell\ell\nu\nu$  decay channel with  
the ATLAS detector**

A dissertation presented to the Faculty of  
the Graduate School of Arts and Sciences of  
Brandeis University, Waltham, Massachusetts

by Laura Bergsten

# Contents

<b>Abstract</b>	vii
<b>1 Introduction</b>	1
<b>2 Theory</b>	2
2.1 Standard Model . . . . .	2
2.2 LHC Physics/Phenomenology . . . . .	17
2.3 Brief history of SM tests . . . . .	25
2.4 Measurement motivation . . . . .	30
<b>3 The LHC and the ATLAS detector</b>	33
3.1 The Large Hadron Collider . . . . .	33
3.2 A Toroidal LHC Apparatus . . . . .	36
3.3 The High-Luminosity LHC and Inner Tracker (ITk) . . . . .	38
<b>4 Tracking and Isolation in ATLAS</b>	50
4.1 Jets . . . . .	51
4.2 Missing transverse energy . . . . .	56
4.3 Electrons . . . . .	60
4.4 Muons . . . . .	64
<b>5 Event Selection</b>	76
5.1 Data and Monte Carlo samples . . . . .	76
5.2 Object definitions . . . . .	76
5.3 Event selection . . . . .	76
<b>6 Backgrounds and Systematics</b>	77
6.1 Backgrounds . . . . .	77
6.2 Systematic uncertainties . . . . .	100

## *CONTENTS*

<b>7 Results</b>	<b>110</b>
7.1 Statistical analysis . . . . .	110
7.2 Unfolding . . . . .	112
7.3 Results and future measurements . . . . .	112
<b>8 Conclusions</b>	<b>113</b>

# **Chapter 1**

## **Introduction**

Introduction to the thesis. Explain what u'll see.

# Chapter 2

## Theory

The measurement at the heart of this thesis can only be understood within the context of a vast amount of preceding theoretical and experimental work. I have tried to condense and summarize key concepts that will motivate the central measurement's strategy and results. This chapter begins with a brief summary of the Standard Model itself, first describing fundamental particles and their forces before delving into a succinct mathematical formulation. Next, the chapter discusses history of the Standard Model and crucial tests of the theory up until current work at the LHC. The next section outlines some of the recent and current physics analyses at the Large Hadron Collider (LHC) with a focus on Higgs boson measurements. Finally, I'll introduce my thesis' main focus, fiducial and differential cross-section measurements of Vector-Boson-Fusion (VBF) Higgs decaying into two W-bosons.

### 2.1 Standard Model

The Standard Model is one of the most successful scientific theories to date. Its predictions encompass all of the visible universe and continue to undergo careful testing. The

## *CHAPTER 2. THEORY*

SM combines three forces- electromagnetic, weak, and strong - but it is not complete. One known force, gravity, is not included in the Standard Model and further questions, like an explanation for dark matter and dark energy, remain.

### **2.1.1 Particles and forces**

The particles we define in high energy physics are the most minute portions of observable matter. They are generally considered point-like, have no internal structure, and cannot be further split. Each particle we can define has a unique set of quantum numbers and its own anti-particle (with the same mass and spin, but opposite electrical charge and quantum numbers).

Particles can be sorted into a few distinct groups - first bosons, with integer spin, and fermions, with half-integer spin. Bosons are ‘force carriers’ meaning they are exchanged any time particles interact. Fermions are at the heart of all conventional matter. They can be split further into two categories- leptons and quarks. Quarks have fractional integer charge and interact strongly while leptons have integer charge and interact solely through the weak or electromagnetic forces. Both quarks and leptons are made of three generations of particles, each heavier and more unstable than the next. Charts showing quark/lepton families and their key quantum numbers are shown below in Figure 2.1. Each generation of quarks and leptons contains a particle doublet. Each lepton doublet contains a charged lepton and a neutrino while each quark doublet contains one  $+2/3$  charged particle and one with a  $-1/3$  charge. Each lepton and quark also has an anti-particle. All conventional, stable matter is made from the first generation of quarks and leptons.

There are four gauge bosons and one scalar boson predicted through the Standard Model. These correspond to three fundamental forces in nature (the fourth, gravity, is so small on the

## CHAPTER 2. THEORY

scale of particle interactions as to not be considered). The strongest force on the subatomic scale is the strong force- this is mediated by the gluon- and works primarily to bind quarks together to form composite particles like protons or neutrons. The electromagnetic force is about  $60\times$  weaker than the strong force and is mediated by the photon. This force accounts for all electric interactions like that between an electron and an atomic nucleus. Finally, the weak force ( $10^4\times$  weaker than the EM) facilitates  $\beta$ -decay and is mediated by massive  $W$  and  $Z$  bosons. The final boson predicted by the Standard Model is the Higgs boson. The only scalar boson, it has no charge or intrinsic spin. The Higgs gives mass to all other particles through Spontaneous Symmetry Breaking, which will be described in later sections.

### Standard Model of Elementary Particles

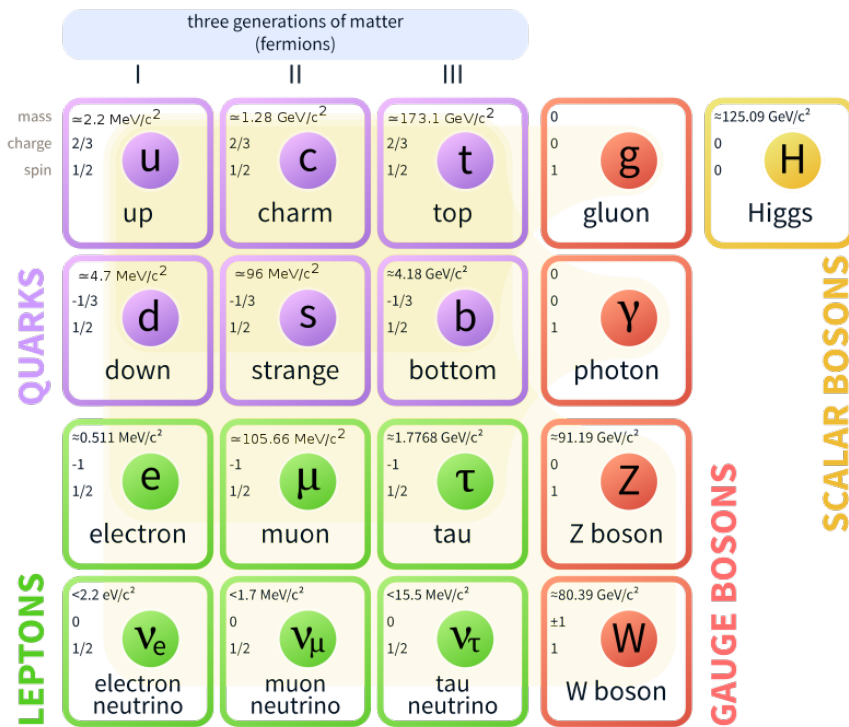


Figure 2.1: Three generations of quarks and leptons are shown along with all SM bosons [1]

## CHAPTER 2. THEORY

Photons are massless, spin-1 particles and mediate all electromagnetic interactions. They couple directly to any particle with electric charge- so quarks, leptons, and  $W/Z$  bosons but not neutrinos. Since the photon is massless, the electromagnetic force can operate on infinitely long scales but its force decreases with  $1/r^2$ .

Gluons are massless particles with no charge and spin-1. They couple to color charges, which are a property only of quarks and gluons. Each quark has one of three colors (RGB) while anti-quarks have "anti" versions of these. Colors are conserved 'charges' similar to electric charge. Quarks are never found alone as they couple so strongly to one another as to be confined in groups of two or three. These groups are "color-confined" meaning the quarks contain colors which add up to a color neutral sum. For instance, a two quark meson  $u\bar{u}$  may have colors R and anti-R while a three quark hadron  $uud$  (proton) may have colors R, G, and B. Gluons differ from photons in that they are not neutral in the charge they couple to. Gluons have two colors (8 total combinations) and can thus couple to each other. This makes the strong force distinct from the electromagnetic and has implications for long-distance interactions.

$W$  and  $Z$  bosons, unlike gluons and photons, are massive. However, like their other gauge boson counterparts, they have spin-1 and mediate a charge (weak).  $W^\pm$  mediates charged-current interactions which can violate flavor conservation between quarks and/or leptons and their neutrinos.  $Z^0$  mediates neutral-current interactions which conserve flavor.  $W^\pm$  bosons contain electric charge so can interact through EM as well. In addition,  $W$  and  $Z$  bosons contain weak charge (as do all fermions) so can self-couple as well as couple with all fermions.

The Higgs boson will be further motivated and described in later sections but suffice to say it's a massive spin-0 particle which couples to all particles with mass (including itself). It doesn't mediate any force but is still an integral part of the Standard Model.

## CHAPTER 2. THEORY

### 2.1.2 Gauge Invariance

According to Noether's theorem, for every continuous transformation of a field that leaves the Lagrangian invariant, there is a conserved current. In other words, symmetries found in physical theories lead to conservation laws (and vice-versa). The Standard Model is a gauge theory built on symmetries; all interactions between particles result from requiring the theory to be invariant under local gauge transformations. Each part of the Standard Model- from quantum electrodynamics (QED) to quantum chromodynamics (QCD) - is a gauge theory on its own. Each part has gauge invariance symmetries. In this section I'll step through the basic mathematic formalism for QED, QCD, and the combined electro-weak theory to illustrate the physical ramifications of gauge invariance and set the stage for the Higgs mechanism. The following sections are written with guidance from text [2].

### Quantum Electrodynamics

Quantum electrodynamics (QED) is the first, and simplest, physical gauge theory, describing how light and matter interact even under relativistic conditions. The theory produces extremely good agreement with experiment due to the success of perturbative QED calculations. Entire textbooks are dedicated to QED formalism and predictions. Here I will highlight only the effects of its local gauge invariance symmetry and generating the full QED Lagrangian beginning with the Dirac Lagrangian of a free fermion.

First, the Dirac Lagrangian describes a free fermion of mass  $m$

$$\mathcal{L} = i\psi\gamma^\mu\partial_\mu\psi - m\bar{\psi}\psi, \quad (2.1)$$

where  $\psi$  is a Dirac spinor and  $\gamma^\mu$  represent the Dirac matrices. To demonstrate local gauge

## CHAPTER 2. THEORY

invariance we need to transform

$$\psi(x) \rightarrow e^{i\alpha(x)}\psi(x) \quad (2.2)$$

where  $\alpha(x)$  depends on space and time arbitrarily. Directly substituting this into our Lagrangian shows that  $\mathcal{L}$  is not invariant, and the  $\partial_\mu$  term breaks this

$$\partial_\mu\psi \rightarrow e^{i\alpha(x)}\partial_\mu\psi + ie^{i\alpha(x)}\partial_\mu\alpha \quad (2.3)$$

In order to mandate the theory is invariant we need to change this term to the “covariant derivative”  $D_\mu$  which transforms

$$D_\mu\psi \rightarrow e^{i\alpha(x)}D_\mu\psi. \quad (2.4)$$

The “covariant derivative” must contain a vector field  $A_\mu$  and this field must transform so as to cancel with the unwanted part of the transformed  $D_\mu$  in order to transform as required by gauge invariance.

$$D_\mu \equiv \partial_\mu - ieA_\mu \quad (2.5)$$

where

$$A_\mu \rightarrow A_\mu + \frac{1}{e}\partial_\mu\alpha \quad (2.6)$$

Now the original Dirac equation is replaced with the following:

$$\mathcal{L} = \bar{\psi}(i\gamma^\mu\partial_\mu - m)\psi + e\bar{\psi}\gamma^\mu\psi A_\mu. \quad (2.7)$$

By requiring local gauge invariance we've introduced a gauge field  $A_\mu$  which couples to the Dirac particle just as the photon. In fact, if we take this as the photon gauge field and so add a kinetic energy term (which is also local gauge invariant!) we find the Lagrangian of

## CHAPTER 2. THEORY

QED.

$$\mathcal{L} = \bar{\psi}(i\gamma^\mu \partial_\mu - m)\psi + e\bar{\psi}\gamma^\mu\psi A_\mu - \frac{1}{4}F_{\mu\nu}F^{\mu\nu} \quad (2.8)$$

One can also see that adding a mass term to the Lagrangian for the new field ( $\frac{1}{2}m^2 A_\mu A^\mu$ ) would break gauge invariance, indicating the photon must be massless. From the free fermion Lagrangian, imposing local gauge invariance leads to the full interacting field theory of QED. This is not a curiosity but an essential component of the theory, and the use of local gauge symmetry in deriving particle interactions does not end here.

### Quantum chromodynamics

Quantum chromodynamics differs from QED in a few crucial ways. First, since quark color fields exist the QED  $U(1)$  gauge group is replaced with  $SU(3)$  and the free Lagrangian contains indices  $j$  to denote the three color fields:

$$\mathcal{L} = \bar{q}_j(i\gamma^\mu \partial_\mu - m)q_j. \quad (2.9)$$

QCD also carries three quark flavors, which will be ignored here for simplicity. The QCD group is non-Abelian since not all generators of the group commute with each other. These generators will be defined as  $T_a$  where  $a = 1, \dots, 8$  and are linearly independent traceless  $3 \times 3$  matrices (the Gell-Mann matrices  $\lambda_a$  are conventional). The local color phase transformation required is thus

$$q(x) \rightarrow e^{i\alpha_a(x)T_a}q(x) \quad (2.10)$$

We can consider an infinitesimal phase transformation as

$$\begin{aligned} q(x) &\rightarrow [1 + i\alpha_a(x)T_a]q(x), \\ \partial_\mu q &\rightarrow (1 + i\alpha_a T_a)\partial_\mu q + iT_a q \partial_\mu \alpha_a. \end{aligned} \quad (2.11)$$

## CHAPTER 2. THEORY

Just as in the QED example, the last line breaks the invariance of  $\mathcal{L}$  and we can proceed similarly by introducing a new gauge field (or in this case eight) called  $G_\mu^a$  which transform

$$G_\mu^a \rightarrow G_\mu^a - \frac{1}{g} \partial_\mu \alpha_a - f_{abc} \alpha_b G_\mu^c \quad (2.12)$$

The last term added here is to cope with the non-Abelian nature of QCD (that not all the generators  $T_a$  commute with each other). Just as in QED this invariance forms a covariant derivative:

$$D_\mu = \partial_\mu u + ig T_a G_\mu^a \quad (2.13)$$

Replacing the derivative in our Lagrangian and adding a gauge invariant energy term for each of the  $G_m u^a$  fields ( $\frac{1}{4} G_{\mu\nu}^a G_{\mu\nu}^a$ ) yields the final gauge invariant QCD Lagrangian:

$$\mathcal{L} = \bar{q}(i\gamma^\mu \partial_\mu - m)q - g(\bar{q}\gamma^\mu T_a q)G_\mu^a - \frac{1}{4} G_{\mu\nu}^a G_{\mu\nu}^a. \quad (2.14)$$

Just as in the QED case, imposing local color phase invariance produced a new interacting field (actually eight) with a coupling specified as  $g$ . These are the gluon fields and just like photons, local gauge invariance requires them to be massless. Unlike the QED case, this Lagrangian's new kinetic term includes self-interaction between the gauge bosons - another key feature of QCD that is mandated by local color phase invariance. Gluons themselves must carry color charge and so self-couple - the structure of these self coupling terms and their single coupling strength  $g$  are uniquely determined by gauge invariance.

### Electroweak unification

Thus far, I've summarized the theoretical backgrounds for symmetries (and so conserved quantities) in both quantum electrodynamics and chromodynamics. The weak force is the

## CHAPTER 2. THEORY

final Standard Model force and weak interactions are mediated by  $Z$  and  $W$  bosons. Unlike the gluons and photons of QCD and QED, these gauge bosons are massive. This is explained through spontaneous symmetry breaking of the electroweak force, which is outlined in the following section. Assuming that  $W/Z$  bosons are massive, the weak force can be combined with QED and a central electroweak force (with its associated symmetries) can be described.

The weak neutral current  $J_\mu^{NC}$  and weak charged currents ( $J_\mu$ ,  $J_\mu^\dagger$ ) can form a symmetry group for weak interactions. The charged currents correspond to the charged weak interaction through  $W^\pm$  bosons while the neutral current is associated with the  $Z^0$  boson.

$$\begin{aligned} J_\mu &= \bar{\nu}_L \gamma_\mu \nu_L, \\ J_\mu^\dagger &= \bar{e}_L \gamma_\mu \nu_L J_\mu^3 = \frac{1}{2} \bar{\nu}_L \gamma_\mu \nu_L - \frac{1}{2} \bar{e}_L \gamma_\mu e_L \end{aligned} \quad (2.15)$$

$L$  denotes that these are left-handed spinors and particle names denote associated Dirac spinors. The charged currents can be written as a doublet using the Pauli spin matrices  $\tau_i$  where  $\tau_\pm = \frac{1}{2}(\tau_1 \pm i\tau_2)$  and

$$\chi_L = \begin{bmatrix} \nu \\ e^- \end{bmatrix} \quad (2.16)$$

as

$$\begin{aligned} J_\mu^+(x) &= \bar{\chi}_L \gamma_\mu \tau_+ \chi_L, \\ J_\mu^-(x) &= \bar{\chi}_L \gamma_\mu \tau_- \chi_L, \\ J_\mu^3(x) &= \bar{\chi}_L \gamma_\mu \frac{1}{2} \tau_i \chi_L \text{ with } i = 1, 2, 3 \end{aligned} \quad (2.17)$$

The corresponding charge  $T^i = \int J_0^i(x) d^3x$  can be introduced so we have an  $SU(2)_L$  algebra

$$[T^i, T^j] = i\epsilon_{ijk} T^k \quad (2.18)$$

Unfortunately while these currents create an  $SU(2)$  group, they don't correspond with the

## CHAPTER 2. THEORY

weak neutral current symmetry in an obvious way. Unlike the charged currents, the neutral current has a right handed component. One clear way to resolve this is to add in the electromagnetic current, as its a neutral current with left and right-handed components.

$$j_\mu^{em}(x) = -e_R \bar{\gamma}_\mu e_R - e_L \bar{\gamma}_\mu e_L \quad (2.19)$$

so the the electromagnetic current  $j_\mu$  can be written using the coupling  $e$

$$j_\mu = ej_\mu^{em} = e\bar{\psi}\gamma_\mu Q\psi \quad (2.20)$$

with  $Q$  the charge operator and generator of the  $U(1)$  symmetry group of EM. In order to “save” the symmetry of the weak neutral current, we can define an electromagnetic current  $j_\mu^Y$ , or the weak hypercharge current, that is unchanged by  $SU(2)_L$  transformations. We define a weak hypercharge  $Y$  and its current  $j_\mu^Y$

$$\begin{aligned} Q &= T^3 + \frac{Y}{2}, \\ j_\mu^Y &= \bar{\psi}\gamma_\mu Y\psi \end{aligned} \quad (2.21)$$

The combined current

$$j_\mu^{em} = J_\mu^3 + \frac{1}{2}j_\mu^Y \quad (2.22)$$

now generates the symmetry group  $U(1)_\gamma$  and so the electromagnetic interaction and weak interaction are combined into one  $SU(2)_L \times U(1)_\gamma$  group. While unified in this way, the two forces still have independent coupling strengths. This brief introduction into electroweak unification is not the complete picture- EM and weak *interactions* still have to be unified. This is simple in the Standard model framework- electroweak currents just have to be coupled to vector bosons. In the electroweak  $SU(2)_L \times U(1)_\gamma$  group there is an isotriplet of vector

## CHAPTER 2. THEORY

fields  $W_\mu^i$  coupled with strength  $g$  to the weak isospin current  $J_\mu^i$  while a single vector field  $B_\mu$  is coupled to the weak hypercharge current  $j_\mu^Y$  with strength  $g'/2$ . The electroweak interaction can thus be defined:

$$-ig(J^i)^\mu W_\mu^i - i\frac{g'}{2}(j^Y)^\mu B_\mu. \quad (2.23)$$

This summary of the unified electroweak force will be the starting point for a derivation of the Higgs boson and an explanation for mass of the weak force's vector bosons (and all the fermions). The electroweak theory is unique in its calculability even at higher order scales. Because of this, theoretical uncertainties are relatively low and many deviations from theory could potentially be observed at current energy scales. The measurement central to my thesis probes for such discrepancies in electroweak theory. The mechanisms for this will be explained in the last section in this chapter.

### **Spontaneous Symmetry Breaking**

Unlike QED and QCD, the weak force is mediated by massive gauge bosons. Because of this, we can't apply the same gauge invariance prescription that we did in the last sections. If a mass term is added to the Lagrangian we break the gauge invariance we aimed to find. If we instead ignore the gauge invariance and add a mass term to the Lagrangian, all predictive power of the theory is lost due to unrenormalizable divergences. With "spontaneous symmetry breaking" we can gain massive gauge bosons while maintaining the integrity of the theory. In this section I first describe the "spontaneous symmetry breaking" mechanism in terms of an Abelian theory composed of complex scalar fields to illustrate the overall strategy. This mechanism is then applied to the non-Abelian electroweak theory to gain massive weak gauge bosons  $W^{+/-}$  and  $Z$  with the Higgs field appearing as a 'spontaneous' result.

## CHAPTER 2. THEORY

The Lagrangian for a  $U(1)$  gauge symmetry

$$\phi \rightarrow e^{i\alpha(x)}\phi \quad (2.24)$$

As in the QED case, we introduce a gauge field  $A_\mu$  and covariant derivative  $D_\mu = \partial_\mu - ieA_\mu$  to obtain the gauge invariant Lagrangian

$$\mathcal{L} = (\partial^\mu + ieA^\mu)\phi^*(\partial_\mu u - ieA_\mu)\phi - \mu^2\phi^*\phi - \lambda(\phi^*\phi)^2 - \frac{1}{4}F_{\mu\nu}F^{\mu\nu}. \quad (2.25)$$

In this example if  $\mu^2 > 0$  we gain back the QED Lagrangian for a charged scalar particle of mass  $\mu$  - with an additional self-interaction term. However, if we take  $\mu^2 < 0$  the potential  $V(\phi^*\phi) = \mu^2\phi^*\phi - \lambda(\phi^*\phi)^2$  now has a non-zero vacuum expectation value (v.e.v.) and there's a set of equivalent minima shown in Figure 2.2. Choosing one of these minima spontaneously breaks the potential's rotational symmetry. Next, we can perturbatively expand the field about a minima through

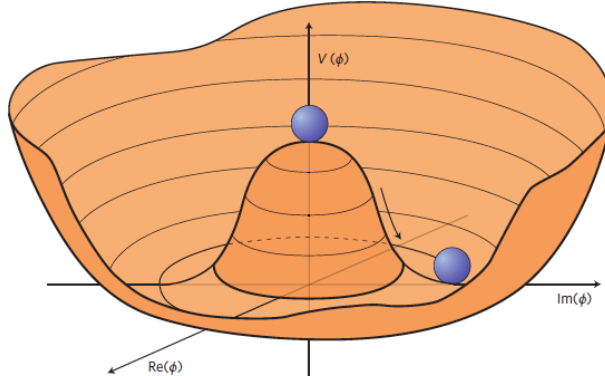


Figure 2.2: Higgs potential when  $\mu^2 < 0$ , choosing a minima spontaneously breaks the  $U(1)$  rotational symmetry [3]

## CHAPTER 2. THEORY

$$\phi(x) = \sqrt{\frac{1}{2}[\nu + \eta(x) + i\xi(x)]} \quad (2.26)$$

Substituting this perturbation gives the new Lagrangian

$$\mathcal{L}' = \frac{1}{2}(\partial_\mu \xi)^2 + \frac{1}{2}(\partial_\mu \eta)^2 - \nu^2 \lambda \eta^2 + \frac{1}{2}e^2 \nu_\mu^A A^\mu - e\nu A_\mu \partial^\mu \xi - \frac{1}{4}F_{\mu\nu} F^{\mu\nu} + \text{interaction terms.} \quad (2.27)$$

Three particles seem to emerge here: massless Goldstone boson  $\xi$ , massive vector  $A_\mu$  with  $m_A = e\nu$  and a massive scalar  $\eta$  with  $m_\eta = \sqrt{2\lambda\nu^2}$ . However, the number of particles does not correspond to the polarization degrees of freedom expected. A longitudinal polarization was added, creating an unphysical field, and injecting extra degrees of freedom. To eliminate the unphysical field we can substitute new set of fields:

$$\phi \rightarrow \sqrt{\frac{1}{2}(\nu + h(x))e^{i\theta(x)/\nu}} \quad (2.28)$$

and

$$A_\mu \rightarrow A_\mu + \frac{1}{e\nu} \partial_\mu \theta. \quad (2.29)$$

Introducing these substitutions, the Goldstone boson field disappears and the new Lagrangian is

$$\mathcal{L} = \frac{1}{2}(\partial_\mu h)^2 - \lambda \nu^2 h^2 + \frac{1}{2}e^2 \nu^2 A_\mu^2 - \lambda \nu h^3 - \frac{1}{4}\lambda h^4 + \frac{1}{2}e^2 A_\mu^2 h^2 + \nu e^2 A_\mu^2 h - \frac{1}{4}F_{\mu\nu} F^{\mu\nu}. \quad (2.30)$$

Here the degrees of freedom before our substitutions remains the same and a massive boson  $A_\mu$  is preserved along with a massive scalar  $h$ . The "Higgs mechanism" applied to a scalar field succeeded in creating a massive boson and determined the existence of a massive scalar boson. This same mechanism can be applied in the more complicated Standard Model electroweak field. Through electroweak symmetry breaking we not only gain massive gauge

## CHAPTER 2. THEORY

bosons and a massive scalar boson (the Higgs!) but also a way to calculate testable Standard Model predictions for many other quantities. We start with the  $SU(2) \times U(1)$  gauge symmetry of electroweak interactions derived in the previous section. In order to gain masses for three gauge bosons and keep the photon massless we need at least 3 degrees of freedom added and a simple choice is the  $SU(2)$  doublet of scalar fields  $\phi$ , with four fields in an isospin doublet of weak hypercharge  $Y = 1$ :

$$\mathcal{L} = (D^\mu \phi)^\dagger (D_\mu \phi) - \mu^2 \phi^\dagger \phi - \lambda (\phi^\dagger \phi)^2 \quad (2.31)$$

where  $\phi$  is a  $SU(2)$  doublet of complex scalar fields

$$\phi = \sqrt{\frac{1}{2}} \begin{bmatrix} \phi_1 + i\phi_2 \\ \phi_3 + i\phi_4 \end{bmatrix}. \quad (2.32)$$

Local gauge invariance can be achieved just as in the  $U(1)$  case with the covariant derivative, though now a bit more complex:

$$D_\mu = \partial_\mu + ig \frac{\tau_a}{2} W_\mu^a \quad (2.33)$$

with three gauge fields  $W_\mu^a(x)$  and  $a = 1, 2, 3$ . An infinitesimal transformation is defined

$$\phi(x) \rightarrow \phi'(x) = (1 + i\alpha(x) \cdot \tau/2)\phi(x) \quad (2.34)$$

so that we have a Lagrangian potential

$$V(\phi) = \mu^2 \phi^\dagger \phi + \lambda (\phi^\dagger \phi)^2. \quad (2.35)$$

Once again if we choose the conditions  $\mu^2 < 0$  and  $\lambda > 0$  there is rotational symmetry in

## CHAPTER 2. THEORY

our choice of vacuum expectation value. In this case choice of v.e.v. is limited. For the photon to remain massless, the vacuum must be invariant under  $U(1)$  (or electromagnetic) transformations, and not be charged in either direction (charge conservation). Thus the chosen minima to spontaneous break electroweak symmetry is

$$\phi_0 = \sqrt{\frac{1}{2}} \begin{bmatrix} 0 \\ \nu \end{bmatrix} \quad (2.36)$$

Next, substituting the vacuum expectation value  $\phi_0$  for  $\phi(x)$  and expanding perturbatively yields

$$\phi(x) \rightarrow \begin{bmatrix} 0 \\ \sqrt{\frac{1}{2}(\nu + H(x))} \end{bmatrix} \quad (2.37)$$

Fully expanding this term in the Lagrangian gives a complex and illuminating result, the Goldstone bosons have been consumed and there is only a Higgs field ( $H(x)$ ) remaining. Next, masses for the vector bosons are found from expanding one key parameter in the Lagrangian

$$|(-ig\frac{\tau}{2} \cdot W_\mu - i\frac{g'}{2}B_\mu)\phi|^2 = \frac{1}{8} \left| \begin{bmatrix} gW_\mu^3 + g'B_\mu & g(W_\mu^1 - iW_\mu^2) \\ g(W_\mu^1 + iW_\mu^2) & igW_\mu^3 + g'B_\mu \end{bmatrix} \begin{bmatrix} 0 \\ \nu \end{bmatrix} \right|^2. \quad (2.38)$$

Expanding further and substituting  $W^\pm = (W^1 \pm iW^2)/\sqrt{2}$  gives the result

$$|(-ig\frac{\tau}{2} \cdot W_\mu - i\frac{g'}{2}B_\mu)\phi|^2 = (\frac{1}{2}\nu g)^2 W_\mu^+ W^{-\mu} + \frac{1}{8}(W_\mu^3, B_\mu) \begin{bmatrix} g^2 & -gg' \\ -gg' & g'^2 \end{bmatrix} \begin{bmatrix} W^{\mu 3} \\ B^\mu \end{bmatrix}. \quad (2.39)$$

It is immediately clear that there is a mass-term for the  $W^\pm$ ,  $M_W = \frac{1}{2}\nu g$ . Masses for the photon and  $Z$ -boson are also apparent after expanding the last final term

$$\frac{1}{8}\nu^2(g^2(W_3^\mu)^2 - 2gg'W_\mu^3B^\mu + g'^2B_\mu^2) = \frac{1}{8}\nu^2(gW_\mu^3 - g'B_\mu)^2 \quad (2.40)$$

## CHAPTER 2. THEORY

and using the substitutions

$$\begin{aligned} A_\mu &= \frac{g'W_\mu^3 + gB_\mu}{\sqrt{(g^2 + g'^2)}} \text{ with } M_A = 0, \\ Z_\mu &= \frac{gW_\mu^3 - g'B_\mu}{\sqrt{(g^2 + g'^2)}} \text{ with } M_Z = \frac{1}{2}\nu\sqrt{(g^2 + g'^2)}. \end{aligned} \quad (2.41)$$

Now the Higgs field exists just as in the previous example and the theory contains a massive scalar boson and three massive vector gauge fields - for each of the  $W^\pm$  and  $Z$  bosons. The Goldstone bosons have been consumed, their degrees of freedom used to give mass to the vector bosons. Choosing a ground state and so breaking the gauge symmetry does not eliminate this symmetry altogether, since the theory is still renormalizable. Fermion masses can also be derived from their interactions with the Higgs boson using this Lagrangian. These derivations can be used to predict masses of bosons and fermions and couplings to the Higgs boson. It's important to note that though the Higgs mechanism gives mass to all fermions and massive gauge bosons, it doesn't determine what the Higgs mass ought to be. This is left as an empirical input to the theory that can then be used to calculate other observables.

The Standard Model has been proven over decades to be an incredibly robust theory and the Large Hadron Collider (LHC) is its key testing ground.

## 2.2 LHC Physics/Phenomenology

The Large Hadron Collider (LHC) is the foremost Standard Model testing ground and the proton-proton collisions recorded through ATLAS, CMS, ALICE, and LHCb have demonstrated the breadth and accuracy of the theory. Fermion and gauge boson masses and couplings, including the mass of the Higgs boson, have been measured with increasingly

## CHAPTER 2. THEORY

high precision. In the next chapter the mechanics of the LHC and ATLAS detector will be discussed, but first here I will introduce the motivations and observations of LHC physics. This section will begin with the mechanics of proton-proton collisions and their decay products, then discuss the concept of decay cross-sections and finally focus more closely on the Higgs boson and its properties.

The LHC was designed with one central goal- discover the missing Standard Model Higgs boson. The protons in the LHC collide at a center-of-mass energy of 13 TeV, but began at half that in 2010. The electroweak symmetry breaking scale was theoretically known to be between 100-1000 GeV and so probing at 7 TeV provided near certainty of finding either the Higgs or an inconsistency in the Standard Model. The motivation for a proton collider was multifaceted. Foremost, using the tunnels built for the electron-positron detector LEP with protons allows the collider to reach higher energies, as protons don't lose energy to synchrotron radiation at the same scale as electrons. However, proton collisions have added complexity from their component quarks. Each parton carries some fraction of the momentum of the proton described by parton distribution functions.

Figure 2.3 shows a proton-proton collision schematic. In this example the hard process comes from the up quark in each proton [4]. “Hardness” refers to the fraction of proton momentum involved in the collision. In contrast, “soft” collisions are those from remaining partons in each proton and usually involve low momentum transfer. These soft collisions are considered the underlying event shown in the figure 2.3. Parton scatter is the most common hard process at the LHC by far due to the high density of gluons in the proton and the scale of QCD couplings above electroweak coupling strength.

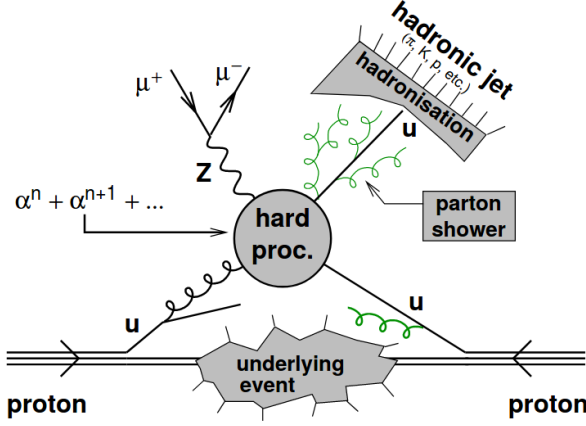


Figure 2.3: Example proton-proton collision with quark-gluon scattering and final state jet and Z-boson [4]

Quarks and gluons emitted from the high energy hard scatter do not appear in the detector directly. QCD, in one of its key differences to QED, becomes stronger with larger distances. As a parton reaches high enough energy, it will begin to radiate low energy gluons until resultant partons are able to bind into color-neutral hadrons. These hadrons are seen collimated in groups in the detector as “jets”. The energy and momentum of jets are considered reflections of the intial scattered partons. Various “jet algorithms” can be used to determine initial parton properties as reproducibly and accurately as possible. The jet algorithm used in this analysis will be described in detail in Chapter 3. However, it is important to note that the algorithm used by all LHC experiments- anti- $k_t$ - is collinear and infrared safe, or unaffected by small angle and soft scatterings that occur in a parton shower. Without these qualities, perturbation theory applied to the parton shower would find infinities at high orders.

Cross-sections (denoted  $\sigma$ ) measure the probability that a certain process will occur in the collision of two particles, in our case protons. In high energy physics cross-sections are

## CHAPTER 2. THEORY

measured in inverse femtobarns. A barn is the cross-sectional area of a uranium nucleus and was named to describe the large target area needed in order to have direct strikes on a nucleus. The name was inspired by the expression "couldn't hit the broad side of a barn". Inverse femtobarns are used to measure the number of particle collision events per femtobarn area of a target and quantifies time-integrated luminosity.

Hard scattering cross-sections in hadron-hadron collisions can be calculated using the QCD factorization theorem, and to leading-order these calculations are relatively simple. In the factorization theorem, developed by Drell and Yan, deep inelastic scattering parton model processes could apply to hadron-hadron collisions. The Drell-Yan process is the production of a massive lepton pair by quark-antiquark annihilation. According to the factorization theorem, a hadronic cross-section  $\sigma(AB \rightarrow \mu^+\mu^- + X)$  could be calculated by weighting the Drell-Yan sub-process cross-section  $\hat{\sigma}$  for  $\bar{q}q \rightarrow \mu^+\mu^-$  with parton distribution functions  $f_{q/A}(x)$  which come from deep inelastic scattering [5]:

$$\sigma_{AB} = \int dx_a dx_b f_{a/A}(x_a) f_{b/B}(x_b) \hat{\sigma}_{ab \rightarrow X} \quad (2.42)$$

where  $X$  represents the two resulting leptons and  $ab$  the two annihilated quarks. This parton model provides good agreement with measured cross sections and so allows understanding of particular hard scattering processes. Predictions for some key Standard Model processes are shown in Figure 2.4. Noting the logarithmic scales it's clear that the Higgs boson of mass 125 GeV is orders of magnitude more numerous at the LHC than the Tevatron and that certain high mass particles like the  $b$  quark and  $W/Z$  bosons are produced at the LHC at high levels [5]. In addition, the plot shows cross-sections of particular Higgs decay modes. These will be discussed next.

## CHAPTER 2. THEORY

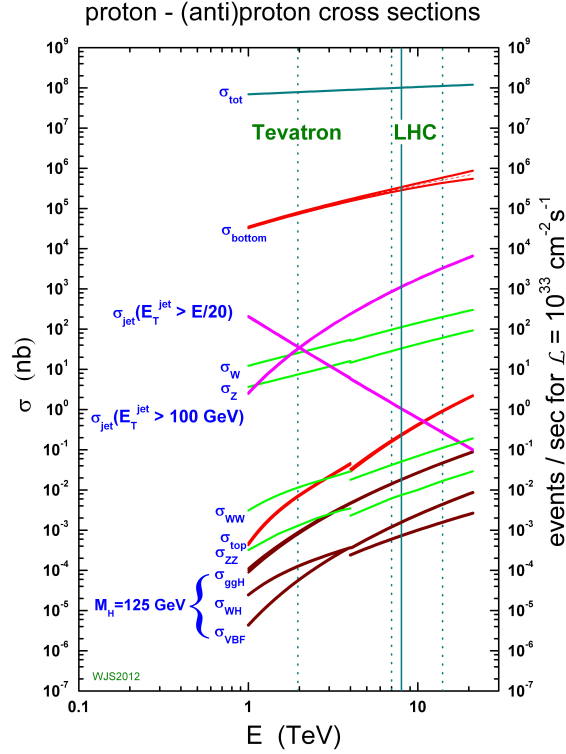


Figure 2.4: Predicted Standard Model cross-sections for the Tevatron and LHC [6].

Higgs production at the LHC occurs via four main processes: gluon-gluon fusion, vector-boson fusion, associated production with  $W/Z$  bosons, and associated production with top or bottom quarks. The Feynman diagrams for these processes are shown in Figure 2.5.

## CHAPTER 2. THEORY

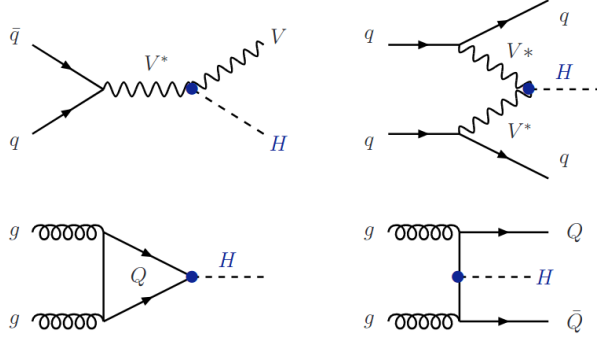


Figure 2.5: Feynman diagrams for the leading Higgs boson production modes at the LHC [7].

The LHC Cross-section Working Group produces predictions on cross-sections, branching ratios, and pseudo-observables for the Higgs boson. Four CERN reports bring together Higgs recommendations for current and planned LHC efforts [8]. Figure 2.6 shows the Higgs cross-section for the main production modes as a function of the Higgs mass and the collision center-of-mass energy. The Standard Model doesn't predict the Higgs mass, but with our experimental knowledge of that  $m_H$  is about 125GeV, the calculations can be focussed on the region of interest. Examining cross-section as a function of center-of-mass demonstrates the increase in statistics for events of interest that running the detector at higher energy levels can accomplish. It is also clear that gluon-gluon fusion Higgs production is the leading production mechanism by far. The cross-section is currently known at NNLO in QCD with NLO EW corrections. The second highest production cross-section is from vector-boson-fusion (VBF). As seen in the Feynman diagram, two outgoing quarks are produced in the interaction. These quarks produce two hard jets in the forward region, with the Higgs boson appearing between them. To leading order VBF Higgs production is solely electroweak and QCD corrections (calculated at NLO) have a smaller impact than in ggF. NLO EW corrections are also applied. As a result, VBF theoretical uncertainties are smaller

## CHAPTER 2. THEORY

than those on ggF. Vector boson associated Higgs production through a  $W/Z$  boson are less common than VBF but also dominated by electroweak processes with a small QCD correction (NNLO). Finally, associated production with top and bottom quarks is shown, though these are quite rare and have high NLO and NNLO QCD corrections.

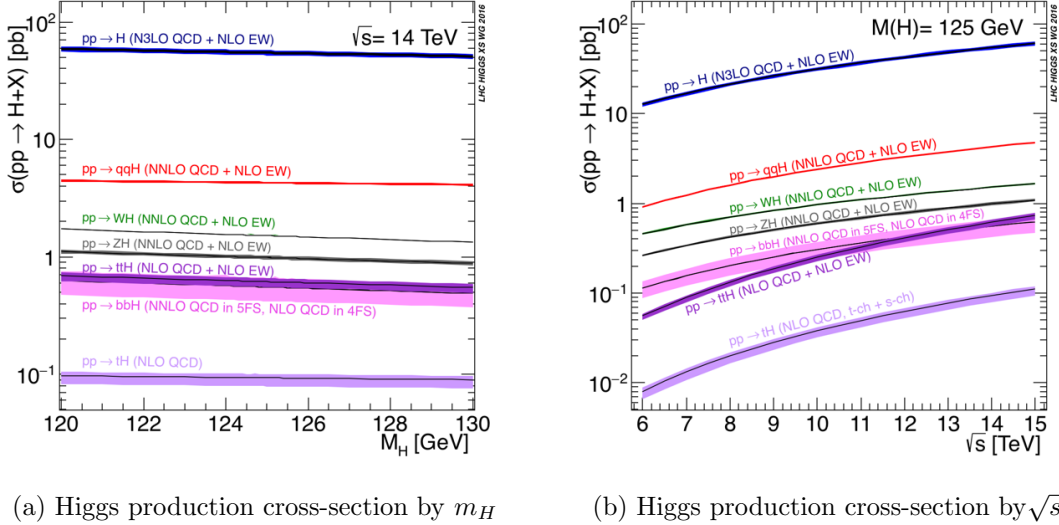


Figure 2.6: Higgs production cross-sections over Higgs mass at center-of-mass energy 14TeV (left) and over center-of-mass energy for a Higgs mass of 125GeV (right)[8]

Theoretical uncertainties shown as colored bars in 2.6 are calculated from choice of PDFs and renormalization and factorization scales. Parton distribution functions (PDFs) are described in more detail by the PDF4LHC working group [9]. This group performs studies of PDFs and their predictions at the LHC and makes recommendations for methods of estimating PDF uncertainties.

## CHAPTER 2. THEORY

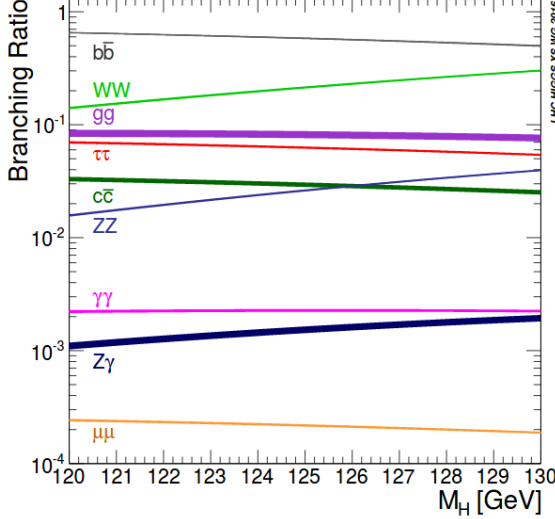


Figure 2.7: Predicted branching ratios for the Higgs boson at the LHC as a function of Higgs mass [8].

Since the Higgs boson couplings are directly proportional to the masses of each particle, the Higgs decays most readily into the heaviest particles possible. Figure 2.7 shows key decay mode branching ratios near the experimentally known Higgs mass. While the branching ratios demonstrate the relative abundance of each Higgs decay, these don't translate directly into their ease of discovery or measurement. The current status of Higgs boson coupling and cross-section measurements for each decay mode will be detailed in the next section. The Higgs boson discovery was made through a combination of searches in many channels though dominated by  $H \rightarrow ZZ^*$ ,  $H \rightarrow \gamma\gamma$ , and  $H \rightarrow WW$  [10]. This is because though other decay branching ratios are higher, like  $H \rightarrow b\bar{b}$ , the backgrounds associated with this decay are much higher. As previously mentioned, proton-proton collisions create large amounts of QCD jets that are difficult to discern from target hard QCD processes. Because of this, Higgs decays to quarks and gluons are particularly difficult and those with leptonic products (ZZ decays to 4 leptons, decays directly to photons, and WW decays to two leptons and two neutrinos) are much easier to reconstruct. As energy and integrated luminosity increased

## CHAPTER 2. THEORY

during LHC runs 1 and 2, measurements of even rare and background-heavy Higgs decay channels were able to be made. This thesis focuses on the decay of  $H \rightarrow W^+W^- \rightarrow \ell\nu\ell\nu$  through VBF production and in the last section of this chapter I will motivate the choice of these conditions for probing new physics beyond the SM.

### 2.3 Brief history of SM tests

Here I summarize key moments in the history of the development of the Standard Model and its experimental tests. I use both [11] and [12] as a guide.

The history of the Standard Model could start with any number of physicists well before the formalism of the theory itself. As far back as the fifth century B.C. philosophers posited that matter is composed of discrete “particles” in its most fundamental state. This idea was only tested beginning in the nineteenth century, when chemists were able to detect physical evidence of atoms and their structure. The first of the gauge theories, QED, was invented in the 1930s but only calculated to first order. Renormalization theory was invented simultaneously by Feynman, Schwinger, and Tomonaga in the 1940s. This made calculations of higher order QED results possible. Following this advancement, QED was verified experimentally with incredibly high precision.

Physicists next attempted to understand and formalize the other fundamental forces- strong and weak- in the same way. Symmetries for these theories were not as easy to find as that of QED and in 1954 the first new gauge theory for QCD was proposed by Shaw, Yang, and Mills. Though ultimately incorrect it led to proposals for a gauge theory of weak interactions by Schwinger in 1956 (unifying weak and electromagnetic interactions with photons and massive  $W^\pm$  bosons). Glashow added a fourth boson,  $Z$ , to the theory, but the problem of a broken symmetry necessary to give mass to the  $W/Z$  bosons remained.

## *CHAPTER 2. THEORY*

Spontaneous symmetry breaking was a known and tested concept, but its use in the theory led to unwanted massless “Nambu-Goldstone” bosons. Some thought this problem was inevitable in using SSB in the gauge theory. In 1964 Englert and Brout, then Higgs and a few months later Guralnik, Hagen, and Tribble all published papers with the same conclusion—the Goldstone theorem can be applied to gauge theories and massive bosons can “eat” the Nambu-Goldstone bosons to gain mass. This then creates a new scalar field whose particles are now termed Higgs bosons. A few years later Weinber unified these ideas into the electroweak theory we recognize today. The theory was confirmed many times over at experiments over the next decades.

While electroweak symmetry breaking and its implications were being understood in the 1960s, QCD was gradually being assembled. Experimental discoveries of a host of new particles led to Gell-Man and Zweig’s development of a theory that these were all composed of the same three base particles, “quarks”. Han and Nambu understood that an octet of colored gauge bosons, “gluons”, mediated the strong force through color interactions. In 1973 Gross, Wilczek, and Politzer demonstrated the asymptotic freedom of QCD, its weakness at short distances which allows perturbation theory to calculate high-energy interactions. The Standard Model as it is composed of electroweak dynamics and QCD, has been remarkably predictive but there is much it doesn’t explain. While theoretical physicists work to expand the Standard Model (or replace it entirely), experimentalists search for deviations from Standard Model predictions, which may be the next hint of entirely new physics.

Large amounts of experimental evidence for the predictive power of QED had amassed over time and by the 1970s high energy accelerators at CERN, Fermilab, Brookhaven and SLAC began making first measurements of predicted electroweak and QCD observables. In 1969 physicists at SLAC collided electrons and protons and found that electron scattering behaved as though the proton was made up of point-like particles, quarks. Electroweak

## CHAPTER 2. THEORY

theory's predicted new neutral weak current interaction between quarks and leptons was discovered at CERN and then Fermilab in 1973, giving evidence to electroweak unification. The  $W$  and  $Z$  bosons predicted by the theory with masses  $\approx 80\text{GeV}$  were discovered at SPS at CERN. This was the first proton-antiproton collider and with a center-of-mass energy of  $540\text{GeV}$ , it was the highest energy collider ever built. The collider was built for the main purpose of finding the predicted  $W$  and  $Z$  bosons and it succeeded in discovering both in 1983. Higher energy colliders like LEP at CERN and SLC at SLAC were able to produce millions of  $W$  and  $Z$  bosons and so test electroweak predictions with high precision. The theory continued to prove extremely accurate. QCD remains more difficult to test precisely as calculating QCD parameters theoretically is a computationally difficult task. However, evidence of QCD's accuracy has still accumulated. In 1978, SPEAR at DESY was able to indirectly detect the first gluon. The electron-positron collider produces two quarks that form two jets of particles with equal energy in opposite directions. QCD predicts that there will also be 3-jet events, where a gluon is radiated from one of the scattered quarks and forms the third quark. The strength of the strong interaction was first measured in 1978 and thereafter with more and more precision and has always followed QCD predictions. Quarks beyond the first generation (up, down) were discovered progressively in terms of their mass-strange, charm, bottom, and finally in 1995 the top. Similarly the muon was discovered well before the heavier tau-lepton. After the discovery of the top quark, the last Standard Model particle left undiscovered was the Higgs boson. Its mass is an input rather than a prediction to the Standard Model, but with the large amount of data taken at increasingly high energy colliders, experimentalists and theorists were confident that if it existed, it would be between  $100\text{GeV}$  and  $1\text{TeV}$ . In order to search for the Higgs boson, the Large Hadron Collider was planned and built at CERN. The collider and its largest all-purpose detector, ATLAS, are discussed in the next chapter.

## CHAPTER 2. THEORY

In 2012, the Higgs boson was discovered at the LHC in both the ATLAS and CMS detectors. After just one year of data at a center-of-mass energy of 7-8TeV, combined searches predominantly in the  $H \rightarrow ZZ^* \rightarrow \ell\ell\ell\ell$ ,  $H \rightarrow \gamma\gamma$  and  $H \rightarrow WW \rightarrow \ell\nu\ell\nu$  channels found a particle compatible with the Standard Model Higgs with a significance of 5.9 standard deviations at a mass close to 125 GeV. The LHC continued data-taking after the discovery with a new goal of measuring this new particle and its properties with accuracy and precision. The center-of-mass energy increased to 13TeV and more than 20 $\times$  the data used in the first discovery has now been recorded. Measurements of the Higgs boson are now numerous and incredibly precise, but the particle still doesn't deviate significantly from its theoretical expectation. While the Standard Model has proven a successful model of known interactions, there are many phenomena that it does not predict - from dark matter to gravity to neutrino masses. There must be physics beyond this theory and in continuing to probe new aspects of the model, the LHC may find deviations from the known forces or physics beyond the Standard Model.

The mass of the Higgs boson is measured through a combination of decay modes and in combination with CMS to be  $125.10 \pm 0.14$ GeV [1]. The latest combined Higgs cross-section measurement from ATLAS uses data from 2015-2017 and finds the production cross-sections (normalized to their Standard Model predictions) as shown in Figure 2.8. Branching ratios of relevant decay modes are also measured and are shown in Figure 2.9 multiplied by their cross-sections in each relevant production mode. Overall results demonstrate Higgs production and decay agree with SM predictions over a wide array of decay channels and production modes. The differences in theoretical and systematic uncertainty for certain decays (QCD heavy VBF  $H \rightarrow b\bar{b}$  in comparison to the leptonically decaying VBF  $H \rightarrow WW^*$ ) show how discernable backgrounds play a major role in the viability of a measurement, even when the branching ratio is high [13].

## CHAPTER 2. THEORY

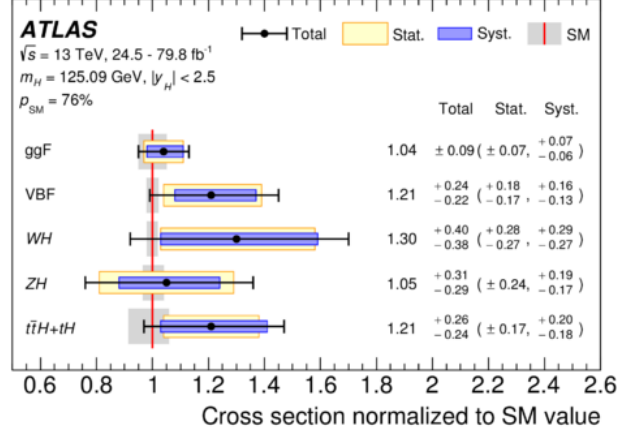


Figure 2.8: Production cross-sectios for ggF, VBF, VH, and  $t\bar{t}H + tH$  normalized to their SM predictions. Total, systematic, and statistical uncertainties are shown [13]

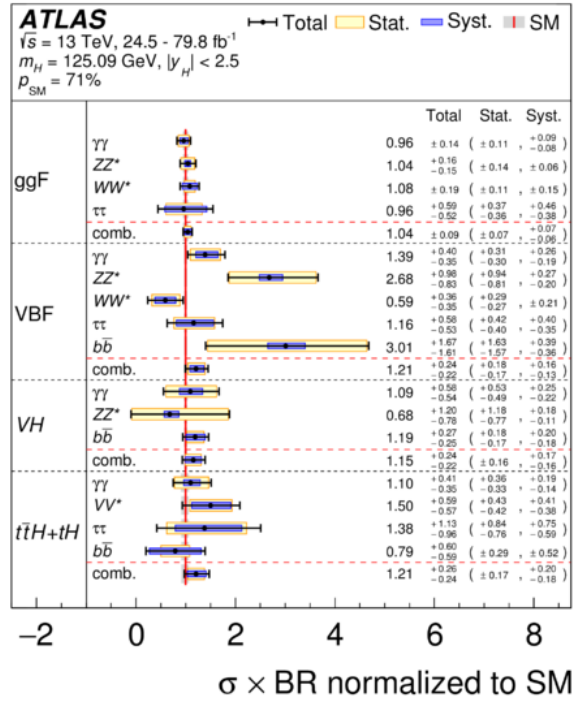


Figure 2.9: Branching ratios for measured Higgs decays normalized to their SM predictions. Total, systematic, and statistical uncertainties are shown [13]

## CHAPTER 2. THEORY

This thesis details my work on the differential measurement of VBF  $H \rightarrow WW^* \rightarrow \ell\nu\ell\nu$  decays. The clear sign of VBF Higgs production (2 jets recoiling in opposite high  $\eta$  directions, combined with the leptonically decaying  $W$  bosons) gives the decay a distinctive signature. This channel can be measured with high accuracy which may allow small deviations from theory to be visible. In addition, the differential cross-section measurement can probe higher order perturbative contributions to QCD or EW. Details on the particular motivations for this thesis' analysis will be outlined in the next section. The last ATLAS VBF  $H \rightarrow WW$  differential measurement was published in 2016 with  $20.3\text{fb}^{-1}$  at center-of-mass energy  $8\text{TeV}$  and measured only ggF Higgs boson production differential cross-sections [14]. This new measurement is presented with a  $4\times$  higher integrated luminosity and center-of-mass energy  $13\text{TeV}$  as well as new methodology for overall analysis strategy in order to take advantage of larger statistics. This is also to be the first ATLAS measurement focussing primarily on VBF Higgs differential cross-sections(?).

## 2.4 Measurement motivation

There are many reasons why the VBF  $H \rightarrow \ell\nu\ell\nu$  channel is particularly interesting to measure precisely. Since the  $W$  bosons decay leptonically, they create a clear signal in the detector which allows precise reconstruction of the hard processes. Further, the VBF production mode has a similarly clear signal with the two jets accompanying the decaying  $W$  bosons with a high  $\eta$  separation. The pseudorapidity of these jets and the rapidity between them are particularly sensitive to the electroweak symmetry breaking mechanism, so a differential cross-section measurement over these variables (along with other detailed and motivated in further sections) tests the Higgs mechanism. As previously stated, VBF Higgs WW decays have never been measured with the ATLAS detector, so this analysis

## CHAPTER 2. THEORY

introduces novel measurements. In Run-1 VBF  $H \rightarrow WW^* \rightarrow \ell\nu\ell\nu$  cross-sections were measured with an experimental uncertainty of  $\approx 30\%$  [13]. This new measurement uses the entirety of Run-2 data, with a factor of  $2.5\times$  higher statistics. This VBF differential  $H \rightarrow WW$  measurement uses new analysis techniques, higher statistics, and improvements in theoretical calculations to make an accurate probe of new physics within the electroweak symmetry breaking mechanism.

This thesis focuses on the VBF differential  $H \rightarrow WW$  measurement, but this measurement is the first piece to a larger goal beyond the scope of my Ph.D. Our group plans to make a simultaneous measurement of VBF  $H \rightarrow WW$  and VBF  $W + \text{jets}$  fiducial and differential cross-sections. The VBF  $W + jj$  production cross section is sensitive to the  $WWV$  vertex. In vector boson scattering, we expect (with minimal assumptions) that new physics ought to be at a scale above the current experiment. Effects from this type of new physics would simultaneously affect  $HWW$  and  $WWV$  vertices. In particular, dimension-6 operators affect VBF Higgs mechanisms and VBF  $W$  production, while the interplay of VBF and VBS mechanisms allows for the probe of dimension-6 and dimension-8 operators. Measuring fiducial and differential cross-section ratios (of VBF Higgs and  $Wjj$ ) enhances sensitivity to new physics because any new phenomena that simultaneously affect both vertices are suppressed and so sensitivity to the phenomena affecting just the  $WWV$  vertex (for example, anomalous quadruple-gauge couplings) is enhanced. VBF Higgs and  $Wjj$  productions are also characterized by final-states with two jets with similar kinematics. Because of this, the ratio of cross sections measurement allows for the cancellations of correlated systematic uncertainties. As both process are characterized by large ( $10\% - 20\%$ ) jet-related uncertainties, a reduction via the ratio cancellation would greatly improve the sensitivity to the VBF Higgs process and to the search for new phenomena. This VBF  $HWW$  measurement is the first part of the ratio of fiducial differential cross sections for VBF  $HWW$  and  $Wjj$ , which will

## *CHAPTER 2. THEORY*

set limits on EFT parameters, benefiting from enhanced sensitivity through the cancellation of correlated uncertainties.

# Chapter 3

## The LHC and the ATLAS detector

### 3.1 The Large Hadron Collider

The Large Hadron Collider (LHC) is a proton-proton storage ring operating at CERN and for last 13 years it has been the world's highest energy particle collider. The LHC first began operation in 2008 but following a magnetic quench incident it had to be repaired and adjusted. The first data-taking commenced in 2009 [15]. During the 9 years of LHC operation thus far, protons collided with increased center-of-mass energiy, approaching the design energy of 14TeV. Instaneous luminosity has also successively increased, surpassing design instantaneous luminosity of  $1 \times 10^{34} \text{cm}^{-2}\text{s}^{-1}$  in 2018 to reach  $2 \times 10^{34} \text{cm}^{-2}\text{s}^{-1}$ [16]. The overall data recorded in the ATLAS detector totals more than  $10^{16}$  collisions, and total collisions (not recorded) far surpasses this. Operation of the LHC has led to the most precise measurements of Standard Model constants yet including the coupling of the Higgs boson to bottom quarks [? ],  $W$  and  $Z$  bosons [17], [18], photons[19] and tau leptons [20]. The LHC has also facilitated searches over a wide parameter space, setting confidence level exclusion limits on masses of supersymmetric particles like squarks, gluinos and neutralinos

### CHAPTER 3. THE LHC AND THE ATLAS DETECTOR

[21].

The LHC is set to begin Run 3, in which design center-of-mass energy should be reached, in 2021. Following Run 3 detector upgrades will be made during a long shutdown. Then the High-Luminosity LHC (HL-LHC) will begin colliding protons with unprecedented  $10 \times$  LHC-luminosity in 2027 [22]. The HL-LHC and its goals will be explained further in later in this chapter. Suffice to say LHC-physics is progressing quickly and promises exciting developments in the near future.

In a brief explanation of the LHC operation, one could begin with the small volume of  $\approx 10^{11}$  protons that are accelerated. Linac 2 is the primary source of protons for CERN accelerators and has been since the early 1990s [23]. This injects protons at 50 MeV into the Proton Synchrotron Booster (PSB) where they are further accelerated to 1.4 GeV. Next they enter the Proton Synchrotron (PS) where the protons are separated into bunches with a spacing of 25 ns and are further accelerated to 25 GeV before being extracted to the Super Proton Synchrotron (SPS) where they reach 450 GeV. Finally these bunches of protons enter the LHC and are accelerated to their final energy of 6.5 TeV. Linac 2, PSB, PS, and SPS were all operational accelerators before being involved in the LHC apparatus though each had to be majorly upgraded to handle the energy and beam intensity required for LHC collisions [23].

The LHC layout mimics that of the Large Electron Positron collider (LEP) that was housed in the same tunnels. Figure 3.1 shows the positioning of each experiment on the LHC as well as injection systems and other features. Once proton bunches enter the LHC in two opposing beams they are accelerated with radio frequency (RF) systems. Located at Point 4 in the LHC schematic, the system consists of 16 RF cavities operating at twice the frequency of the SPS injector. RF cavities are metallic chambers containing oscillating electromagnetic fields, in the LHC this oscillation frequency is 400 Mz. The tuning of this

## CHAPTER 3. THE LHC AND THE ATLAS DETECTOR

frequency ensures that protons of the ideal energy are not accelerated further and simply maintain their momentum while particles arriving in an RF cavity slightly before or after will be decelerated or accelerated toward the ideal proton energy. This acceleration process can also be used to split beams of protons into discrete bunches, and this is first done with RF cavities in the PS. After proton bunches have circled the LHC approximately 1 million times (15 minutes), peak energy is reached and collisions can commence [24].

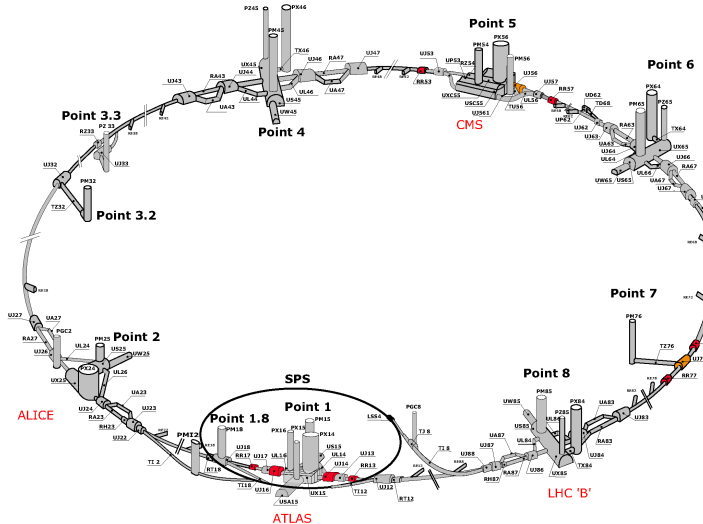


Figure 3.1: LHC layout [25]

Superconducting magnets in the LHC main dipoles create a magnetic field of  $\approx 8\text{T}$  to bend the proton beams into the circular path of the collider. Figure 3.2 shows the flux in a dipole cross-section. The opposing direction beamlines are shown centered and the flux is shown to be high (and directionally opposed) in the center of each beam. To maintain these fields, the magnets operate at below 1.9K. Pressurized superfluid helium chosen for its low viscosity and high specific heat cools the dipole magnets. Once the two LHC rings are filled from the SPS, center-of-mass energy of the beams increases until it reaches peak energy after about 28 minutes. Finally proton bunches separated by 25ns collide simultaneously in each

detector.

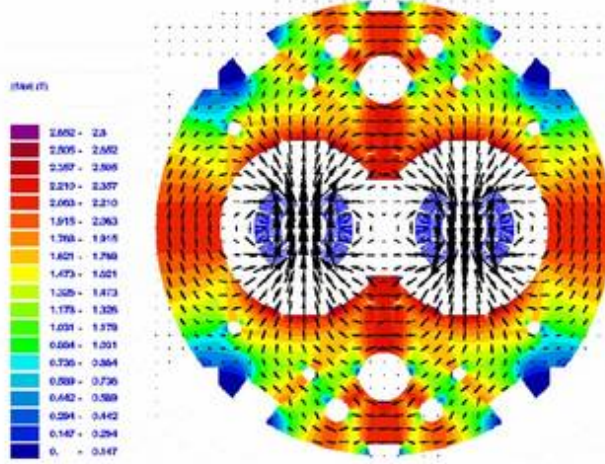


Figure 3.2: Flux within an LHC dipole cross-section [25]

## 3.2 A Toroidal LHC ApparatuS

The LHC creates proton-proton collisions at the rate and energy necessary for pushing the boundaries of particle physics, but identifying and reconstructing the tracks of such energetic particles is no mean feat. A Toroidal LHC ApparatuS (ATLAS) and the Compact Muon Solenoid (CMS) are multi-purpose detectors built to search for and measure a wide range of particle interactions and properties. Both experiments measured a particle consistent with the Higgs boson in 2012 and their agreement was a key verification of the discovery. The following sections describe each major component of the ATLAS detector so to highlight their necessity in the measurement of  $H \rightarrow WW \rightarrow e\nu\mu\nu$ .

ATLAS utilizes a coordinate system with its origin at the center of the detector (the “interaction point”) and has a z-axis along the beam pipe. The x-axis points from the interaction point to the center of the LHC ring, and the y-axis points upward. The experiment

### CHAPTER 3. THE LHC AND THE ATLAS DETECTOR

uses cylindrical coordinates  $(r, \phi)$  where  $\phi$  is the azimuthal angle around the beam pipe. The pseudorapidity and the transverse momentum are defined in terms of the polar angle  $\theta$  as  $\eta = -\ln(\tan(\theta/2))$  and  $p_T = p \sin \theta$ .

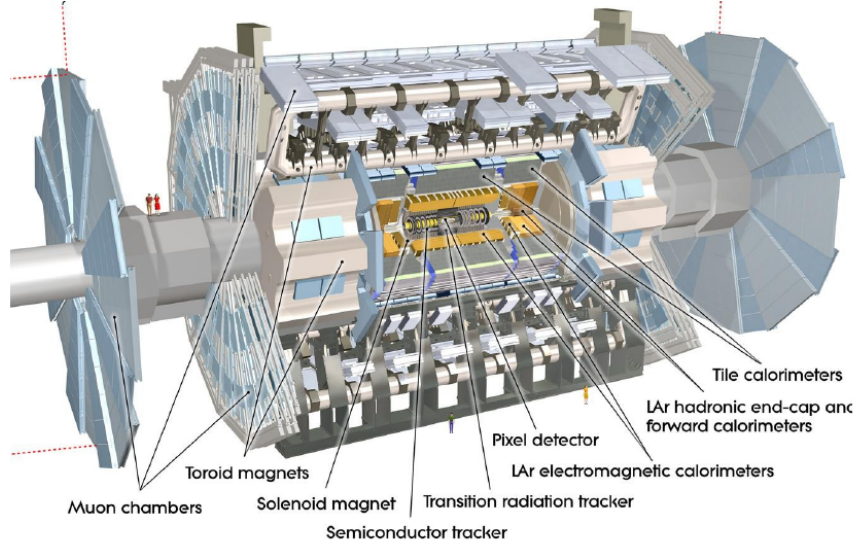


Figure 3.3: Computer-simulated ATLAS detector schematic [26]

The Inner Detector (ID) detects charged particles with  $|\eta| < 2.5$  operating in a 2T solenoidal field. It consists of 3 layers of pixel sensors, 4 layers of silicon strips, and 72 straw layers of transition radiation tracker modules. The ID describes particles closest to the interaction point and locates track parameters with great resolution due to high granularity [26].

The ATLAS detector contains 3 superconducting magnet systems- the barrel toroid, 2 end-cap toroids, and a central solenoid. The central solenoid provides a magnetic field for the inner detector while the toroids create a strong magnetic field for the muon detector. These magnet systems were built to create the largest possible uniform field (for increased momentum resolution on particle tracks) on a large volume enclosing the detector

### CHAPTER 3. THE LHC AND THE ATLAS DETECTOR

components. They also need to use as little material as possible so as to not unduly influence particles in the detector. The toroids in the barrel and endcap each have 8 coils and create a 4T magnetic field while the central solenoid creates a 2T magnetic field in the inner detector. Combined the magnet systems contain  $>100\text{km}$  of superconducting wire which are cooled to working temperatures below 5K [26].

The Muon Spectrometer precision chambers provide muon momentum measurements at a high resolution over a wide range of  $p_T$ . The MS consists of 3 layers of Monitored Drift Tube chambers covering  $|\eta| < 2.7$  and an inner layer of Cathode Strip Chambers with  $|\eta| > 2.0$ . In addition, it includes trigger chambers that contain 3 layers of Resistive Plate Chambers ( $|\eta| < 1.05$ ) and 3 layers of Thin Gap Chambers ( $1.05 < |\eta| < 2.4$ ). As the outermost subdetector, the MS provides precise muon momentum measurements along the muon trajectory and the muon chambers are located with a precision of under  $60\ \mu\text{m}$ . The MS also contains a system of three superconducting toroidal magnets each with eight coils providing a magnetic field with a bending integral of up to 6 Tm [26].

Calorimeters provide detailed information about the energy deposited as particles pass through. Electromagnetic calorimeters detect and halt the motion of electrons and photons while the hadronic calorimeter does the same for hadrons. Muons and neutrinos are able to pass through the calorimeters to the MS. The electromagnetic and hadronic calorimeters, made of liquid Argon and scintillating tiles respectively, are able to pass information from the location of energy deposits to the various identification and reconstruction algorithms [26].

## 3.3 The High-Luminosity LHC and Inner Tracker (ITk)

Though the LHC succeeded in its paramount goal of discovering the Higgs boson in 2012, its continuous operation at higher energy and luminosity has led to more rigorous measure-

### *CHAPTER 3. THE LHC AND THE ATLAS DETECTOR*

ments of Higgs boson properties as well as searches for new physics beyond the Standard Model. The LHC has been the leading high energy collider in terms of person power, energy, and scale for over a decade and will continue to be extremely important for understanding theoretical questions in the future. While more data collection is planned in Run-3 starting in 2021, new colliders and detectors take decades to design, develop and build, so the plans for the collider to take its place is well underway. The High Luminosity LHC will operate at an LHC-level energy (14TeV) and begin data-taking in 2026. The HL-LHC will begin with  $5 - 7 \times$  the luminosity of the LHC and will have a design instantaneous luminosity of  $10 \times$  the LHC, or  $12.6 \times 10^{-34} \text{cm}^{-2}\text{s}^{-1}$ . This huge increase in number of collisions requires massive upgrades to the LHC including new 11-12T superconducting magnet systems, compact superconducting cavities for beam rotation and phase control, and new technology beam collimation [? ]. This massive undertaking has been underway for many years already and has involved laboratories all over the world.

Just as the LHC had to be re-designed and built to create higher luminosity, so too do all the experiments on the LHC have to be redesigned to be able to interpret so many more collisions per second. The detectors must be built to withstand more radiation, as the increased collision rate also means a high radiation rate especially closest to the beamline. They also have to provide greater granularity to be able to reconstruct tracks with good enough resolution that individual tracks can be discriminated. Finally, they have to be able to deal with increased pile-up. Pile-up is caused by high numbers of collisions occurring at each bunch crossing. When there is a large amount of pile-up it becomes difficult to trace which particle tracks come from the same interaction point. Finally, the increased data in and of itself creates a complex problem for the detectors to solve, as briefly discussed previously, the trigger system must quickly choose which collision events may hold interesting events and store these. When there are more events happening near simultaneously these systems must

## CHAPTER 3. THE LHC AND THE ATLAS DETECTOR

make these decisions in real-time. New algorithms to speed up this process are necessary when there are an order of magnitude more events to sort through.

Detectors for high energy colliders are not built often- expensive and time-consuming to design and test, they're made to last at least a decade. I was lucky to have the opportunity to work on ATLAS detector research and development during the year I worked at Brookhaven National Laboratory during my Ph.D. Though my thesis isn't directly related to this work, it was formative and extremely interesting, so I'll touch on this work in the next section. Because I worked on the new ATLAS inner detector for the HL-LHC (termed Inner Tracker or ITk) I will discuss solely this sub-detector and the particular role I played in its assembly.

### 3.3.1 Inner Tracker (ITk)

The Inner Tracker is planned to be an all-silicon detector that will completely replace the current Inner Detector. While the current ID has been extremely successful during Runs 1 and 2 (and will certainly continue to be in Run 3), it does not have the capacity to withstand the radiation and pile-up conditions of the HL-LHC. The ITk is designed to operate for 10 years under an instantaneous luminosity of  $7.5 \times 10^{-34} \text{ cm}^{-2} \text{s}^{-1}$  with 25ns between bunch crossings. This will result in  $1,000 \text{ fb}^{-1}$  and average pile-up up to  $\langle \mu \rangle = 200$  [27]. The current solenoid magnet will remain in the detector with a 2T magnetic field. The ITk will consist of an innermost section with silicon pixels and an outermost section of silicon strips. The pixel detector will contain four barrel layers and six forward region disks, while the strip detector will contain five barrel layers and seven disks. The rapidity range matches the coverage of the Muon Spectrometer with  $|\eta| < 2.7$ . This layout is shown in ??.

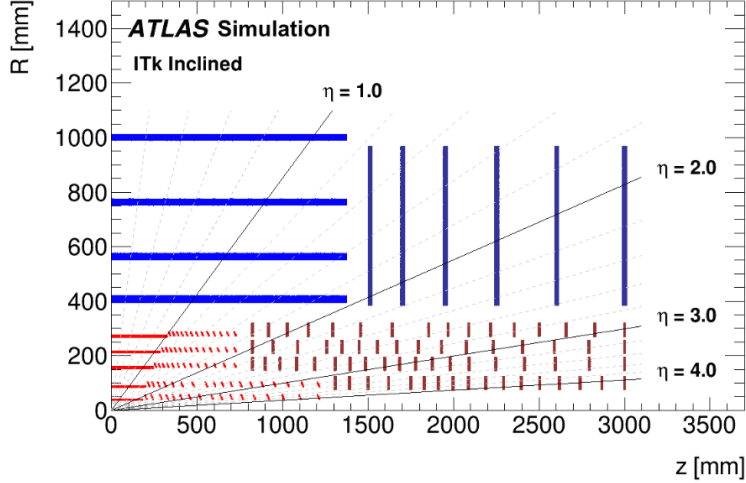


Figure 3.4: ITk layout as defined in ITk Technical Design Report [27]

### Building ITk Strip barrel staves

I spent 1.5 years of my Ph.D. at Brookhaven National Laboratory funded through a SCGSR Fellowship and was able to make key contributions to the ITk Strip barrel stave assembly effort. The goal of stave assembly is to precisely calibrate specified positions for silicon modules on carbon fiber stave cores and then glue them in place within a  $25\mu\text{m}$  tolerance. Brookhaven National Laboratory is responsible for assembly of half off all ITk staves ( 200) and their accurate assembly is necessary for the ITk to reduce uncertainty on track positions as well as to ensure a symmetric detector. At Brookhaven I was tasked with co-creating a stave assembly software system through LABView to automatically calibrate required module positions, apply a layer of adhesive gel, and guide a user in accurately placing a module into its specified location. This project was highly collaborative and evolved further after I left the laboratory, but the overall process remains unchanged.

The basic design of the Inner Tracker for both barrel and endcap components is the same - a carbon fiber core (containing titanium cooling pipes) is covered on each side with co-cured kapton service tapes. The carbon fiber core is designed to reduce overall radiation

### CHAPTER 3. THE LHC AND THE ATLAS DETECTOR

length and the similar design in the barrel and endcap adds to simplicity. Silicon modules are glued to stave cores. Similar radial silicon strip detectors have been used previously in both ATLAS and CMS but never covering so much fiducial area. The modules consist of one silicon sensor and one or two low-mass PCB’s (hybrid) which host ASICs. Module design has optimized producibility and low cost while maintaining readout goals. Overall module design is the same in barrel and endcap regions, while strip lengths and geometries vary. Components of a short-strip barrel module are shown in [3.5](#).

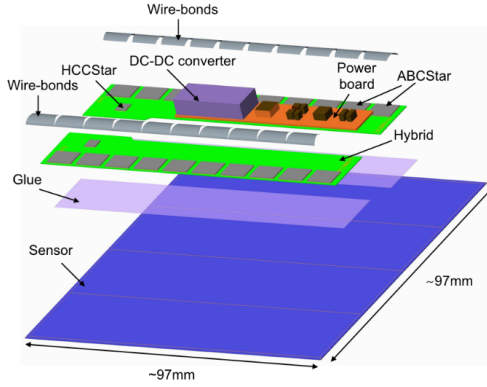


Figure 3.5: Short-strip barrel module components [\[27\]](#)

Each barrel stave core needs to be “loaded” with 14 modules, as shown in the assembled electrical prototype in [3.6](#). The placement of these modules needs to be accurate to below  $25\mu\text{m}$  so that the ITk models accurately demonstrate particle track positions. After the detector is assembled and commisioned tests will be undergo laser alignment to understand the exact positioning of the modules and staves but any module positioning out of specification will have adverse affects on track resolution during operation.

Brookhaven National Laboratory is one of two sites responsible for assembling barrel staves. Assembly procedures have been tested with the production of numerous prototypes including a thermomechanical double-sided stave and a fully operational electrical stave. The thermomechanical prototype was later used for various thermal tests, including IR imaging

### CHAPTER 3. THE LHC AND THE ATLAS DETECTOR

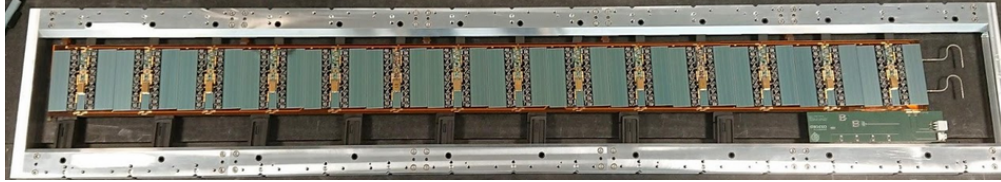


Figure 3.6: Electrical stave prototype at Brookhave National Laboratory

(documented in the next section). The electrical stave is currently undergoing tests for full electrical read-out. Stave assembly is composed of three main parts: system calibration, module placement, and survey of results.

Staves at BNL are assembled on a granite table housing an Aerotech XYZ Stage accurate to the micron level. The stage is equipped with a 10-megapixel camera that gives real-time feedback to a nearby computer and a glue dispenser. The stave assembly software system is implemented by a user who interacts with a LabView GUI and monitors progress. The stave is fixed to optical rails drilled into the table. In order to accurately place modules in their correct positions a series of calibrations need to be completed including camera calibrations to test the optimal working point, focus, and pixel-to-micron conversion. Next, the position of the stave with relation to the XYZ stage needs to be calibrated. Transforming coordinates of the XYZ stage to that of the stave and so specified coordinates for modules atop their carbon fiber cores requires locating a fixed point on the stave core as well as the angle of the stave relative to the XYZ stage. Pattern matching algorithms find the exact locations of particular features on the stave core and allow calculation of required positions for all modules based on specifications. Once specified module positions are calculated, calibrations are complete and it is time to apply glue and affix modules.

Next an epoxy (SE4445) is loaded into the glue dispenser on the XYZ-stage which is connected to a vacuum controlled by the LABView software system. The epoxy is automatically dispensed in lines to cover  $\approx 60\%$  of area under the module. Then the module

### CHAPTER 3. THE LHC AND THE ATLAS DETECTOR

is lifted with a custom-made “pick-up” tool which uses a vacuum applied to module corners to hold the module in place and move it to the needed position along the optical rails. Then using real-time feedback from the software system and its pattern matching algorithm, the user is directed on how to finetune module position using knobs on the “pick-up” tool. Markings etched in the silicon sensor at each corner are used to position the module accurately. The output of the module alignment GUI is shown in 3.7. When the module is within specifications it is lowered into position above the epoxy and held in place for 24 hours until the glue has completely dried.



Figure 3.7: GUI interface showing etched marking on module corner located in real-time to guide user on how to adjust module position

Finally after the glue has set a final survey of module positions is recorded using pattern matching to find positions of etched markings on each module corner. These results are saved into an ITk database and checked for any biases. After module placement on the stave is complete, the loaded stave is moved to another station in the lab for wirebonding so that all data from the modules can be read-out to stave-wide electronics. The module assembly system has been successful at placing modules accurately for all prototypes, achieving specification requirements for almost all modules. Results of the first prototype stave’s

### CHAPTER 3. THE LHC AND THE ATLAS DETECTOR

module placement are shown in 3.8. While a few module corners are slightly out of the ideal range, the majority are well within specifications. Throughout prototype assembly issues and inefficiencies were found and corrected. New hardware like an improved glue system and temperature monitoring were also added. The methods described continue to be in use now and will be utilized for the production of 200 ITk staves at BNL.

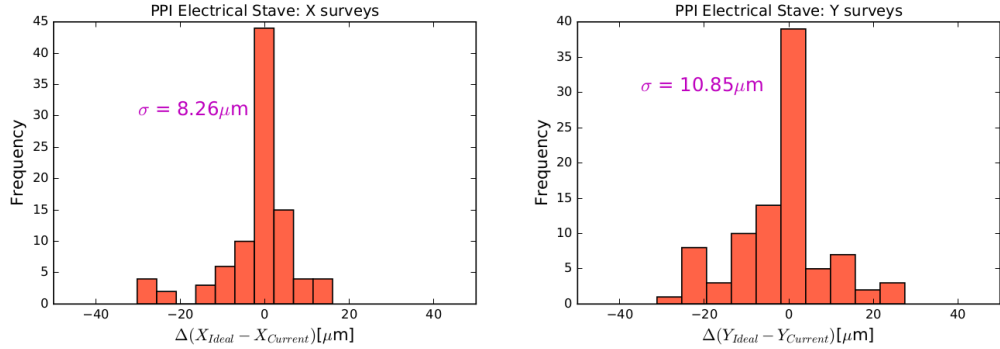


Figure 3.8: Histograms show difference between ideal and final position of each module corner. Left shows difference from specification in X and right in Y.

### IR Testing ITk Strip barrel staves

The first full US stave prototype was the thermo-mechanical stave built in the summer of 2017. Building this stave was the first test of stave assembly procedures and the results showed success. This stave was also assembled to test the thermal and mechanical properties of a fully loaded barrel stave. Multiple studies were conducted including thermal measurements using thermistors and IR imaging, thermal cycling and thermal shock tests, mechanical studies, and bending tests. I will give a short summary on IR imaging tests, as these were another focus of my time at BNL. First, the thermo-mechanical stave consists of 13 modules mounted on each side. The modules used are thermo-mechanical, which means that instead of the usual readout chips their hybrids have copper traces to mimic the power dissipation and location of the chips. The powerboard can vary the TM hybrid power dissi-

### *CHAPTER 3. THE LHC AND THE ATLAS DETECTOR*

pation of each module individually. In addition these modules each have three thermistors—one on the DC-DC converter, and one on each of two hybrids. The stave is powered by a custom End-of-Substructure (EoS) card which is attached to a RaspberryPi and Arduino and can power on or off each module.

Thermal testing of barrel staves had a few main goals: first, to compare with Finite Element Analysis (FEA) simulations and so test that all temperature trends are as we expect, to make sure that individual modules and their slightly modified assembly methods don't exhibit abnormal thermal behavior, and finally to check that loaded staves can cope with potential issues they might face during operation. I will highlight a few key results which demonstrate that each of these goals have been accomplished.

Thermal measurements were taken both through the mounted thermistors on each module and through IR imaging. IR imaging provides information about the entirety of the loaded stave, rather than at just a few module positions so provides a more complete picture. The loaded stave was spray-painted black with a high emissivity, low conductivity black paint since silicon is transparent to the IR camera spectrum ( $8\text{-}14\mu\text{m}$ ). In order to image the entire stave core, the IR camera was attached to rails above and pulled at a constant speed with an external motor as it recorded video. The frames were then stitched together into one image. A section of the painted stave is shown in [3.9](#).

FEA simulations for the thermal performance of a stave were completed by Prof. Graham Beck at Queen Mary University of London. These calculations quickly became intractable if convection was included so conditions of the stave and coolant were adjusted such that convective contributions were minimal or the total electrical power and power absorbed into the coolant were identical. At BNL we adjusted the coolant temperature until we saw this convective power minimization then recorded module temperatures under these conditions. These results were compared to the FEA simulations by averaging hybrid temperatures

### CHAPTER 3. THE LHC AND THE ATLAS DETECTOR

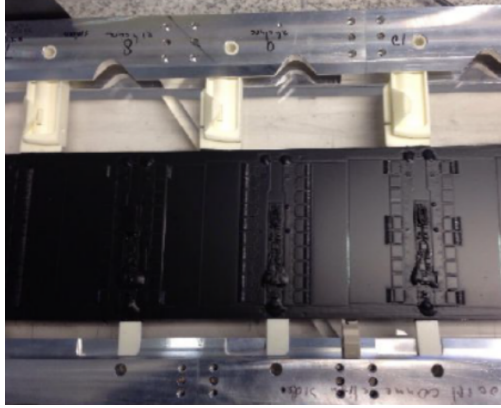


Figure 3.9: Portion of the thermo-mechanical stave after spray-painted for increased emissivity

recorded through IR imaging and recording NTC thermistor readings. These comparisons are shown in 3.10. The measurements show very good agreement with FEA calculations within 5% of the expected values.

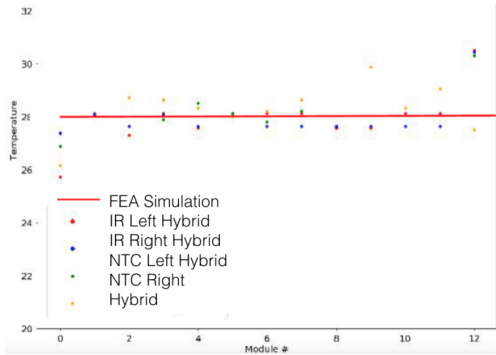


Figure 3.10: IR measurements, NTC thermistor measurements, and FEA simulations for the TM stave are compared. Agreement with FEA simulation within 5%

During module assembly some slight variations were tested including varying glue thickness below modules, glue curing time, and FEAST versions. Modules with these variations were noted and compared to those without at varying coolant temperatures and output power settings. Overall, no significant differences in module temperature change was observed for any of these assembly modifications. Fully loaded stave thermal properties are thus robust

### CHAPTER 3. THE LHC AND THE ATLAS DETECTOR

to assembly modifications like these. Figure 3.11 shows a full IR image of the fully loaded stave. It is clear that there are no obvious module-to-module variations in silicon, hybrid, or FEAST temperature. The module sensors increase in temperature as they get closer to the EoS, which is expected since it dissipates power to the stave.

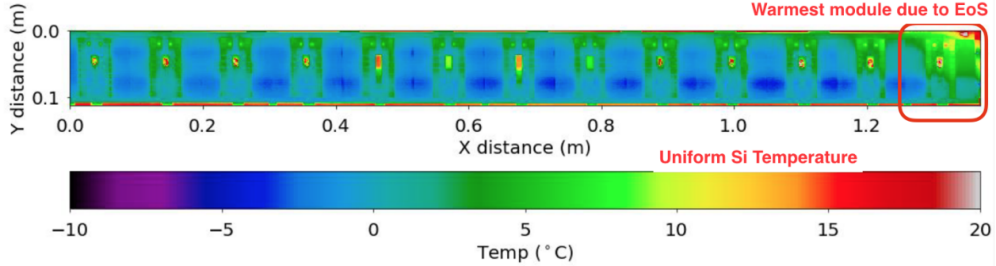


Figure 3.11: IR image of fully loaded thermo-mechanical stave

The thermo-mechanical stave was pushed to limits beyond what we would expect loaded staves to encounter during operation and never exhibited unexpected behavior. Thermal cycles, thermal shocks and bend tests showed the loaded stave robust to intense temperature variation and that the carbon fiber core is as stiff as it was prior to loading. Another test was how neighboring modules would perform if one module malfunctioned and went offline. Figure 3.12 shows temperature of each module when one of them (fourth to the left) turns off. The rest shows modules continue to operate normally and temperature changes from the unpowered module don't propagate very far. The second image in the figure shows the reverse of the stave when a module is powered off (fourth from the right). The temperature effects are greater directly below than adjacent to which is expected due to material differences.

My experiences on ATLAS detector upgrades for the HL-LHC provided context for the bulk of my thesis research. This project provided me with in depth and hands-on knowledge of the ATLAS detector and its component parts, as well as the scale of effort required to build new detector components. I have an abiding appreciation for the people and technology

### CHAPTER 3. THE LHC AND THE ATLAS DETECTOR

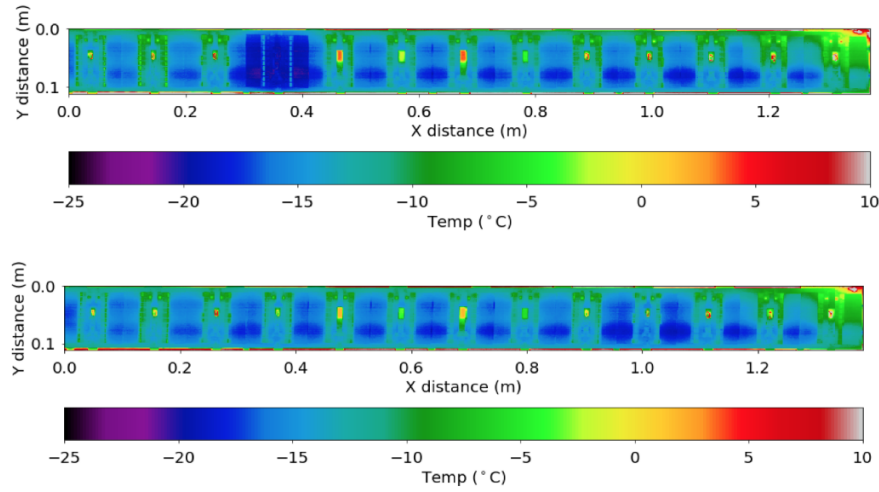


Figure 3.12: IR image of fully loaded thermo-mechanical stave

necessary for data-taking at the LHC both of which make measurements like the Higgs cross-section detailed in this thesis possible.

# Chapter 4

## Tracking and Isolation in ATLAS

The measurement of  $H \rightarrow WW^* \rightarrow \ell\nu\ell\nu$  cross-sections relies on the accurate determination of a number of physics objects within the detector primarily jets, missing transverse energy ( $E_T^{miss}$ ), electrons, and muons. The final state particles of this interaction consist of one electron, one muon, and two neutrinos, which appear as missing transverse energy in the detector since they cannot be directly detected. Because our search focuses on VBF production Higgs, we also require two jets in the final state. Each physics object has a dedicated performance group which is tasked with providing recommendations for reconstruction, identification, isolation and measurements of efficiency, scale, and resolution. Biases or omissions in any of these would severely impact the precision of our analysis and so understanding the uncertainties associated with each reconstructed object is critical. In this chapter I briefly outline the algorithms used for tracking and isolation and determining their relevant uncertainties for jets, missing transverse energy, electrons, and muons. Particular attention will be paid to muons as I spent a significant amount of time working in the Muon Performance Group applying and validating corrections to muon momentum scale and resolution.

## 4.1 Jets

Quarks and gluons emitted from high energy hard scattering do not appear in the detector directly. As quarks and gluons reach high enough energy, low energy gluons are radiated until partons are able to bind into color-neutral hadrons. These hadrons are seen collimated in groups as “jets”. Their energy and momentum are used in physics analyses as proxies for the initial scattered partons. Jet calibration seeks to determine jet energy scale and jet energy and angular resolution as accurately as possible. Pile-up presents the main difficulty in jet calibration - multiple interactions occurring in the detector at once creates significant, often hadronic, background. The hard interaction of interest must be separated from pile-up background (which is most often soft). During Run-1 the ATLAS experiment reconstructed jets using either only the calorimeter or the tracker, though most often the calorimeter. Topological clusters of calorimeter cells (topo-clusters) were used to trace jet tracks. At the end of Run-1, the jet energy scale (JES) correction factor used to calibrate jets to the particle level was re-calculated using additional track information from the Inner Detector and Muon Spectrometer, which greatly improved jet resolution [28].

Beginning in Run-2, a new algorithm for jet reconstruction took advantage of the improvements shown in Run-1 by including information from the tracker. ‘Particle flow’ uses the tracker’s higher momentum resolution for low-energy charged particles and its greater angular resolution of single charged particles. This is complemented by the calorimeter’s ability to reconstruct both charged and neutral particles and the calorimeter’s higher energy resolution for high energy physics objects. The calorimeter also has an extended acceptance so in the forward region only calorimeter topo-clusters are used. One potential difficulty with the ‘particle flow’ algorithm is the possibility for double counting particles if each tracker reconstructed jet isn’t correctly matched to its calorimeter signal. This is avoided in the

## CHAPTER 4. TRACKING AND ISOLATION IN ATLAS

algorithm through the condition that if a particle's track measurement is used, its corresponding energy must be subtracted from the calorimeter measurement. The success of the algorithm in removing only energy deposits from the tracked jet represents a key criteria for its overall performance [29].

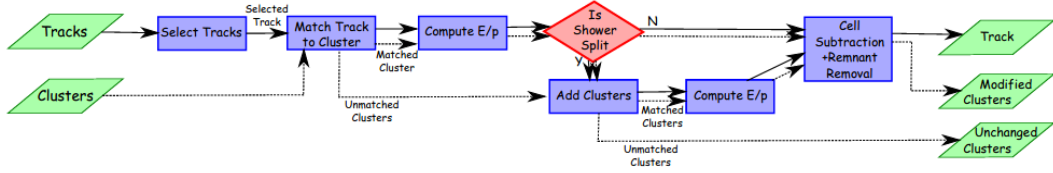


Figure 4.1: Flow chart of the particle flow algorithm beginning with track selection and ending with charged particles and changed/unchanged topo-clusters [29].

Topo-clusters are described by two main properties -  $\epsilon$ , which represents the fraction of true energy deposited in the cluster out of the total true energy deposited in all topo-clusters for that object and  $\rho$ , the purity or fraction of a particle's true energy which lies within the topo-cluster. High  $\rho$ , high  $\epsilon$  topo-clusters separate out contributions from different particles and so are easier to apply hadronic shower subtraction [29].

Jet tracks need to meet strict criteria to be considered. These include at least nine hits in silicon detectors, no missing Pixel hits,  $\eta < 2.5$ , and  $40 > p_T > 0.5\text{GeV}$ . These are referred to as a “tight” selection. Tracks which obey these criteria and do not deposit enough energy to create topo-clusters are still included. High  $p_T$  tracks are excluded because their poor isolation. In addition, tracks which are identified as electrons or muons are excluded [29].

With topo-clusters and tracks assembled, the algorithm next must match each to one another. Topo-clusters are ranked through the distance metric

$$\Delta R' = \sqrt{\left(\frac{\Delta\phi}{\sigma_\phi}\right)^2 + \left(\frac{\Delta\eta}{\sigma_\eta}\right)^2} \quad (4.1)$$

## CHAPTER 4. TRACKING AND ISOLATION IN ATLAS

where  $\sigma_\phi$  and  $\sigma_\eta$  denote angular topo-cluster widths. A requirement that  $E^{clus}/p^{trk} > 0.1$  is applied so that the energy of the topo-cluster must contain more a significant portion of the energy of the track. This requirement rejects about 30–40% of the incorrect topo-clusters at  $p_T > 5\text{GeV}$  (this is less pronounced at lower  $p_T$  and very rarely rejects the correct cluster). Distance selection is made such that the closest topo-cluster to each track in  $\Delta R'$  is taken to be the correct match. This is very successful at  $p_T > 5\text{GeV}$ . If no topo-cluster is within a cone of  $\Delta R' = 1.64$  it is assumed the particle did not form a topo-cluster in the calorimeter [29].

Topo-clusters are thus matched to particle tracks and next the energy the particle deposits must be subtracted from the calorimeter. The average energy deposited by a particle with momentum  $p^{trk}$  is given  $\langle E_{dep} \rangle = p^{trk} \langle E_{ref}^{clus}/p_{ref}^{trk} \rangle$  where  $\langle E_{ref}^{clus}/p_{ref}^{trk} \rangle$  is calculated using single-particle samples without pile-up by summing topo-cluster energies within  $\Delta R = 0.4$  about the track position. These are calculated at varying  $p_T$  and  $\eta$  values to capture effects from detector geometry and shower development. Particles often split their energy between multiple topo-clusters and this can be determined through the significance of the difference between expected energy and that of the matched topo-cluster. If significance is below -1, a split shower recovery procedure runs: topo-clusters within a cone of  $\Delta R = 0.2$  about the track position are considered to be matched to the track. This new full set of matched clusters is considered for energy subtraction [29].

Energy subtraction is performed cell-by-cell (unless  $\langle E_{dep} \rangle$  is greater than the energy of the total matched topo-clusters, in which case they are all removed). Rings are formed in  $\eta, \phi$  about the extrapolated track and are one calorimeter cell wide. The average energy density in each ring is computed and the ring with the highest energy density is subtracted first. This continues to lower density rings until  $\langle E_{dep} \rangle$  is reached. Finally, after cell-by-cell subtraction, remnant energy clusters are removed if they're considered purely from shower

## CHAPTER 4. TRACKING AND ISOLATION IN ATLAS

fluctuations and otherwise remain. Ideally now the set of selected tracks and remaining topo-clusters together represent the reconstructed event without double counting between the subdetectors. An example display of particle flow events is shown in Figure 4.2

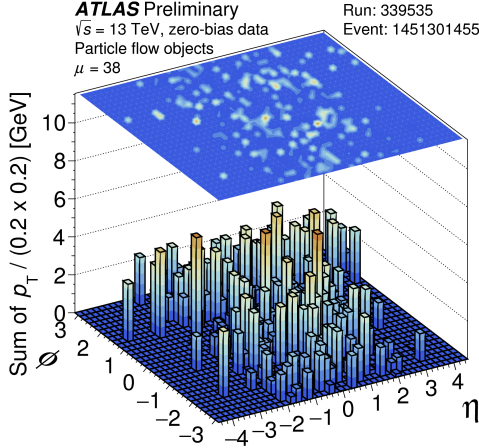


Figure 4.2: Sum of transverse momenta of neutral and charged particle flow objects in an area  $\Delta\eta \times \Delta\phi = 0.2 \times 0.2$  from a 2017 event with mean number of interactions per beam crossing  $\mu = 38$  [30]

Jet finding algorithms aim to approximate the hadron generators of calorimeter and track-based jets in the detector. They bridge the divide between observable jet objects and theoretical predictions in terms of QCD. There are several jet algorithms in use currently and key properties of all are collinear and infrared safety. This means that neither splitting a jet collinearly nor soft emissions should change jet structure. Without these qualities perturbation theory diverges at high orders. In addition modelling hadronization, the underlying event and pile-up is imprecise, so the ideal theory would be minimally sensitive to these effects. Anti- $k_t$  is the jet algorithm used by ATLAS and is infrared collinear-safe by construction and soft-resilient. Distance between pseudojets  $i$  and  $j$ ,  $d_{ij}$  and the distance between pseudojet  $i$  and the beam  $d_{iB}$  are defined. The algorithm loops through these distances beginning with the smallest distance. If  $d_{ij}$  is smallest, pseudojets  $i$  and  $j$  are combined, if

## CHAPTER 4. TRACKING AND ISOLATION IN ATLAS

$d_{iB}$  is smallest then  $i$  is a jet and removed from the list. This continues iteratively until all jets are defined. The distances are defined:

$$d_{ij} = \min(k_{ti}^{2p}, k_{tj}^{2p}) \frac{\Delta_{ij}^2}{R^2}, \quad (4.2)$$

$$d_{iB} = k_{ti}^{2p}$$

where  $\Delta_{ij}^2 = (y_i - y_j)^2 + (\phi_i - \phi_j)^2$  and  $k_{ti}$  is the transverse momentum of particle i.  $p$  is a new parameter which signifies the relative power of energy versus geometrical scales ( $\Delta_{ij}$ ). If  $p = 1$  the algorithm follows one known as  $k_t$ , if  $p = 0$  the algorithm is Cambridge/Aachen, and if  $p = -1$  the anti- $k_t$  algorithm results. One notable characteristic of this algorithm is its resilience to soft radiation while maintaining collinear safety, which is why it's the prevailing jet algorithm used on the ATLAS experiment [31].

Jet reconstruction and isolation doesn't end with particle flow and the anti- $k_t$  algorithm. Further corrections have to be applied to model data with Monte Carlo simulations. MC simulation are calibrated to better model pile-up and to improve jet angular resolution. Global sequential calibrations are calculated with MC using calorimeter, track, and muon chamber information to improve jet resolution. Following this, data is used to constrain uncertainties with through known dijet samples. These calibrations lead to final measurements of jet energy scale (JES) and jet energy resolution (JER) and provide reconstructed jet events in MC and data as well as a number recommended uncertainties for physics analyses to use. Figures 4.3 show jet energy scale and resolution as a function of  $p_T$  for PFlow jets modeling with the anti- $k_t$  algorithm after JES corrections are applied. Fully combined systematic uncertainties are also shown for each [32].

Jet reconstruction and calibration are crucial to this analysis and later chapters will detail how impactful jet energy scale and resolution uncertainties are to the overall precision of the

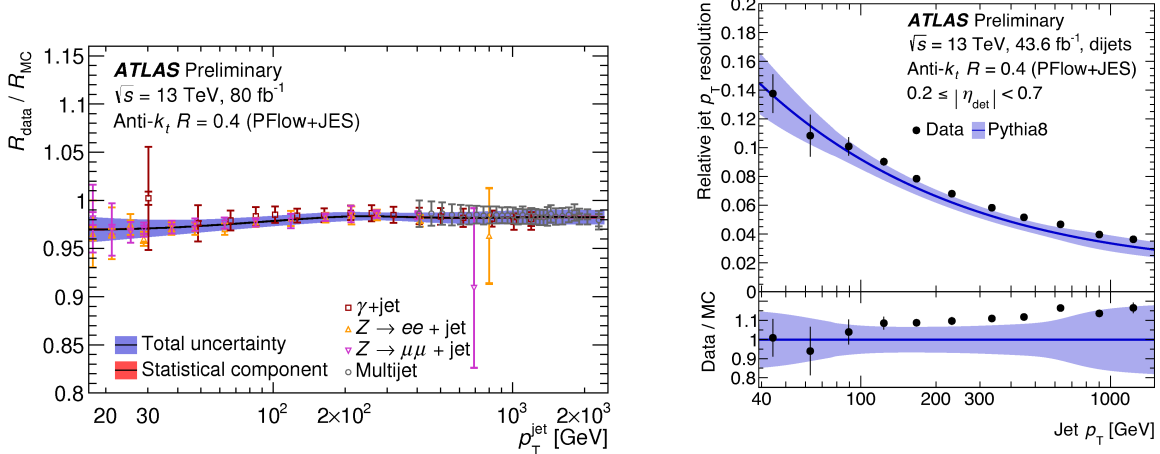


Figure 4.3: a.) data-to-simulation ratio for average jet  $p_T$  as a function of jet  $p_T$ . Three techniques shown as well as their their combination (black) and the combination total uncertainty. PFlow Anti- $k_t$  jets with  $R=0.4$  and JES correction. b.) relative jet energy resolution as a function of  $p_T$  for anti- $k_t$  PFlow jets with  $R = 0.4$  in 2017. JES calibrations applied and compared to MC with full systematic uncertainties [30].

$H \rightarrow WW$  cross-section measurement.

## 4.2 Missing transverse energy

Protons in collider experiments like ATLAS have momentum solely in the plane of the beam. Conservation of momentum implies that in the plane transverse to the beam ( $x - y$ ) the sum of momentum from all interaction by-products is zero. This is most often not the case and the non-zero transverse momentum from any interaction is termed  $E_T^{\text{miss}}$ . Missing transverse energy is a sign of final state neutrinos, which are massless and solely weakly interact so go undetected within ATLAS.  $E_T^{\text{miss}}$  could also point to new particles that cannot be directly detected like neutralinos or dark matter particles.  $E_T^{\text{miss}}$  could also signify interacting particles which evade detection in ATLAS due to detector acceptance or poor reconstruction [33].

## CHAPTER 4. TRACKING AND ISOLATION IN ATLAS

Missing transverse energy is determined using a combination of all reconstructed particles in an event. This is challenging because it involves all detector components and final particle types. The Jet/ $E_T^{miss}$  performance group delivers recommendations for multiple  $E_T^{miss}$  variables that we use in the  $H \rightarrow WW$ . This section will discuss  $E_T^{miss}$  reconstruction and performance followed by definitions of a few additional  $E_T^{miss}$  observables. Reconstructed  $E_T^{miss}$  calculations take into account both *hard* and *soft* event signals. Hard-events are composed of fully reconstructed and calibrated particles like electrons, muons, photons,  $\tau$ -leptons and jets. Hard events are reconstructed charged-particle tracks from the hard-scatter vertex, all objects except those considered *soft*. Reconstruction for all particle types happen independently which means that the same signal may be used to identify two distinct particles. This double-counting is taken into account in  $E_T^{miss}$  resolution. At its most basic,  $E_T^{miss}$  is defined:

$$E_{x(y)}^{miss} = - \sum_{i \in \text{hard objects}} p_{x(y),i} - \sum_{j \in \text{soft objects}} p_{x(y),j} \quad (4.3)$$

where overall  $E_T^{miss}$  is a vector composed of  $x, y$  components. In order to avoid double-counting the same detector signal in multiple particle reconstruction algorithms, hard objects are consider in order: electrons, photons, hadronically decaying  $\tau$ -leptons, and then jets. Muons have little overlap since they are reconstructed using MS and ID tracks (and muons alone leave tracks in the MS). As particles are reconstructed in this sequence, commonly used signals are rejected to avoid overlap. Another key variable is  $\sum E_T$  which is defined

$$\sum E_T = \sum_{\text{electrons}} p_T^e + \sum_{\text{photons}} p_T^\gamma + \sum_{\tau\text{-leptons}} p_T^\tau + \sum_{\text{muons}} p_T^\mu + \sum_{\text{jets}} p_T^{jet} - \sum_{\text{unused tracks}} p_T^{track} \quad (4.4)$$

The first five terms show the hard term while the last represents the soft-term. Selections are applied to reconstructed jets and particles to achieve optimal  $E_T^{miss}$  for a particular analysis [34]. In the context of  $H \rightarrow WW$  we use a “tight” configuration for  $E_T^{miss}$  classified by strict

## CHAPTER 4. TRACKING AND ISOLATION IN ATLAS

conditions on accepted jets. This working point has the greatest pile-up rejection which is integral to our analysis.

$E_T^{miss}$  reconstruction contains the complexity of each of its component parts and their  $p_T$  resolutions all affect total  $E_T^{miss}$  resolution. Pile-up and total event activity also play a large role in  $E_T^{miss}$  performance. Validations for  $E_T^{miss}$  are performed on a variety of observables and MC modelling is compared to reconstructed data. Systematic uncertainties are derived from comparing the reproducibility of these observables and their successful modelling of data. Resolution for reconstructed jets and leptons are also propagated to overall  $E_T^{miss}$  uncertainty.  $E_T^{miss}$  performance is evaluated using  $Z \rightarrow \mu\mu$  or  $Z \rightarrow e^-e^+$  and  $W \rightarrow e\nu$  events, the first with no genuine  $E_T^{miss}$  and the second with significant  $E_T^{miss}$  from neutrinos. After specific event selection and  $E_T^{miss}$  reconstruction, each of these samples  $E_T^{miss}$  distributions is studied and data and MC demonstrated to match within uncertainties. Selected performance observables are shown for the full Run-2 sample set in 4.4. Here  $Z \rightarrow e^+e^-$  events are selected and reconstructed track-based soft term  $E_T^{miss}$  and  $E_T^{miss}$  significance distributions are shown. Data and MC show good agreement.

In this analysis, a number of important  $E_T^{miss}$  variables are used. This selection will be further explained in later chapters, but these variables are used to cut on background (particularly from  $Z \rightarrow \tau\tau$  events and to select for the signal  $H \rightarrow WW \rightarrow \ell\nu\ell\nu$  channel where its two neutrinos require significant  $E_T^{miss}$ ). Some of the variables used for these selections include track-based  $E_T^{miss}$ , track-based soft term  $E_T^{miss}$ ,  $E_T^{miss}$  significance,  $m_{\tau\tau}$ , and  $p_T^{tot}$ . The  $E_T^{miss}$  soft term is composed of a track-based and calo-based component. The calorimeter-based component is highly dependent on pile-up and so using a track-based soft term reduces overall pile-up dependence. Track-based  $E_T^{miss}$  uses only reconstructed ID tracks from the primary vertex and in our analysis this has been just as powerful discriminant for isolating  $Z \rightarrow \tau\tau$  background events from VBF signal as overall  $E_T^{miss}$  without the same

## CHAPTER 4. TRACKING AND ISOLATION IN ATLAS

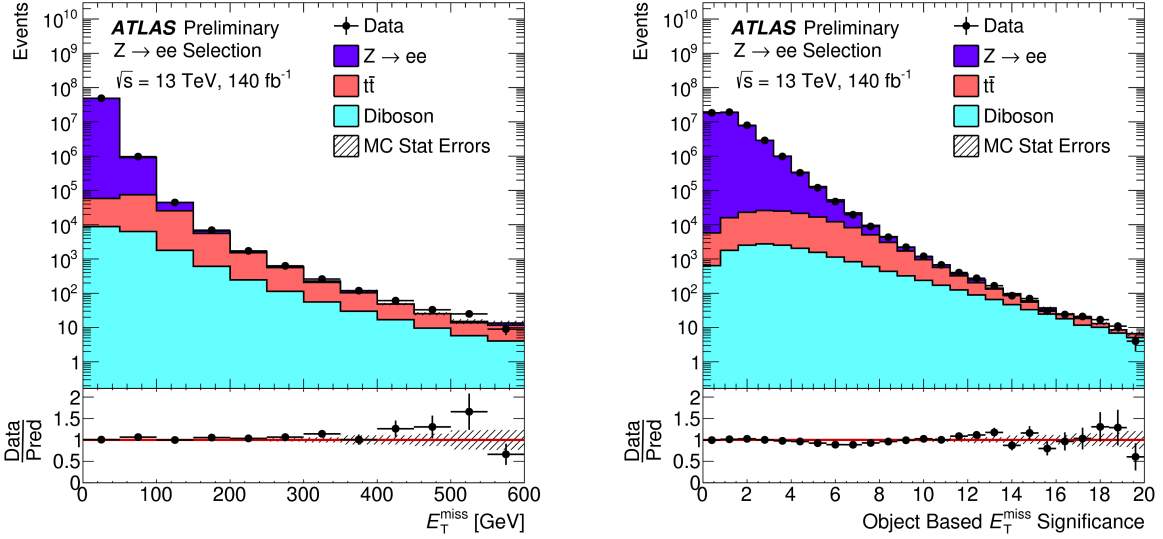


Figure 4.4: a.) Track-based Soft Term  $E_T^{miss}$  shown for the complete Run-2 dataset with an integrated luminosity of  $140 \text{ fb}^{-1}$ . Monte Carlo simulations are compared to data for the tight  $E_T^{miss}$  working point. b.) Track-based Soft Term  $E_T^{miss}$  significance modelling shown in the tight  $E_T^{miss}$  working point [30]

pile-up dependence and correlation with other kinematic variables.  $E_T^{miss}$  significance is newly defined and recommended variable from the Jet/ $E_T^{miss}$  group. Described further in [33], this discriminates real missing energy from momentum resolution effects using a calculated likelihood. Shown in 4.4,  $E_T^{miss}$  significance peaks at low values if  $E_T^{miss}$  likely comes from resolution effects and not from a real invisible particle in the event. Our analysis also defines two variables based on  $E_T^{miss}:p_T^{tot}$  describes the total transverse momentum from all hard objects in the event and  $m_{\tau\tau}$  is defined

$$m_{\tau\tau} = \frac{m_{\ell\ell}}{\sqrt{x_1 * x_2}} \quad (4.5)$$

where

$$\begin{aligned} x_1 &= \frac{p_x^{\ell 0} * p_y^{\ell 1} - p_y^{\ell 0} * p_x^{\ell 1}}{p_y^{\ell 1} * E_{Tx}^{miss} - p_x^{\ell 1} * E_{Ty}^{miss} + p_x^{\ell 0} * p_y^{\ell 1} - p_y^{\ell 0} * p_x^{\ell 1}}, \\ x_2 &= \frac{p_x^{\ell 0} * p_y^{\ell 1} - p_y^{\ell 0} * p_x^{\ell 1}}{p_x^{\ell 1} * E_{Ty}^{miss} - p_y^{\ell 0} * E_{Tx}^{miss} + p_x^{\ell 0} * p_y^{\ell 1} - p_y^{\ell 0} * p_x^{\ell 1}} \end{aligned} \quad (4.6)$$

Each of these variables contributes to our signal region selection and elimination of background. A number of systematic uncertainties from reconstructed  $E_T^{miss}$  are defined and used in our analysis, though these are small compared to the uncertainties from jets and other final state particles.

### 4.3 Electrons

Accurate reconstruction and calibration of electrons within the ATLAS detector is integral to precision measurements, including the  $H \rightarrow WW$  measurement in which an electron is required in the signal’s final state. Reconstruction, identification, and energy measurements of electrons and photons are the goals of the Electron and Photon Performance group. This section will summarize each of these calibration processes and their performances with a focus on electrons as they are particularly important in reconstructing final state particles for  $H \rightarrow WW$ .

Electrons are defined through energy deposits in the calorimeter, called superclusters, each with a matching track from the Inner Detector. Photons are defined strictly through a calorimeter cluster though “converted” photons can be matched to conversion vertexes in the tracker if they are matched to a leptonic initial state. Converted photons constitute a large fraction of reconstructed photons. Figure 4.6 shows the procedure for electron and photon reconstruction. First, topo-clusters in the EM calorimeter and tracks in the ID are

## CHAPTER 4. TRACKING AND ISOLATION IN ATLAS

selected and matched together. Topo-clusters are defined based on signal to noise significance in calorimeter cells and calorimeter cell proximity. Standard reconstruction takes place in the inner detector and potential tracks are assigned to topo-clusters if their positions are within a region-of-interest compatible with that topo-clusters EM shower. Next, super-clusters are built from track-matched topo-clusters. Topo-clusters are tested for use as seed cluster candidates which begin super-clusters. Remaining topo-clusters are tested for compatibility as satellite clusters to each seed candidate. The resultant combination of seed and satellite clusters form super-clusters which are defined independently for photons and electrons. Finally, tracks are added to super-clusters, energy calibration and position corrections are applied, and analysis-level electrons and photons are created. Reconstruction efficiency for electrons is quite high, particularly at high  $p_T$ . Photon reconstruction efficiency is significantly lower due to their dependence solely on calorimeter clusters [35].

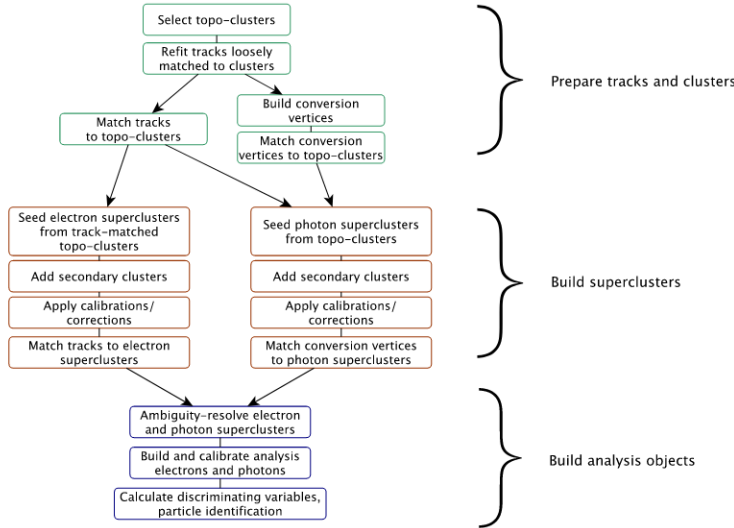


Figure 4.5: Electron and photon reconstruction algorithm [35]

Electron and photon energy resolution is determined from EM calorimeter showers and this is optimized with multivariate regression algorithms. Energy scale is also corrected using

## CHAPTER 4. TRACKING AND ISOLATION IN ATLAS

calibration from well-known  $Z \rightarrow ee$  decays and verified with other  $Z$ -boson decays. Similarly, these calibrations are calculated for photons using  $Z \rightarrow \ell\ell\gamma$ . Systematic uncertainties that effect these calibrations include passive material between the interaction point and the EM calorimeter and pile-up [35].

While electron and photon objects are already identified and reconstructed further ‘identification’ selections are used to improve electron and photon purity. Prompt electrons are identified with a likelihood discriminant which takes into account track parameters and electromagnetic shower properties. The primary electron track must stretch into the two inner tracking layers closest to the beam line and hit multiple points in the silicon-strip detector. The likelihood discriminant is calculated from probability density functions formed by smoothing histograms of 13 discriminating variables with an adaptive kernel density estimator. These are calculated separately for both the likelihood that an event reconstructs a prompt electron (signal) or that it does not (background). These likelihoods are derived from well-known  $Z \rightarrow ee$  and  $J/\Psi \rightarrow ee$  events recorded in Run-2. A tag-and-probe method was used to evaluate this likelihood- one electron in each decay must satisfy strict Run-1 likelihood discriminant requirements while the other serves as a probe of the new likelihood dscriiminator. Three electron working points are derived- Loose, Medium, and Tight, each with respectively lower efficiencies and higher purity. Physics analyses use the working points optimized for their analysis. For the  $H \rightarrow WW$  measurement we use ‘Medium’ reconstructed electrons which have a lower efficiency than the loose condition but a factor  $2\times$  greater rejection of background in electron identification. Figure ?? shows electron identification efficiency for each of the working points in a sample of  $Z \rightarrow ee$  events where efficiency is calculated through comparisons to MC simulated  $Z \rightarrow ee$  and  $J/\Psi \rightarrow ee$  events. The average efficiencies for electroweak processes are 93%, 88% and 80% respectively for Loose, Medium, and Tight operating points and gradually increase at high  $E_T$  [35].

## CHAPTER 4. TRACKING AND ISOLATION IN ATLAS

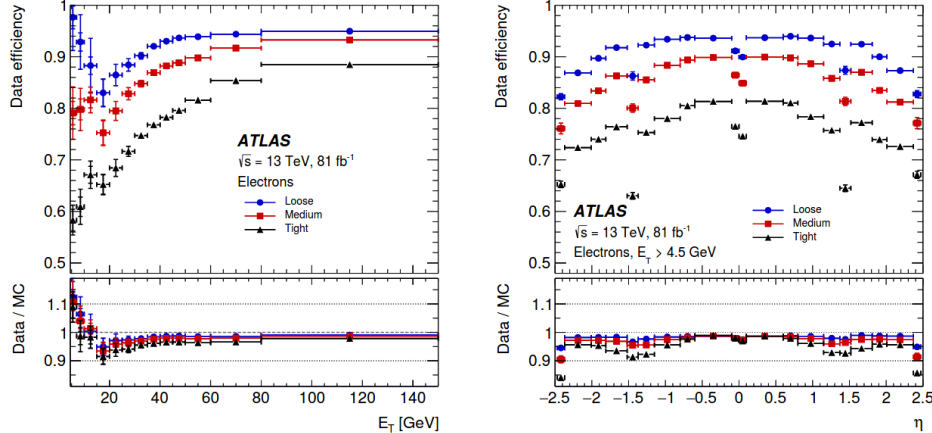


Figure 4.6: Electron reconstruction efficiency as a function of  $E_T$  and  $\eta$  in  $Z \rightarrow ee$  events for Losse, Medium, and Tight electrons [35]

Track hits and calorimeter deposits near reconstructed electrons and muons can bias energy, momentum, and position measurements. Isolation performance are defined for calorimeter clusters by  $E_T^{cone}$ , the sum of transverse energy within a cone  $\Delta R$  near a photon or electron cluster after correcting for leakage and pile-up effects. Track isolation  $p_T^{cone}$  is defined as a sum of the transverse momentum of tracks within a cone about the electron track or interpolated photon track. For electrons the distance between nearby decay products is directly related to electron  $p_T$  so a variable cone size can used such that

$$\Delta R = \min\left(\frac{10}{p_T}, \Delta R_{max}\right) \quad (4.7)$$

where  $\Delta R_{max}$  is typically 0.2. Isolation working points strike a balance between efficiency and rejection of misidentified prompt electrons. The gradient working point is used by the  $H \rightarrow WW$  analysis and gives an efficiency of 90% at  $p_T = 25 \text{ GeV}$  and 99% at  $p_T = 60 \text{ GeV}$ . These values are reached through cuts on  $E_T^{cone20}$  and  $p_T^{varcone20}$  derived from  $J\Psi \rightarrow ee$  and  $Z \rightarrow ee$  MC simulations. Efficiency of different isolation working points for electrons are shown in Figure 4.7. These are shown in Medium identified electrons for  $Z \rightarrow ee$  events and

## CHAPTER 4. TRACKING AND ISOLATION IN ATLAS

demonstrate the efficiencies possible with different cuts on the calorimeter and track-based isolation variables. The Gradient working point delivers reasonably high efficiency that is stable across  $\eta$  and is coupled with high background rejection of misidentified electrons [35].

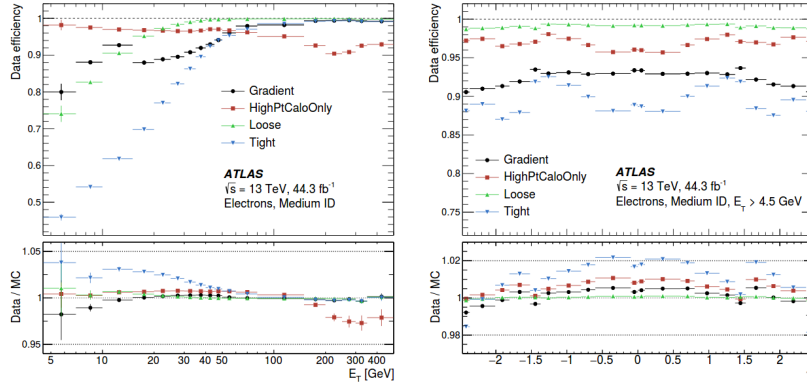


Figure 4.7: Electron isolation efficiency shown for four working points in  $Z \rightarrow ee$  events as a function of  $E_T$  and  $\eta$  [35]

Photon isolation is solely calorimeter-based.  $Z \rightarrow \ell\ell\gamma$  events are used for photon isolation efficiency measurements and three working points are available which balance efficiency and background rejection just as in the electron case.

Electron reconstruction, calibration, identification, and isolation are all integral for the  $H \rightarrow WW$  analysis in order to accurately identify electrons in the final state of candidate Higgs events. Systematic uncertainties from electron identification and isolation efficiency will be discussed further in later chapters and play a significant role in  $H \rightarrow WW$  cross-section measurements.

## 4.4 Muons

Muons are abundant in the ATLAS detector and help lead to some of the most interesting physics results and analyses produced by the ATLAS experiment including  $H \rightarrow WW \rightarrow$

## CHAPTER 4. TRACKING AND ISOLATION IN ATLAS

$\ell\nu\ell\nu$  measurements which require a muon in the final state. The Muon Combined Performance group is tasked with producing the most accurate muon data for physics analyses. This includes muon reconstruction, identification, isolation, and analysis of efficiency, as well as muon momentum scale and resolution. The group’s goal is to create a number of “working points” tailored to different types of physics analyses that will isolate, identify, and reconstruct muons in the region of interest to the analyses. The working points are continuously updated and improved before being tested and implemented on different analyses. My work with the MCP group has focused on applying corrections necessary for muon momentum scale at the per mille level and resolution at the percent level in simulation/data. These are derived by a template fit of simulations smeared and corrected by variables in data. These corrections are validated by comparisons to simulations over a variety of variables.

Muon reconstruction is performed independently in the ID and MS and the information from these separate sub-detectors is combined to form full tracks. This section will focus on: 1) reconstruction in the ID, which is the same for any charged particle; 2) reconstruction in the MS, which is particular to muons; and 3) the combined reconstruction, which uses information from both the ID and MS.

In the ID, a pattern recognition algorithm reconstructs particle tracks with an inside-out sequence [36]. A track from a particle traversing the barrel typically has 3 pixel clusters, 8 SCT clusters and more than 30 TRT straw hits. The sequence begins by finding three-dimensional space points from the silicon hits. Each set of three space points which originate in the interaction point are used to trace hits up to the outer edge of the silicon detector. The final track parameters are fit through a collection of hits that extend to the TRT [37].

Muon reconstruction in the MS is not an inside-out procedure like that in the ID. Reconstruction begins with a search for hit patterns in each MS subdetector, which are called segments. The middle of the MS typically exhibits the largest number of trigger hits, there-

## CHAPTER 4. TRACKING AND ISOLATION IN ATLAS

fore tracks are built by working out from the center of the MS and connecting segments layer-by-layer. Criteria such as hit multiplicity and fit quality determine track acceptance. At least two segments are needed to build a track. Hits associated with each track candidate are fitted using a global  $\chi^2$  fit. A track candidate is accepted if it passes the selection criteria [? ].

The combined ID-MS reconstruction uses different algorithms to find different *muon types*. There are four main types outlined below, but preference-in terms of overlap between types-is given to Combined (CB), then Segment-tagged (ST), and finally Calorimeter Tagged (CT) muons. These algorithms have been continuously been improved to yield better precision, speed, and robustness against misidentification [38].

- **Combined muon (CB):** This type combines tracks from the ID and MS detectors using a global refit on all hits (some may be removed or added to improve quality). Most muons are reconstructed using an outside-in method.
- **Segment-tagged muon (ST):** ST muons are assigned an ID track that is associated with at least one local MDT or CSC track after extrapolation. These are used when muons cross only one layer of the MS because of low  $p_T$  or regions out of most MS layer boundaries.
- **Calorimeter-tagged muon (CT):** These muons are identified by an ID track that can be matched to a minimum ionizing particle energy deposit in the calorimeter. These muons have the lowest purity but are optimized for  $|\eta| < 0.1$  and  $1.5 < p_T < 100$  GeV where the MS is only partially instrumented.
- **Extrapolated muon (ME):** These muons are reconstructed in the MS with the addition of silicon points and with a loose requirement that the muon track originated

## CHAPTER 4. TRACKING AND ISOLATION IN ATLAS

at the IP. In general, this muon is required to traverse  $2 - 3$  layers of MS chambers. These are mainly used to extend acceptance for  $2.5 < |\eta| < 2.7$ , which is not covered in the ID.

In order to identify muons from other particles (like backgrounds from pion and kaon decays) strict quality requirements must be set to select prompt muons with high efficiency. Ideal signal muons are those that come from  $W$  decays (as opposed to light-hadron decays) and originate from the interaction point. We use a few variables to identify muons:

- $q/p$  significance: The absolute value of the difference between the ratio of the charge and momentum of muons in the ID and MS divided by the sum in quadrature of their corresponding uncertainties.
- $\rho'$ : The absolute value of the difference between the  $p_T$  measurements in the ID and MS divided by the  $p_T$  of the combined track.
- $\chi^2$ : The normalized fit parameter of the combined track.

Specific requirements on the number of hits in the ID and MS assure that inefficiencies are expected and momentum measurements are robust. There are four muon identification selections that each addresses specific needs of physics analyses [38].

- **Loose Muons**: The *Loose* criteria maximizes the reconstruction efficiency, losing very few potential muons, while providing satisfactory tracks. All muon types are used in this criteria.
- **Medium Muons**: *Medium* is the default selection for muons in ATLAS because it minimizes systematic uncertainties associated with reconstruction and calibration. Only CB and ME tracks are used with requirements for over 3 hits in at least two MDT layers in most regions. All *Medium* muons are included in the *Loose* criteria.

## CHAPTER 4. TRACKING AND ISOLATION IN ATLAS

- **Tight Muons:** *Tight* selects muons with the highest purity, but sacrifices efficiency. All *Tight* muons are included in the *Medium* selection, but only CB muons with at least two hits in the MS are considered, and the  $\chi^2$  value must be less than 8.
- **High- $p_T$  Muons:** *High- $p_T$*  muons have good momentum resolution for tracks with  $p_T > 100$  GeV. This is beneficial to searches for high-mass  $Z'$  and  $W'$  resonances. CB muons in the *Medium* selection with at least 3 hits in 3 MS stations are included.

The  $H \rightarrow WW$  analysis uses Tight muons with the added condition that  $p_T > 15$  GeV and  $\eta < 2.5$  to gain the highest purity possible and eliminate background from misidentified leptons, which constitute a significant background even with this selection.

We measure the muon reconstruction efficiency in two different ways in the regions  $|\eta| < 2.5$  and  $2.5 < |\eta| < 2.7$ . First, in the barrel region, we use the **Tag-and-Probe** method. In this method we select an almost-pure sample of  $J/\psi$  and  $Z$  decays and require the leading muon to be a *Medium* muon labeled the **tag**. This muon fires the trigger. The subleading muon, the **probe**, must be reconstructed independently. There are three types of probes:

- **ID track:** Allows measurement of MS efficiency and of tracks not accessible to CT muons.
- **CT tracks:** Allows measurement of MS efficiency and has powerful rejection of background (especially at low  $p_T$ ). This is the most commonly used probe.
- **MS tracks:** Allows measurement of ID and CT efficiency.

To find the overall efficiency of *Medium*, *Tight*, or *High- $p_T$*  muons, we multiply the efficiencies associated with each type of probe. The efficiency  $\epsilon(X|CT)$  ( $X = Medium / Tight / High- $p_T$ ) of reconstructing these muons assuming a reconstructed ID track is measured$

## CHAPTER 4. TRACKING AND ISOLATION IN ATLAS

using a CT muon as probe. This result is corrected by the efficiency  $\epsilon(\text{ID}|\text{MS})$  of the ID track reconstruction measured using MS probes.

$$\epsilon(\text{X}|\text{ID}) \cdot \epsilon(\text{ID}) = \epsilon(\text{X}|\text{CT}) \cdot \epsilon(\text{ID}|\text{MS}) \quad (\text{X} = \text{Medium}/\text{Tight}/\text{High-}p_T) \quad (4.8)$$

The ID track reconstruction efficiency must be independent from the muon spectrometer track reconstruction ( $\epsilon(\text{ID}) = \epsilon(\text{ID}|\text{MS})$ ). In addition, the use of a CT muon as a probe instead of an ID track must not affect the probability for *Medium*, *Tight*, or *High- $p_T$*  reconstruction ( $\epsilon(\text{X}|\text{ID}) = \epsilon(\text{X}|\text{CT})$ ). These assumptions are largely true with simulations showing some small deviations. These deviations are taken into account when calculating systematic errors.

The reconstruction efficiency of *Loose* muons is measured separately for CT muons within  $|\eta| < 0.1$  and all other *Loose* types. The CT muon efficiency is measured using MS probe tracks, and the efficiency of other muons is evaluated similarly to the *Medium*, *Tight*, and *High- $p_T$*  muons using CT probe muons [38]. For  $|\eta| > 2.5$ , the efficiency is calculated using the ME muons in the **Loose** and **Medium** selections. The number of muons observed in this region is normalized to the number of muons observed in the region  $2.2 < |\eta| < 2.5$ . A more detailed discussion of the efficiency measurement in this region can be found in Ref [39].

**Scale factors** are defined as the ratios between the efficiency of data and the efficiency of Monte Carlo simulations. They are used to describe the deviation between simulated and real detector behavior and are used in physics analyses to correct simulations.

Figure 4.8 displays reconstruction efficiency for *Medium* muons over a range of  $p_T$  and all other working plotted over  $\eta$ . While *Medium* muons have a higher efficiency than the *Tight* selection used in this analysis, both have an efficiency above 95% for a large range

## CHAPTER 4. TRACKING AND ISOLATION IN ATLAS

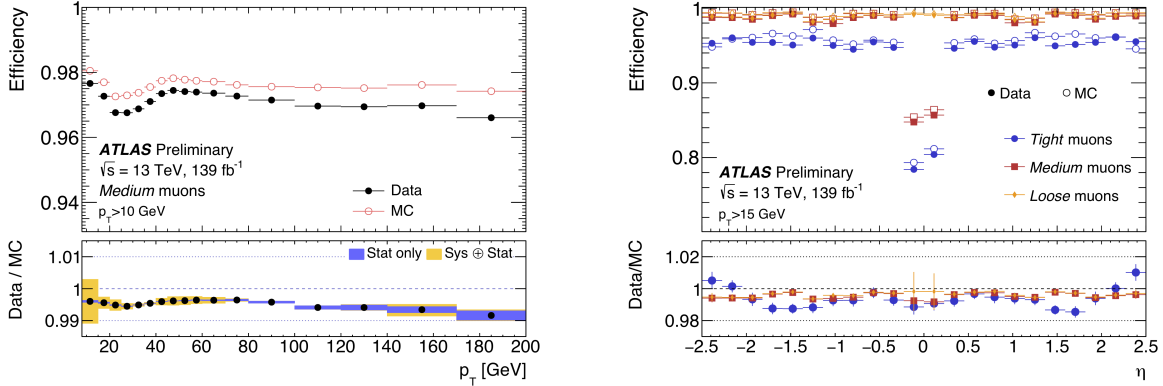


Figure 4.8: On the left, reconstruction efficiency for *Medium* muons from  $Z \rightarrow \mu\mu$  events is displayed as a function of the  $p_T$  of the muon in the region  $0.1 < |\eta| < 2.5$  with systematic and statistical uncertainties. On the right, muon reconstruction efficiency is shown as a function of  $\eta$  in  $Z \rightarrow \mu\mu$  events for muons with  $pT > 15$  GeV for *Medium*, *Loose* and *Tight* muons. In both plots the full  $139\text{fb}^{-1}$  Run-2 dataset is used[40].

of  $\eta$  and  $p_T$ .  $J/\psi$  decays probe low  $p_T$  muons while  $Z$  decays probe muons of a higher  $p_T$  allowing a large range to be defined. In addition, MC simulations match data quite well - within 1 – 2%. The only significant loss of efficiency is seen at extremely low  $\eta$  due to criteria excluding ID muons. Overall, the default *Tight* muon selection demonstrates a high reconstruction efficiency.

Isolating muons from heavy particles is one of the keys to understanding the background in many physics analyses. When heavy particles like  $W$ ,  $Z$ , and Higgs bosons decay they often produce muons in isolation. Semileptonic decays, on the other hand, typically produce muons embedded in jets.

The MCP group uses two muon isolation variables: a track-based variable ( $p_T^{varcone30}$ ) and a calorimeter-based variable ( $E_T^{topocone20}$ ).  $p_T^{varcone30}$  is defined as the scalar sum of the transverse momenta of tracks with  $p_T > 1$  GeV in a cone around the muon of transverse momentum  $p_T$  excluding the muon track itself. The cone size is  $p_T$ -dependent to improve the performance for muons produced in decays with a large transverse momentum.  $E_T^{topocone20}$  is

## CHAPTER 4. TRACKING AND ISOLATION IN ATLAS

defined as the sum of the transverse energy of topological clusters in a cone around the muon after subtracting the contribution from the energy deposit of the muon itself and correcting for pile-up effects [41].

Table ?? defines seven isolation selection criteria - called “isolation working points” - that optimize different physics analyses. The *LooseTrackOnly* and *FixedCutTightTrackOnly* working points are defined by cuts on the relative track-based isolation variable. All other working points are defined by cuts applied separately on both relative isolation variables. All cuts are tuned as a function of the  $\eta$  and  $p_T$  of the muon to obtain a uniform performance. The target efficiencies of the different working points are described in Table 4.1. The efficiencies for the seven isolation working points are measured in data and simulation using the **Tag-and-Probe** method described previously on  $Z \rightarrow \mu\mu$  decays. Figure 4.9 shows the isolation efficiency measured for *Medium* muons in data and simulation as a function of the muon  $p_T$  for two different working points. In both the *GradientLoose* and *FixedCutTightTrackOnly* working points, efficiency is above 90% and matches simulation well within errors for muons for higher  $p_T$  muons. In the *HWW* analysis, a fixed isolation cuts are optimized independent of Muon Performance working points. Only muons with  $p_T > 15$  GeV are considered so the efficiency is optimized for muons which pass this and the *Tight* selection cuts.

The  $H \rightarrow WW$  analysis uses muon isolation cuts  $p_T^{varcone30}/p_T < 0.06\zeta$  and  $p_T^{topocone20}/p_T < 0.09$  which are relatively tight selections and are selected to reduce misidentified lepton backgrounds.

The muon momentum scale and resolution are studied using  $Z$  and  $J/\psi$  decays. In order to obtain agreement between simulation and data in muon momentum scale to the per mille level and in resolution to the percent level, we need to apply a set of corrections to the simulated muon momentum. After applying the corrections we validate them by comparing

## CHAPTER 4. TRACKING AND ISOLATION IN ATLAS

Isolation WP	Discriminating variable(s)	Definition
<i>LooseTrackOnly</i>	$p_T^{\text{varcone}30} / p_T^\mu$	99% efficiency constant in $\eta$ and $p_T$
<i>Loose</i>	$p_T^{\text{varcone}30} / p_T^\mu, E_T^{\text{topocone}20} / p_T^\mu$	99% efficiency constant in $\eta$ and $p_T$
<i>Tight</i>	$p_T^{\text{varcone}30} / p_T^\mu, E_T^{\text{topocone}20} / p_T^\mu$	96% efficiency constant in $\eta$ and $p_T$
<i>Gradient</i>	$p_T^{\text{varcone}30} / p_T^\mu, E_T^{\text{topocone}20} / p_T^\mu$	$\geq 90(99)\%$ efficiency at 25 (60) GeV
<i>GradientLoose</i>	$p_T^{\text{varcone}30} / p_T^\mu, E_T^{\text{topocone}20} / p_T^\mu$	$\geq 95(99)\%$ efficiency at 25 (60) GeV
<i>FixedCutTightTrackOnly</i>	$p_T^{\text{varcone}30} / p_T^\mu$	$p_T^{\text{varcone}30} / p_T^\mu < 0.06$
<i>FixedCutLoose</i>	$p_T^{\text{varcone}30} / p_T^\mu, E_T^{\text{topocone}20} / p_T^\mu$	$p_T^{\text{varcone}30} / p_T^\mu < 0.15, E_T^{\text{topocone}20} / p_T^\mu < 0.30$

Table 4.1: The seven isolation working points are described by their discriminating variables and defining criteria [38].

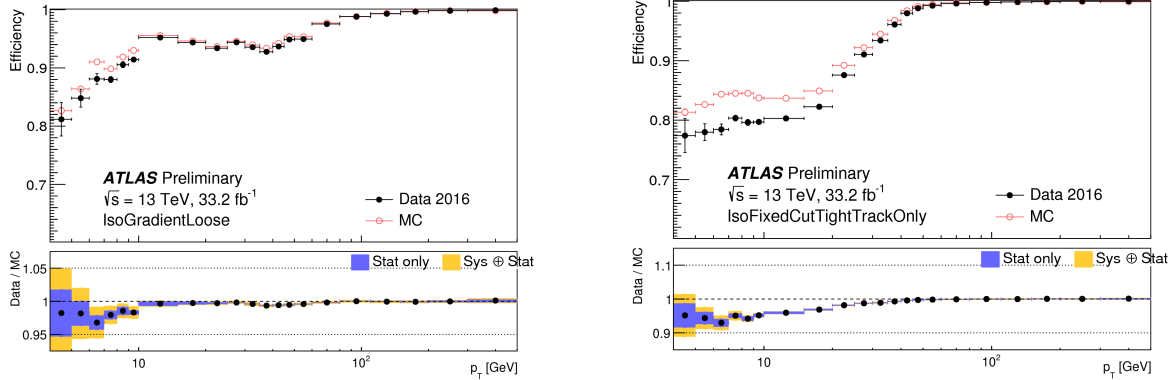


Figure 4.9: Isolation efficiency for the GradientLoose (left) and FixedCutTrackOnly (right) muon isolation working points. The efficiency is displayed as a function of  $p_T$  in  $Z \rightarrow \mu\mu$  events. The black markers show efficiency measured in data samples while the red show MC simulations. The bottom panel shows the ratio of the efficiency between the two as well as both statistical and systematic uncertainties [42].

the muon momentum scale and resolution between simulation and data over  $\eta$ ,  $\phi$ , and  $p_T$ .

We extract the calibration parameters with the transverse momentum of the ID and MS components of a CB track. The corrected transverse momentum is described by the following equation:

## CHAPTER 4. TRACKING AND ISOLATION IN ATLAS

$$p_T^{\text{Cor,Det}} = \frac{p_T^{\text{MC,Det}} + \sum_{n=0}^1 s_n^{\text{Det}}(\eta, \phi)(p_T^{\text{MC,Det}})^n}{1 + \sum_{m=0}^2 \Delta r_m^{\text{Det}}(\eta, \phi)(p_T^{\text{MC,Det}})^{m-1} g_m}. \quad (4.9)$$

Here the  $g_m$  terms are normally distributed random variables with zero mean and unit width. The  $\Delta r$  and  $s$  terms describe momentum resolution smearing and scale corrections applied in specific detector regions, respectively. Both the ID and MS are divided into 18 pseudorapidity regions and the MS is divided into two  $\phi$  bins separating the large and small sectors. Each of these bins leverages different alignment techniques and has different material distributions.

There are two  $s$  terms that represent different types of corrections.  $s_1$  corrects for inaccuracy in the description of the magnetic field integral and the detector in the direction perpendicular to the magnetic field.  $s_0$  corrects for the inaccuracy in the simulation of energy loss in the calorimeter and other materials. Since this loss is negligible in the ID, it is only nonzero in the MS [38].

The denominator introduces momentum smearing which broadens the  $p_T$  resolution in simulation. The parametrization of the smearing is defined:

$$\frac{\sigma(p_T)}{p_T} = r_0/p_T \oplus r_1 \oplus r_2 \cdot p_T. \quad (4.10)$$

In this equation  $r_0$  is related to the fluctuations in energy loss in the traversed material,  $r_1$  accounts for multiple scattering, local magnetic field inhomogeneities, and local radial displacements of hits, and  $r_2$  describes intrinsic resolution effects caused by the spatial resolution of the hit measurements and by residual misalignment of the MS [38]. Correction parameters are extracted from data using a binned maximum-likelihood fit with templates derived from simulation which compares the invariant mass distributions for  $J/\psi$  and  $Z$  decay candidates in data and simulation. The muons are carefully selected to be compati-

## CHAPTER 4. TRACKING AND ISOLATION IN ATLAS

ble with tracks that start at the interaction point and penetrate both the ID and the MS. Muons are also selected to pass specific momentum and isolation criteria. The dimuon mass distribution of these tracks in data is fitted using a Crystal Ball function convoluted with an exponential background distribution in the ID and MS fits. The background model and its normalization are then used in the template fit. The fits are performed in  $\eta - \phi$  regions of fit (ROFs) which compromise regions with uniform features in the ID and MS [38].

From these fits, we can find the smearing terms across all  $\eta$  regions. Once the corrections are applied we can validate that the agreement between data and MC is excellent. This is shown in Figure 4.10.  $r_0$  is set to zero across all  $\eta$  regions since energy loss is negligible in the ID.  $r_1$  and  $r_2$  increase as  $\eta$  increases since spatial resolution decreases and inhomogeneities increase as we move from the barrel to end-cap regions of both the ID and MS. Muon momentum corrections are continuously studied during ATLAS runs to validate muon calibration performance and account for discrepancies.

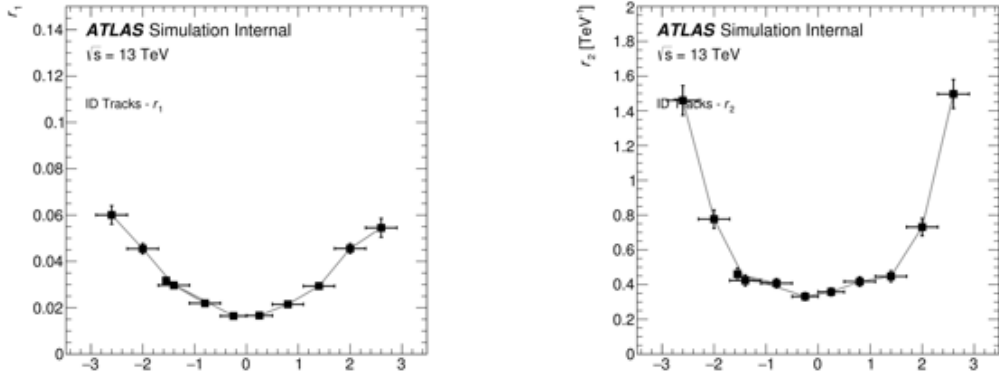


Figure 4.10: The  $r$ -values from each of 10 fits of resolution to  $p_T$  for ID muon simulations are shown. Each value corresponds to a particular ROF or  $\eta$  region. These plots show  $r_1$  (left) and  $r_2$  (right) as functions of leading muon  $\eta$ .

In this chapter, I have outlined the procedures for building all the component physics objects we use in the  $H \rightarrow WW$  analysis. The successful reconstruction, calibration, and

## *CHAPTER 4. TRACKING AND ISOLATION IN ATLAS*

isolation of jets, missing transverse energy, electrons, and muons is integral to the measurement of VBF Higgs bosons, as they decay to a final state with each of these components. As discussed, the measurement of physics objects includes their systematic and statistical uncertainties all of which are taken into account in our final measurement. The next chapters will use these physics objects and their kinematic variables to understand our background and signal events.

# **Chapter 5**

## **Event Selection**

**5.1 Data and Monte Carlo samples**

**5.2 Object definitions**

**5.3 Event selection**

# Chapter 6

## Backgrounds and Systematics

### 6.1 Backgrounds

While the VBF  $H \rightarrow WW \rightarrow \ell\nu\ell\nu$  channel gives a fairly clear signal with  $E_T^{\text{miss}}$ , two leptons, and 2 jets, there are substantial backgrounds with similar final states. These include Drell-Yan processes (in which a  $Z$  boson is formed from quark anti-quark annihilation of the two colliding protons), top quark final states (predominantly  $t\bar{t}$ ) and diboson events (led by SM  $WW$  events), Higgs decays from the ggF production mode and finally background from mis-identified leptons, called fakes. In this section I will detail each background and describe our methods for estimating their role in our overall results. I will also demonstrate the purity and modelling of these backgrounds in their control regions. I made key contributions in this analysis in optimizing and testing control region definitions and their effects on our overall results.

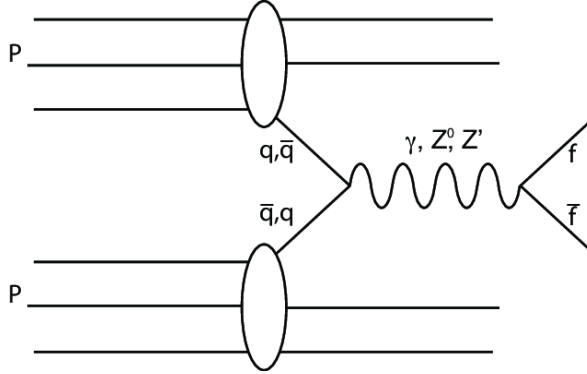


Figure 6.1: Feynman diagram for Drell-Yan process in which two quarks produce a photon or  $Z$ -boson that then decays leptonically.

### 6.1.1 Drell-Yan background ( $Z \rightarrow \tau\tau$ )

The Drell-Yan background, alternatively called  $Z \rightarrow \tau\tau$  or  $Z+\text{jets}$  is produced in the initial collision when two quarks produce a  $Z$  boson which then decays to two leptons (in the largest background,  $\tau$  leptons which then decay to electron/muons and neutrinos). Thus there are two jets and two leptons in its final state as well as missing energy from neutrinos, all of which are indicative of signal VBF Higgs events as well. A typical Drell-Yan feynman diagram is shown in Figure 6.1. The Drell-Yan background can be discriminated from our signal as well as the other backgrounds in two main ways- first in terms of the mass of the overall event aligning with the mass of the  $Z$  boson. To select for Drell-Yan events we can select those which  $m_{\tau\tau}$  is near the  $Z$  mass peak.  $m_{\tau\tau}$  is defined in the previous section and cutting on this in a 25 GeV window about the  $Z$ -mass peak drastically improves our  $Z+\text{jets}$  purity from only 19% of total events to  $\approx 52\%$ . The second main discriminant our analysis utilizes to isolate  $Z+\text{jet}$  events is a BDT trained to discriminate  $Z+\text{jets}$  and VBF signal events.

The  $Z+\text{jets}$  background has a very different  $E_T^{\text{miss}}$  signature than VBF as this sample does not contain the level expected from VBF Higgs events. Thus a BDT trained to discriminate

## CHAPTER 6. BACKGROUNDS AND SYSTEMATICS

between VBF signal events and the  $Z + \text{jets}$  background uses a range of  $E_{\text{T}}^{\text{miss}}$  variables and cutting on this trained discriminant rather directly on  $E_{\text{T}}^{\text{miss}}$  provides an enhanced purity. The training and results from the BDT are described in the next subsection. Note that the following results from substantial optimization on training inputs and techniques where the final BDT has high discrimination, no under or overtraining, and utilizes variables which are well-modelled and not highly correlated to one another.

### $Z \rightarrow \tau\tau$ BDT

A decision tree is a collection of cuts designed to classify events as signal-like or background-like. A given signal event is correctly identified if it is placed in a signal-dominated leaf and vice-versa for background events. After the initial tree is built another tree is grown to better separate the signal and background events misidentified by the first tree. This proceeds iteratively until there is a collection of a specified number of trees, in a process known as boosting. A weighted average is taken from all these trees to form a BDT output discriminant with values ranging from -1 to 1.

The BDT is trained using  $e\mu + \mu e$  events after the VBF selection and the signal regions cuts including that on  $n_{\text{jets}}$ ,  $b$ -veto, OLV, CJV,  $M_{jj}$  and  $DY_{jj}$ . In this way, the phase space in which we train the BDT is exactly the same as the one where we apply it. The training includes only the  $Z \rightarrow \tau\tau$  background and the VBF signal. The MC statistics used in the training are half those available after all signal region cuts (as the other half are later used to test the training). This corresponds to  $\approx 5,000$   $Z\tau\tau$  events and  $\approx 100,000$  VBF events.

The TMVA BDTG interface is used to train and test the BDT. The optimal parameters were found through a scan of reasonable values and the final set is summarized in Table 6.1. For this BDT we aim to take advantage of the different  $E_{\text{T}}^{\text{miss}}$  distributions in  $Z \rightarrow \tau\tau$  backgrounds and VBF signal Monte Carlo events. Instead of a cut on  $E_{\text{T}}^{\text{miss}}$ ,

## CHAPTER 6. BACKGROUNDS AND SYSTEMATICS

Parameter	Value	Range
Boosting algorithm	Gradient	–
Maximum tree depth	22	[3,10,22,30]
Number of trees	1000	[200,1000,10000]
Minimum number of events requires per mode	5%	[5%]
Number of cuts	7	[3,5,7,9]

Table 6.1: BDT parameters used for the  $Z \rightarrow \tau\tau$  training.

we train the BDT using multiple different  $E_T^{\text{miss}}$  variables to maximize discrimination and then cut on the BDT output variable. Training using variables including  $E_T^{\text{miss}}$ ,  $E_T^{\text{miss, track}}$ ,  $E_{T,\text{rel}}^{\text{miss}}$ ,  $E_{T,\text{rel}}^{\text{miss, track}}$ ,  $\Delta\phi_{\ell\ell, E_T^{\text{miss}}}$ ,  $\Delta\phi_{\ell\ell, E_T^{\text{miss, track}}}$ , and  $E_T^{\text{miss, significance}}$  have been tested. The optimal analysis uses  $E_T^{\text{miss, significance}}$ ,  $E_T^{\text{miss, track}}$ ,  $E_{T,\text{rel}}^{\text{miss}}$ , and  $E_{T,\text{rel}}^{\text{miss, track}}$ ,  $\Delta\phi_{\ell\ell, E_T^{\text{miss, track}}}$ , and  $\Delta\phi_{\ell\ell, E_T^{\text{miss}}}$ . Relative  $E_T^{\text{miss}}$  is defined as  $E_T^{\text{miss}} * \sin(|\Phi_{E_T^{\text{miss}}} \Phi_{jet}|)$ ,  $E_T^{\text{miss, track}}$  is calculated from tracking detectors while  $E_T^{\text{miss}}$  is calculated from calorimeter deposits. Finally,  $E_T^{\text{miss, significance}}$  is a newly calibrated variable from the Jet/ $E_T^{\text{miss}}$  group that differentiates between  $E_T^{\text{miss}}$  from electroweak and strong interactions [30]. While  $E_T^{\text{miss, significance}}$  wasn't shown to increase the discrimination of the BDT due to its high correlations with  $E_T^{\text{miss}}$ , replacing this variable with  $E_T^{\text{miss}}$  showed very similar results while reducing correlations between variables like  $E_{T,\text{rel}}^{\text{miss}}$  and  $\Delta\phi_{\ell\ell, E_T^{\text{miss}}}$ . Plots shown in 6.2 and 6.3 demonstrate the input distributions used to train the BDT and their correlations. The BDT training successfully separates  $Z \rightarrow \tau\tau$  and VBF signal. In order to quantify the discrimination we use the integrated-ROC calculated through TMVA for unweighted normalized samples and find an optimal value of 0.897. Comparisons between the test and training show that the BDT is un-biased- differences between testing and training samples would imply overtraining, or the BDT using to many parameters on too few events. Visually, once can see that the testing and trainings samples are quite similar. Additionally, a Kolmogorov-Smirnov test is performed to measure if the two test and training distributions differ significantly. If the two distributions are random samples of the

## CHAPTER 6. BACKGROUNDS AND SYSTEMATICS

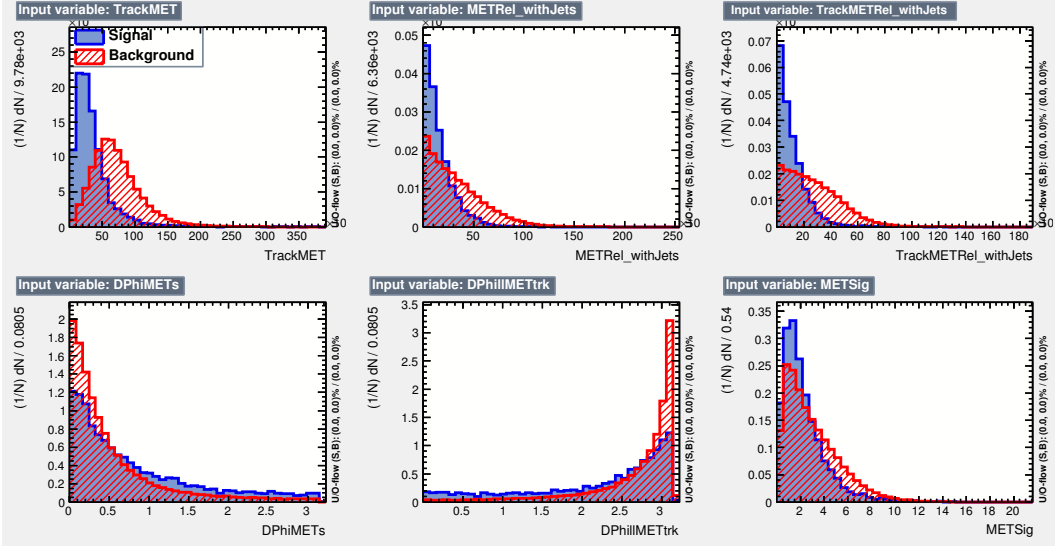


Figure 6.2: Distributions of input variables to  $Z \rightarrow \tau\tau$  BDT. Samples are unweighted and normalized to even numbers of background and signal events. Signal represents  $Z \rightarrow \tau\tau$  and background VBF Higgs.

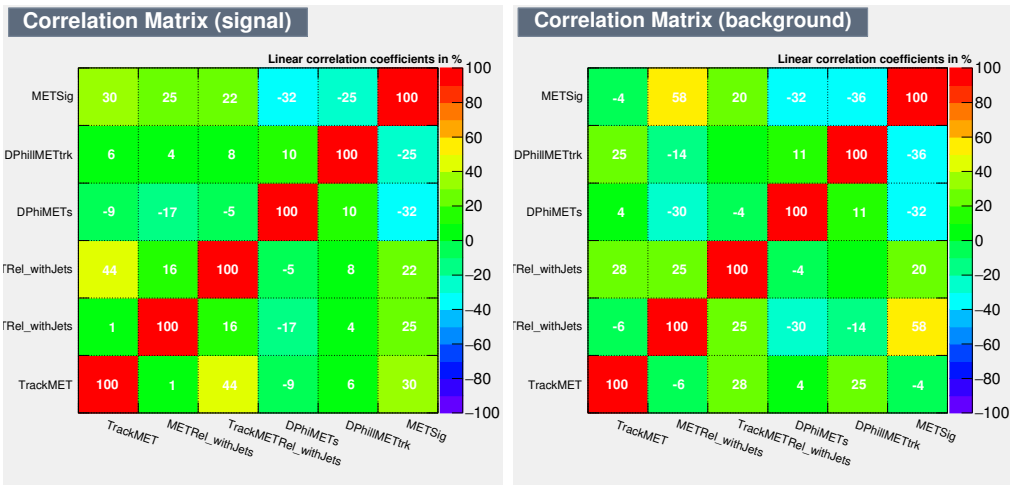


Figure 6.3: Correlations of input variables to  $Z \rightarrow \tau\tau$  BDT. Signal represents  $Z \rightarrow \tau\tau$  and background VBF Higgs.

## CHAPTER 6. BACKGROUNDS AND SYSTEMATICS

same parent distribution, the KS-test would give a uniformly distributed value between zero and one (or an average value of 0.5). The closer to 0.5 the KS-test, the greater likelihood the curves come from the same parent, however this calculation is heavily skewed toward lower values so any value above zero (or not very close to zero, on order  $10^{-4}$ ) can be considered not indicative of overtraining. For signal and background we find KS-test values of 0.062 and 0.286, and so no evidence of over-training. We can visualize the BDT output variable both on un-weighted normalized samples and on samples with all event weights applied. The following plots show BDT results applied to un-weighted and weighted samples of  $Z \rightarrow \tau\tau$  and VBF signal.

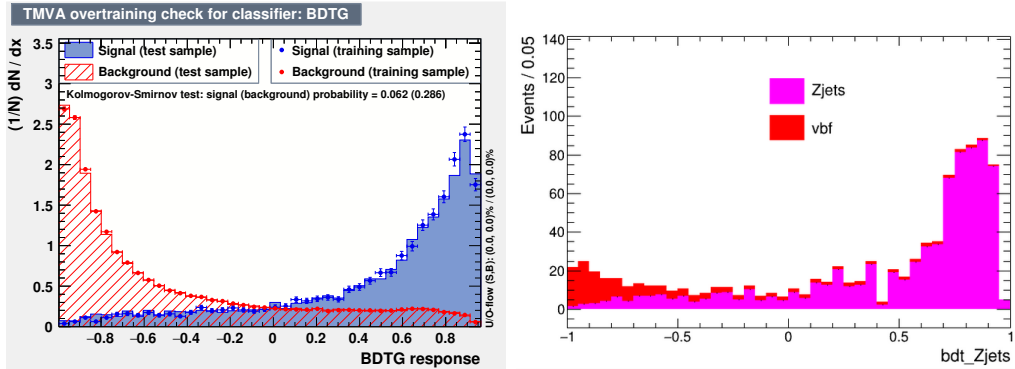


Figure 6.4: Weighted, normalized samples of  $Z \rightarrow \tau\tau$  (signal) and VBF (background) plotted over BDT output distribution on left, overlaid testing and training samples shown. On right, full weighted samples of  $Z \rightarrow \tau\tau$  and VBF signal plotted over BDT output distributions.

Finally, we can test how other background samples distribute with the  $Z \rightarrow \tau\tau$  BDT output variable and optimize results from cutting on this variable. The following plot ?? shows distribution of all backgrounds as well as signal with  $Z \rightarrow \tau\tau$  BDT output. We aim to increase significance while also keeping as much signal sample as possible for keep high statistics. To accomplish this we cut at a BDT output value of 0.5, in this way we eliminate 60% of  $Z \rightarrow \tau\tau$  background, or  $\approx 450$  events, and only 6% of signal events. We have also tested this cut on truth samples to validate that applying this cut does not affect our fiducial

## CHAPTER 6. BACKGROUNDS AND SYSTEMATICS

phase space.

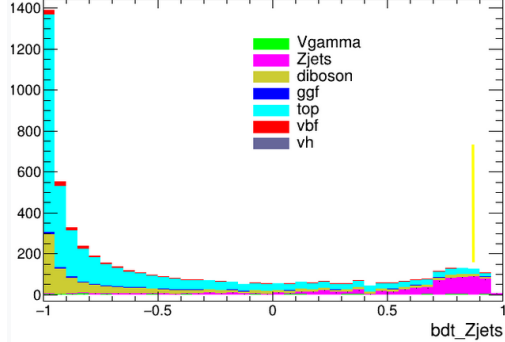


Figure 6.5: Full weighted samples of all signal and background plotted over BDT output distributions

### Drell-Yan Control Region

The  $Z$ +jets control region definition is quite similar to the VBF signal region except that the  $Z$ +jets veto cuts are inverted. Thus instead of removing events near the  $Z$ -mass window we select for them by applying a cut on  $m_{ll} < 80$  GeV,  $66.2$  GeV  $< m_{\tau\tau} < 116.2$  GeV, and the same OLV and CJV cuts as in the VBF signal region as well as a cut on the  $Z$ +jets BDT reversing that on the signal region ( $\text{BDT}_{Z\text{jets}} > 0.5$ ). The  $Z$ +jets control region has a purity of  $\approx 82\%$  and yields in this region are shown in the table below.

$\sqrt{s} = 13\text{TeV}$ , $\mathcal{L} = 139\text{fb}^{-1}$ (Full Run 2)	$H_{VBF}$	$H_{ggF}$	$WW$	Other VV	Top	Zjets	Mis-Id	Total Bkg	Significance	Data	Data/MC
<b>Scale factors</b>					<b>NF = 0.99 ± 0.01</b>	<b>NF = 1.03 ± 0.05</b>		<b>NFs Applied</b>			
$Z \rightarrow \tau\tau$ CR: $ m_{\tau\tau} - m_Z  < 25$ , bVeto	$27.15 \pm 0.16$	$67.22 \pm 0.76$	$1809.83 \pm 8.26$	$394.27 \pm 4.91$	$5630.06 \pm 17.10$	$9040.34 \pm 45.91$	$507.91 \pm 26.88$	$17449.63 \pm 56.70$	$0.21 \pm 0.00$	$16400$	$0.94 \pm 0.01$
<b>Scale factors</b>					<b>NF = 0.99 ± 0.01</b>	<b>NF = 1.03 ± 0.05</b>		<b>NFs Applied</b>			
$Z \rightarrow \tau\tau$ CR: $M_{ll} < 80$ GeV	$26.48 \pm 0.16$	$64.96 \pm 0.75$	$589.77 \pm 4.57$	$221.55 \pm 4.43$	$1702.27 \pm 9.24$	$8802.21 \pm 41.65$	$284.22 \pm 21.72$	$11664.97 \pm 48.30$	$0.25 \pm 0.00$	$10805$	$0.92 \pm 0.01$
<b>Scale factors</b>					<b>NF = 0.99 ± 0.01</b>	<b>NF = 1.03 ± 0.05</b>		<b>NFs Applied</b>			
$Z \rightarrow \tau\tau$ CR: $\text{CJV} < 20$ GeV	$20.86 \pm 0.14$	$46.58 \pm 0.63$	$419.89 \pm 3.94$	$161.68 \pm 4.14$	$1149.53 \pm 7.66$	$6569.13 \pm 36.52$	$224.08 \pm 18.68$	$8570.90 \pm 42.12$	$0.23 \pm 0.00$	$7931$	$0.92 \pm 0.01$
<b>Scale factors</b>					<b>NF = 0.99 ± 0.01</b>	<b>NF = 1.03 ± 0.05</b>		<b>NFs Applied</b>			
$Z \rightarrow \tau\tau$ CR: OLV	$16.04 \pm 0.12$	$11.63 \pm 0.32$	$86.60 \pm 1.87$	$34.00 \pm 1.35$	$291.98 \pm 3.89$	$1413.62 \pm 17.49$	$30.62 \pm 8.22$	$1868.45 \pm 19.85$	$0.37 \pm 0.00$	$1832$	$0.97 \pm 0.02$
<b>Scale factors</b>					<b>NF = 0.99 ± 0.01</b>	<b>NF = 1.03 ± 0.05</b>		<b>NFs Applied</b>			
BDT Zjets $> 0.5$	$3.52 \pm 0.06$	$4.42 \pm 0.20$	$34.38 \pm 1.27$	$13.76 \pm 1.03$	$106.25 \pm 2.36$	$809.42 \pm 14.54$	$9.33 \pm 6.18$	$977.56 \pm 16.06$	$0.11 \pm 0.00$	$979$	$1.00 \pm 0.04$

Table 6.2: Cutflow in the  $Z$ +jets control region.

Data/MC shows decent agreement over various variable distributions as seen in the below.

In particular, modelling over variables used in the BDT are modelled well.

## CHAPTER 6. BACKGROUNDS AND SYSTEMATICS

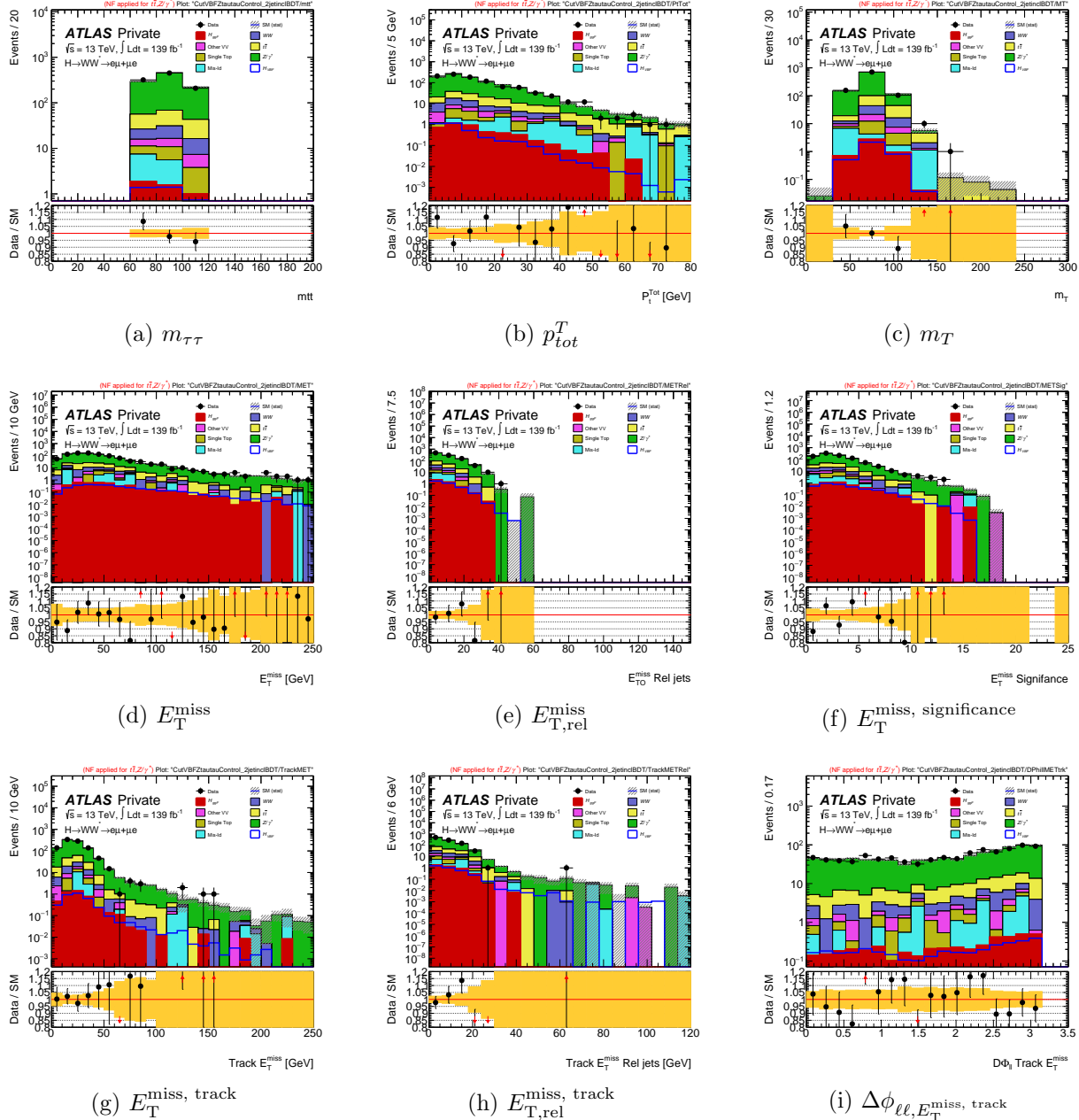


Figure 6.6: Distributions of  $m_{\tau\tau}$ ,  $p_T^T$ ,  $m_T$ , in  $E_{\text{T,rel}}^{\text{miss}}$ ,  $E_T^{\text{miss, significance}}$ ,  $E_T^{\text{miss, track}}$ ,  $E_{\text{T,rel}}^{\text{miss, track}}$ ,  $\Delta\phi_{\ell\ell, E_T^{\text{miss, track}}}$  in the  $Z + \text{jets}$  control region.

The BDT that discriminates VBF signal and  $Z + \text{jets}$  is applied in the  $Z + \text{jets}$  control region to maintain orthogonality. This further increases purity in the control region. This

## CHAPTER 6. BACKGROUNDS AND SYSTEMATICS

distribution is shown in the following plot. Normalization factors (NF) are derived in the

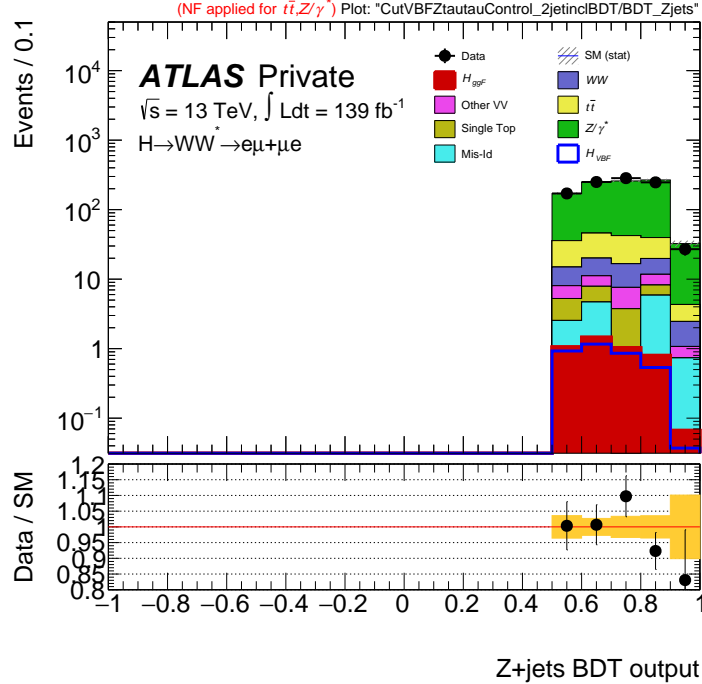


Figure 6.7: Full weighted samples of all signal and background plotted over BDT output distributions in  $Z$ +jets control region after cut on  $Z$ +jets BDT

$Z$ +jets control region to correct for Data/MC mis-modelling. These factors are applied to the  $Z$ +jets sample in the signal region. The NF factors are  $1.03 \pm 0.05$ .

### 6.1.2 Top background

The top background consists of two main components,  $Wt$  and  $t\bar{t}$  events where the  $W$  decays leptonically and the top quarks decay to jets (notably  $b$ -jets). The top background is dominated by  $t\bar{t}$  and is the largest background in our signal region, composing about 60% of the total background. Though top backgrounds are numerous, discrimination between top and signal Higgs events is possible through training a BDT on variables that have very different distributions between these two types of events like  $m_{\ell\ell}$  and  $\Delta Y_{jj}$ . This BDT

## CHAPTER 6. BACKGROUNDS AND SYSTEMATICS

discriminates between signal and top background quite well and so the top background is defined in the signal region and separated using this variable. The final BDT used in the final statistical fit is discussed in the following chapter. We define a top validation region to test top Monte Carlo modelling as well as to calculate a normalization factor that is used to correct top mis-modelling in the signal region. The top validation region is described similarly to the signal region with one major difference, a  $b$ -tag applied in the signal region requiring all events with a  $b$ -jet to be removed is (almost) reversed. Instead we require exactly one  $b$ -tagged jet. We require exactly one in order to define the validation region as similarly to the signal region as possible while increasing top purity. The results is a highly pure top validation region where the flavor composition of the tagged jets is close to the signal region. Purity of the top control region is  $\approx 97\%$  and yields in this region are shown in the table below.

$\sqrt{s} = 13 TeV, \mathcal{L} = 139 fb^{-1}$ (Full Run 2)	$H_{VBF}$	$H_{ggF}$	$WW$	Other VV	Top	Zjets	Mis-Id	Total Bkg	Significance	Data	Data/MC
Scale factors					$NF = 0.99 \pm 0.01$	$NF = 1.03 \pm 0.05$		$NFs$ Applied			
$n_{b-jets} = 1$	$39.79 \pm 0.19$	$129.20 \pm 1.08$	$2993.57 \pm 9.53$	$690.94 \pm 4.40$	$349498.67 \pm 128.68$	$3739.16 \pm 34.69$	$4824.17 \pm 101.77$	$361875.73 \pm 168.02$	$0.07 \pm 0.00$	$359758$	$0.99 \pm 0.00$
Scale factors					$NF = 0.99 \pm 0.01$	$NF = 1.03 \pm 0.05$		$NFs$ Applied			
$Z \rightarrow \tau\tau$ veto	$18.05 \pm 0.13$	$18.70 \pm 0.42$	$175.96 \pm 2.68$	$43.24 \pm 1.19$	$29996.21 \pm 38.10$	$183.57 \pm 8.79$	$287.05 \pm 30.06$	$30704.73 \pm 49.41$	$0.10 \pm 0.00$	$30709$	$1.00 \pm 0.01$
Scale factors					$NF = 0.99 \pm 0.01$	$NF = 1.03 \pm 0.05$		$NFs$ Applied			
$CJV < 20$ GeV	$29.69 \pm 0.17$	$84.86 \pm 0.88$	$1905.77 \pm 7.80$	$454.48 \pm 3.81$	$238439.98 \pm 107.23$	$2524.42 \pm 30.90$	$3083.10 \pm 83.79$	$246492.61 \pm 139.83$	$0.06 \pm 0.00$	$244811$	$0.99 \pm 0.00$
Scale factors					$NF = 0.99 \pm 0.01$	$NF = 1.03 \pm 0.05$		$NFs$ Applied			
OLV	$20.85 \pm 0.14$	$20.90 \pm 0.44$	$294.56 \pm 3.34$	$76.17 \pm 1.52$	$46224.53 \pm 47.42$	$507.30 \pm 13.10$	$427.86 \pm 36.88$	$47551.32 \pm 61.60$	$0.10 \pm 0.00$	$47182$	$0.99 \pm 0.00$
Scale factors					$NF = 0.99 \pm 0.01$	$NF = 1.03 \pm 0.05$		$NFs$ Applied			
$Z \rightarrow \tau\tau$ veto	$18.05 \pm 0.13$	$18.70 \pm 0.42$	$175.96 \pm 2.68$	$43.24 \pm 1.19$	$29996.21 \pm 38.10$	$183.57 \pm 8.79$	$287.05 \pm 30.06$	$30704.73 \pm 49.41$	$0.10 \pm 0.00$	$30709$	$1.00 \pm 0.01$

Table 6.3: Cutflow in the top control region.

Data/MC in the top validation region shows good agreement over various variable distributions as seen in the below.

The BDT to discriminate top background from VBF signal events is trained and applied in the signal region and so described in the next chapter, but its distribution in the top validation region is shown below. This BDT discriminates both WW and top (combined) against the VBF signal as they have similar kinematic distributions and are treated together in the final simultaneous fit.

A designated BDT discriminates between top and WW backgrounds and is described fur-

## CHAPTER 6. BACKGROUNDS AND SYSTEMATICS

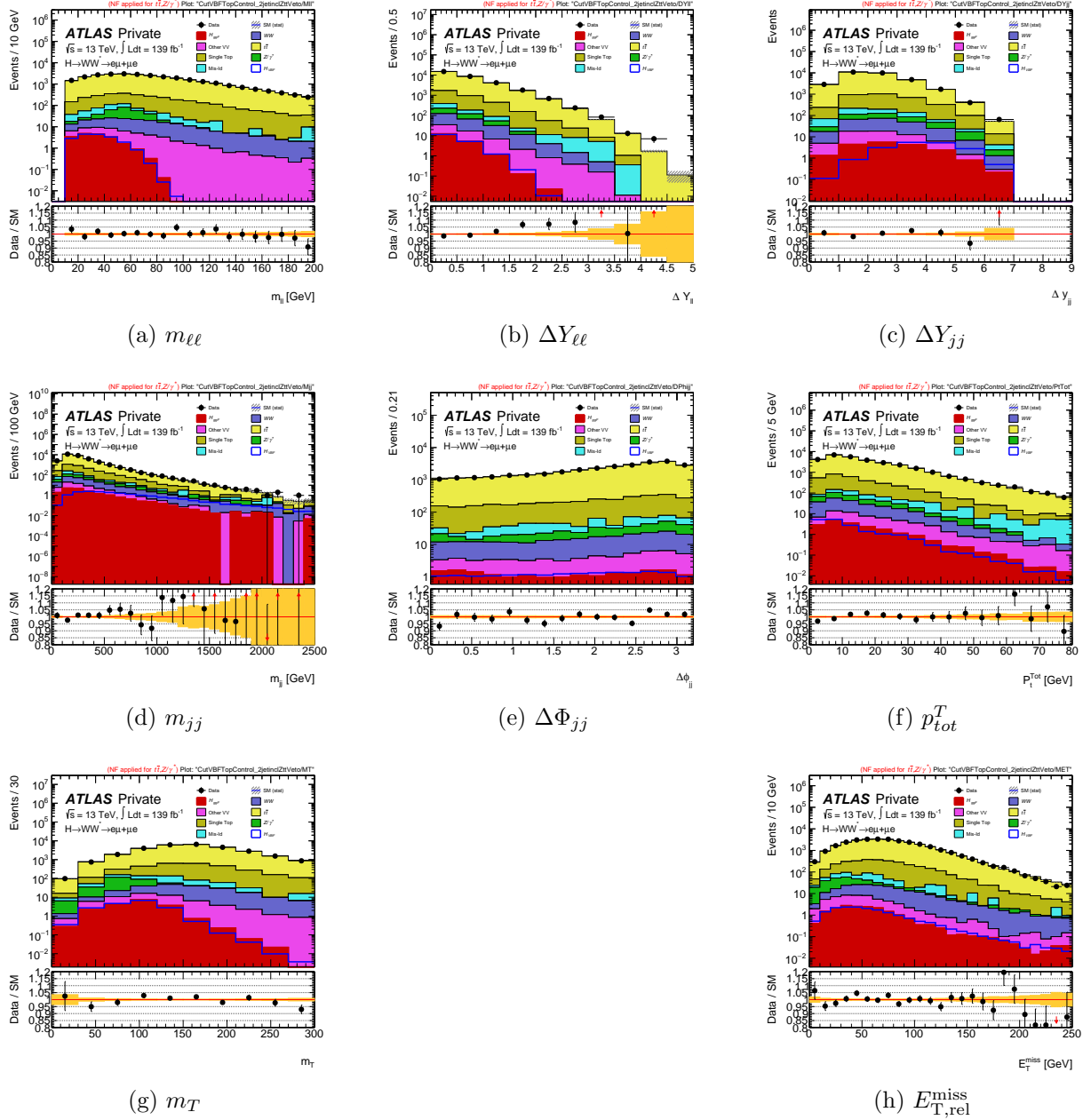


Figure 6.8: Distributions of  $m_{\ell\ell}$ ,  $\Delta Y_{\ell\ell}$ ,  $\Delta Y_{jj}$ ,  $m_{jj}$ ,  $\Delta\Phi_{jj}$ ,  $p_{\text{tot}}^T$ ,  $m_T$ , and  $E_{\text{T},\text{rel}}^{\text{miss}}$  in the top validation region.

ther in the WW background section (next). However, this distribution in the top validation region with all weighted samples is shown below.

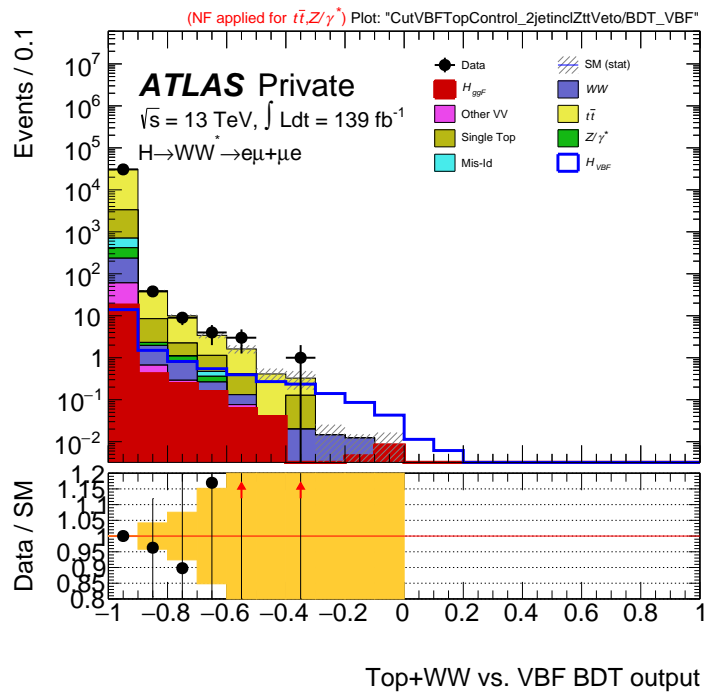


Figure 6.9: Full weighted samples of all signal and background plotted over Top +  $WW$  vs. VBF BDT output distributions in top validation region

## CHAPTER 6. BACKGROUNDS AND SYSTEMATICS

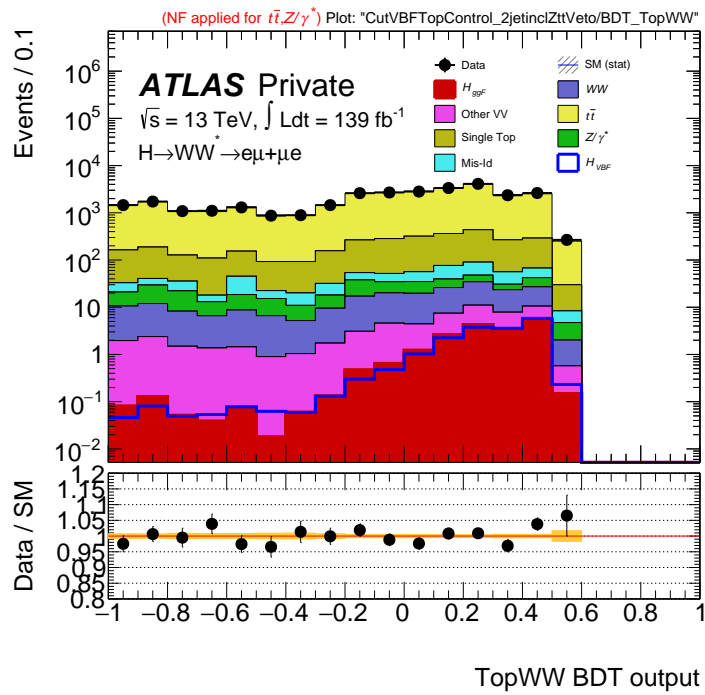


Figure 6.10: Full weighted samples of all signal and background plotted over Top vs.  $WW$  BDT output distributions in top validation region

## CHAPTER 6. BACKGROUNDS AND SYSTEMATICS

Normalization factors (NF) are derived in the top validation region to correct for data/MC mis-modelling. These factors are applied to the top sample in the signal region. The NF factors are  $0.99 \pm 0.01$ .

### 6.1.3 Diboson background

The  $WW$  background consists primarily of QCD  $WW$ +jets events (highly dominating electroweak vertices). This background is estimated along with the top background using a joint parameter due to their similarities in signature as well as the difficulty in defining a pure  $WW$  control region (without top contamination). A  $WW$  validation region is defined to demonstrate  $WW$  MC modelling in a targeted  $WW$  region. The  $WW$  validation region is defined with at least 2 jets, a  $b$ -veto  $N_{b-jet} < 1$  and a central-jet-veto of below 20GeV as in the signal region. Two additional cuts differ from the signal region -  $m_T > 130\text{GeV}$  and  $m_{T2} > 160\text{GeV}$  where  $m_{T2}$  is defined as

$$m_{T2} = \min_{p_T^1 + p_T^2 = p_T} (\max(m_T^2(p_T^1, p_T^a), m_T^2(p_T^2, p_T^b))) \quad (6.1)$$

This represents a lower bound on the parent particle's mass, so using a large  $m_{T2}$  cut eliminates contamination from many  $t\bar{t}$  decays which have an upper limit near the top mass. The purity of the region is  $\approx 37\%$  and the cutflow for this region is shown below.

$\sqrt{s} = 13\text{TeV}, \mathcal{L} = 139\text{fb}^{-1}$ (Full Run 2)	$H_{VBF}$	$H_{ggF}$	$WW$	Other VV	Top	Zjets	Mis-Id	Total Bkg	Significance	Data	Data/MC
Scale factors					<b>NF = 0.99 ± 0.01</b>	<b>NF = 1.03 ± 0.05</b>					
b-veto	$323.67 \pm 0.54$	$914.43 \pm 2.86$	$21075.69 \pm 28.85$	$2701.86 \pm 10.03$	$63729.30 \pm 57.17$	$22477.17 \pm 104.35$	$4407.46 \pm 70.33$	$115305.91 \pm 141.58$	$0.95 \pm 0.00$	$109677$	$0.95 \pm 0.00$
Scale factors					<b>NF = 0.99 ± 0.01</b>	<b>NF = 1.03 ± 0.05</b>					
$M_T, 130\text{ GeV}$	$32.37 \pm 0.17$	$130.66 \pm 1.09$	$16127.61 \pm 24.93$	$1573.71 \pm 6.42$	$50042.33 \pm 50.78$	$885.51 \pm 34.16$	$2078.63 \pm 49.84$	$70838.44 \pm 83.03$	$0.12 \pm 0.00$	$68255$	$0.96 \pm 0.00$
Scale factors					<b>NF = 0.99 ± 0.01</b>	<b>NF = 1.03 ± 0.05</b>					
$M_{T2}, 160\text{ GeV}$	$18.87 \pm 0.13$	$50.22 \pm 0.67$	$6528.07 \pm 14.33$	$591.47 \pm 3.59$	$11542.51 \pm 24.79$	$306.95 \pm 14.38$	$602.98 \pm 26.34$	$19622.20 \pm 41.64$	$0.13 \pm 0.00$	$18672$	$0.95 \pm 0.01$
Scale factors					<b>NF = 0.99 ± 0.01</b>	<b>NF = 1.03 ± 0.05</b>					
CJV (20GeV)	$13.61 \pm 0.11$	$32.51 \pm 0.54$	$4363.49 \pm 11.96$	$385.58 \pm 2.86$	$6410.03 \pm 18.98$	$187.58 \pm 13.07$	$392.37 \pm 20.45$	$11771.56 \pm 33.18$	$0.13 \pm 0.00$	$11245$	$0.95 \pm 0.01$

Table 6.4: Cutflow in the  $WW$  validation region.

Data/MC shows good agreement over various variable distributions as seen in the below.

## CHAPTER 6. BACKGROUNDS AND SYSTEMATICS

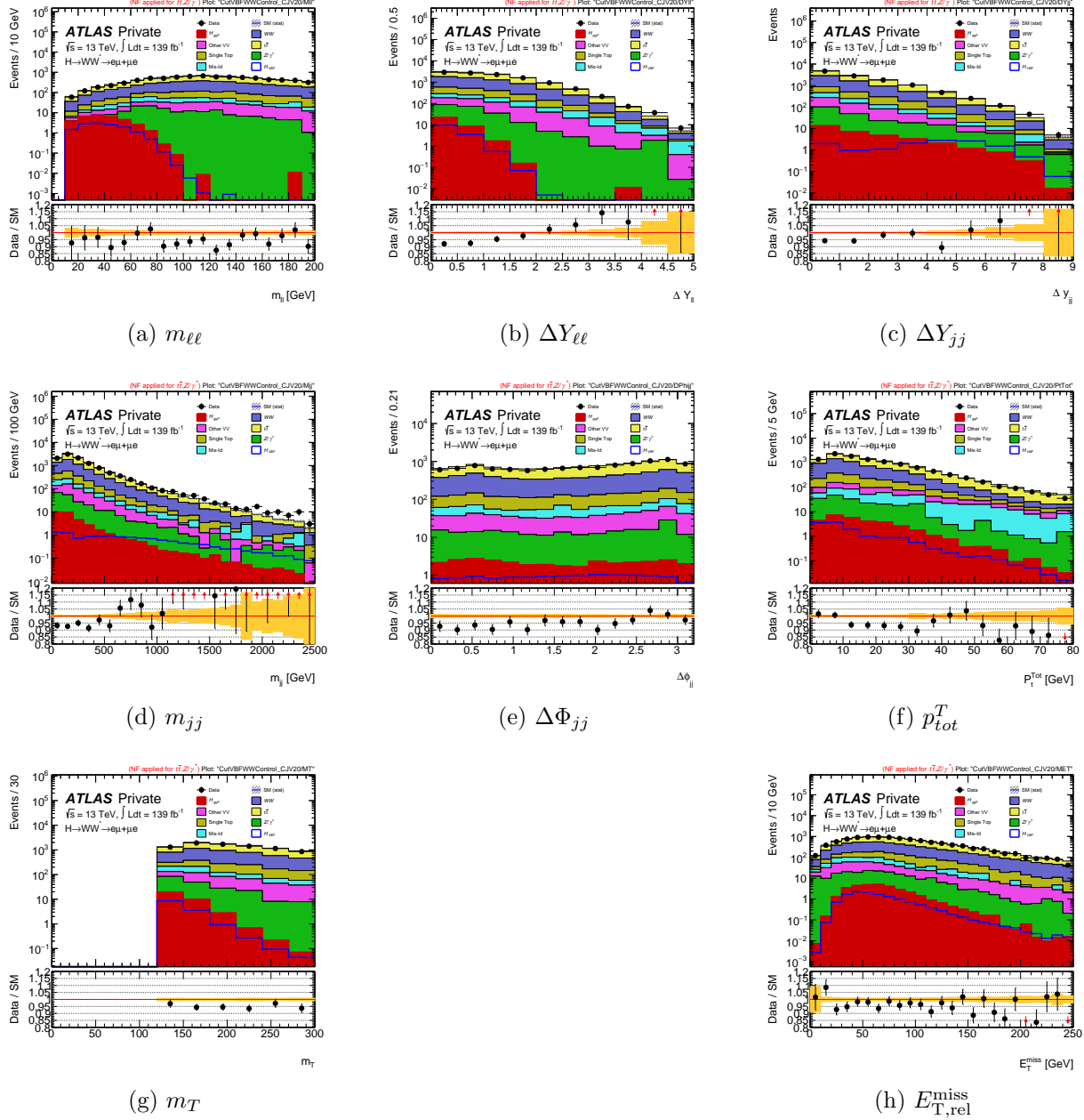


Figure 6.11: Distributions of  $m_{\ell\ell}$ ,  $\Delta Y_{\ell\ell}$ ,  $\Delta Y_{jj}$ ,  $m_{jj}$ ,  $\Delta\Phi_{jj}$ ,  $p_{tot}^T$ ,  $m_T$ , and  $E_{T,\text{rel}}^{\text{miss}}$  in the  $WW$  validation region.

The BDT to discriminate  $WW$  background from VBF signal events is trained and applied in the signal region and so described in the next chapter, but its distribution in the  $WW$

## CHAPTER 6. BACKGROUNDS AND SYSTEMATICS

validation region is shown below. This BDT discriminates both WW and top (combined) against the VBF signal as they have similar kinematic distributions and are treated together in the final simultaneous fit.

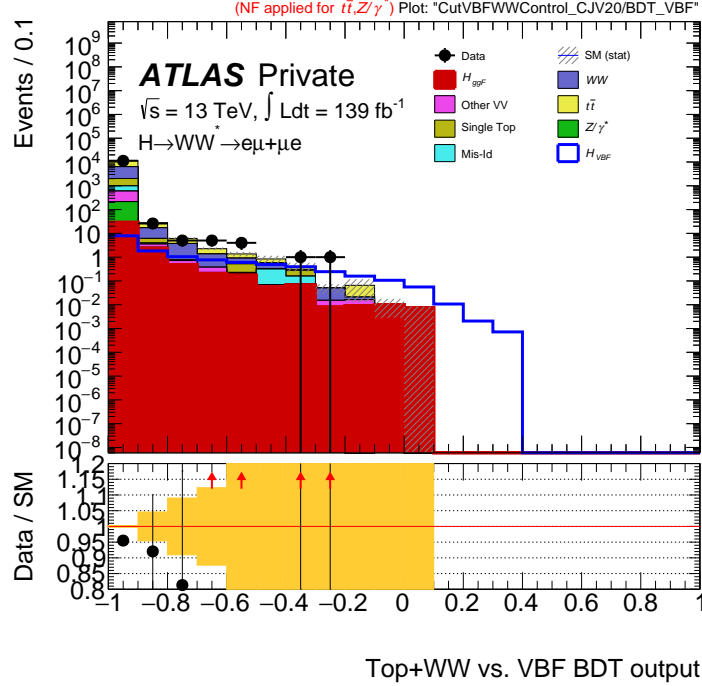


Figure 6.12: Full weighted samples of all signal and background plotted over Top +  $WW$  vs. VBF BDT output distributions in  $WW$  validation region

A designated BDT discriminates between top and WW backgrounds in the signal region...  
**need to put in BDT training information, Sagar?**

### 6.1.4 ggF background

The Higgs production via gluon–gluon fusion is estimated simultaneously from three control regions and the signal region. The control regions are chosen such as the both to minimize both the statistical and the modelling uncertainties, in particular these originating from the modelling of higher order QCD corrections. In particular, the regions inspired from

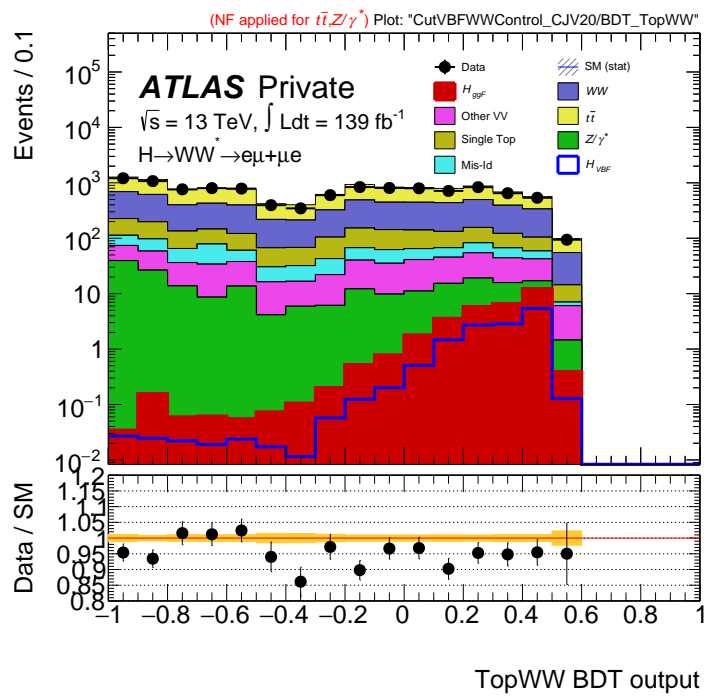


Figure 6.13: Full weighted samples of all signal and background plotted over BDT output distributions in WW validation region

## CHAPTER 6. BACKGROUNDS AND SYSTEMATICS

a subdivision based on the jet multiplicity. The first region, CRGGF1, is build based from the preselection and selecting events with 0 and 1 jet. The second and third regions, are constructed starting from the preselection and inverting the VBF selection cuts, such as to minimize the extrapolation uncertainties to the signal region. In particular, the definitions are the following:

- **GGF-CR1** Preselection criteria and  $N_j < 2$ .
- **GGF-CR2** Preselection criteria and  $CJV > 1$  and  $OLV > 1$
- **GGF-CR3** Preselection criteria and  $CJV < 1$  and  $OLV > 1$  or  $CJV > 1$  and  $OLV < 1$

from this the expectation in the signal region is build from the following ratio, inspired from the ABCD method,

$$\mu_{GGF-SR} = \frac{\mu_1^{GGF-CR} \cdot \mu_2^{GGF-CR}}{\mu_3^{GGF-CR}}. \quad (6.2)$$

where  $\mu_{GGF-X}$  denotes the yield modifier in each region GGF-X not extalised to the expectation from simulation. The final event yield in the signal region  $\mu_{GGF-SR}$  is detetextined in the simultaneous fit as described in Sec ???. In each *ggF* category the *ggF* yield is extracted from simulation-extracted template fits based on dedicated discriminants.

For each category, a dedicated multivariate discriminant is trained and applied to discriminate between *ggF* and the backgrounds. Each of these trainings is discussed next.

### Discriminant in the GGF-CR1

The multivariate discriminate used for the GGF CR1 is a boosted decision tree (BDT) trained using  $e\mu + \mu e$  events that pass all ggF CR1 cuts. The training includes ggF events trained against VBF signal and all backgrounds. The MC statistics used in the training are half those available after the ggF CR1 cuts (as the other half are later used to test the

## CHAPTER 6. BACKGROUNDS AND SYSTEMATICS

training). This corresponds to  $\approx 3,200$  ggF events and  $\approx 480,000$  other signal and background events.

The TMVA BDTG interface is used to train and test the BDT. The optimal parameters were found through a scan of reasonable values and the final set is summarized in Table 6.5. For this BDT various distributions are used to take advantage of differences in distributions

Parameter	Value
Boosting algorithm	Gradient
Maximum tree depth	10
Number of trees	100
Minimum number of events requires per mode	5%
Number of cuts	7

Table 6.5: BDT parameters used for the ggF CR1 training.

between ggF events and other sample types. These variables include  $\Delta Y_{\ell\ell}$ ,  $\Delta\Phi_{\ell\ell,m_{\ell\ell},m_T,p_{tot}^T}$ , lep  $p_{\text{lead}}^T$ , lep  $p_{\text{sublead}}^T$ , jet  $p_{\text{lead}}^T$ , jet  $p_{\text{sublead}}^T$ ,  $\Delta\Phi_{jj}$ , and  $E_{\text{T,rel}}^{\text{miss}}$ . Distributions for these variables in the ggF CR1 region where the BDT is trained are shown below demonstrating data/MC modelling for each.

Plots shown in 6.15 and 6.16 demonstrate the input distributions used to train the BDT and their correlations where each distribution is unweighted and normalized to equal number of background and signal events.

In order to quantify the discrimination we use the integrated-ROC calculated through TMVA for unweighted normalized samples and find an optimal value of 0.896. Comparisons between the test and training show that the BDT is un-biased- differences between testing and training samples would imply overtraining, or the BDT using too many parameters on too few events. Visually, one can see that the testing and training samples are quite similar. Additionally, a Kolmogorov-Smirnov test is performed to measure if the two test and training distributions differ significantly and no evidence of over-training is present. We can visualize

## CHAPTER 6. BACKGROUNDS AND SYSTEMATICS

the BDT output variable both on un-weighted normalized samples and on samples with all event weights applied. The following plots show BDT results applied to un-weighted and weighted samples.

### Discriminant in the GGF-CR2

The multivariate discriminate used for the GGF CR2 is a boosted decision tree (BDT) trained using  $e\mu + \mu e$  events that pass all ggF CR2 cuts. The training includes ggF events trained against VBF signal and all backgrounds. The MC statistics used in the training are half those available after ggF CR2 cuts (as the other half are later used to test the training). This corresponds to  $\approx 3,200$  ggF events and  $\approx 480,000$  other signal and background events.

The TMVA BDTG interface is used to train and test the BDT. The optimal parameters were found through a scan of reasonable values and the final set is summarized in Table 6.6. For this BDT various distributions are used to take advantage of differences in distributions

Parameter	Value
Boosting algorithm	Gradient
Maximum tree depth	10
Number of trees	100
Minimum number of events requires per mode	5%
Number of cuts	7

Table 6.6: BDT parameters used for the ggF CR2 training.

between ggF events and other sample types. These variables include  $\Delta Y_{\ell\ell}$ ,  $\Delta\Phi_{\ell\ell, m_{\ell\ell}, m_T, p_{tot}^T}$ , lep  $p_{\text{lead}}^T$ , lep  $p_{\text{sublead}}^T$ , jet  $p_{\text{lead}}^T$ , jet  $p_{\text{sublead}}^T$ ,  $\Delta\Phi_{jj}$ , and  $E_{\text{T,rel}}^{\text{miss}}$ . Distributions for these variables in the ggF CR2 region where the BDT is trained are shown below demonstrating data/MC modelling for each.

Plots shown in 6.19 and 6.20 demonstrate the input distributions used to train the BDT and their correlations where each distribution is unweighted and normalized to equal number

## CHAPTER 6. BACKGROUNDS AND SYSTEMATICS

of background and signal events.

In order to quantify the discrimination we use the integrated-ROC calculated through TMVA for unweighted normalized samples and find an optimal value of 0.910. Comparisons between the test and training show that the BDT is un-biased- differences between testing and training samples would imply overtraining, or the BDT using to many parameters on too few events. Visually, once can see that the testing and trainings samples are quite similar. Additionally, a Kolmogorov-Smirnov test is performed to measure if the two test and training distributions differ significantly and no evidence of over-training is present. We can visualize the BDT output variable both on un-weighted normalized samples and on samples with all event weights applied. The following plots show BDT results applied to un-weighted and weighted samples.

### Discriminant in the GGF-CR3

The multivariate discriminate used for the GGF CR3 is a boosted decision tree (BDT) trained using  $e\mu + \mu e$  events that pass all ggF CR3 cuts. The training includes only ggF events trained against VBF signal and all backgrounds. The MC statistics used in the training are half those available after the ggF CR3 cuts (as the other half are later used to test the training). This corresponds to  $\approx 3,200$  ggF events and  $\approx 480,000$  other signal and background events.

The TMVA BDTG interface is used to train and test the BDT. The optimal parameters were found through a scan of reasonable values and the final set is summarized in Table 6.7. For this BDT various distributions are used to take advantage of differences in distributions between ggF events and other samples types. These variables include  $\Delta Y_{\ell\ell}$ ,  $\Delta\Phi_{\ell\ell}, m_{\ell\ell}, m_T, p_{tot}^T$ , lep  $p_{\text{lead}}^T$ , lep  $p_{\text{sublead}}^T$ , and  $E_T^{\text{miss}}$ . Distributions for these variables in the ggF CR3 region where the BDT is trained are shown below demonstrating data/MC modelling for each.

## CHAPTER 6. BACKGROUNDS AND SYSTEMATICS

Parameter	Value
Boosting algorithm	Gradient
Maximum tree depth	10
Number of trees	1000
Minimum number of events requires per mode	5%
Number of cuts	7

Table 6.7: BDT parameters used for the ggF CR3 training.

Plots shown in [6.23](#) and [6.24](#) demonstrate the input distributions used to train the BDT and their correlations where each distribution is unweighted and normalized to equal number of background and signal events.

In order to quantify the discrimination we use the integrated-ROC calculated through TMVA for unweighted normalized samples and find an optimal value of 0.901. Comparisons between the test and training show that the BDT is un-biased- differences between testing and training samples would imply overtraining, or the BDT using too many parameters on too few events. Visually, one can see that the testing and trainings samples are quite similar. Additionally, a Kolmogorov-Smirnov test is performed to measure if the two test and training distributions differ significantly and no evidence of over-training is present. We can visualize the BDT output variable both on un-weighted normalized samples and on samples with all event weights applied. The following plots show BDT results applied to un-weighted and weighted samples.

### Dependance on the modelling of the simulation

This method detetextines *ggF* the background entirely from data and, thus, the sensitivity to migration of events from one region to the other is greatly reduced. In order to study this, pseudo-experiments were thrown using Asimov data-sets. For each toy set the input yield for each region was varied independently in the range of  $0 < \mu_{\text{GGF-X}} < 2$  at generation level.

## CHAPTER 6. BACKGROUNDS AND SYSTEMATICS

Param name	Patextam Val	$\Delta ggFCRNj1$	$\Delta ggFCRNj2$	$\Delta ggFCRNj3$
$\mu_{VBF}$	$1.00^{+0.36}_{-0.33}$	0.10	0.10	0.10
$\mu_{VBF}$	$1.00^{+0.34}_{-0.31}$	0.10	0.10	0.50
$\mu_{VBF}$	$1.00^{+0.33}_{-0.30}$	0.10	0.10	1.00
$\mu_{VBF}$	$1.00^{+0.36}_{-0.33}$	0.10	0.50	0.10
$\mu_{VBF}$	$1.00^{+0.34}_{-0.31}$	0.10	0.50	0.50
$\mu_{VBF}$	$1.00^{+0.33}_{-0.30}$	0.10	0.50	1.00
$\mu_{VBF}$	$1.00^{+0.36}_{-0.33}$	0.10	1.00	0.10
$\mu_{VBF}$	$1.00^{+0.34}_{-0.31}$	0.10	1.00	0.50
$\mu_{VBF}$	$1.00^{+0.33}_{-0.30}$	0.10	1.00	1.00
$\mu_{VBF}$	$1.00^{+0.36}_{-0.33}$	0.50	0.10	0.10
$\mu_{VBF}$	$1.00^{+0.34}_{-0.31}$	0.50	0.10	0.50
$\mu_{VBF}$	$1.00^{+0.33}_{-0.30}$	0.50	0.10	1.00
$\mu_{VBF}$	$1.00^{+0.36}_{-0.33}$	0.50	0.50	0.10
$\mu_{VBF}$	$1.00^{+0.34}_{-0.31}$	0.50	0.50	0.50
$\mu_{VBF}$	$1.00^{+0.33}_{-0.30}$	0.50	0.50	1.00
$\mu_{VBF}$	$1.00^{+0.36}_{-0.33}$	0.50	0.50	0.10
$\mu_{VBF}$	$1.00^{+0.34}_{-0.31}$	0.50	0.50	0.50
$\mu_{VBF}$	$1.00^{+0.33}_{-0.30}$	0.50	0.50	1.00
$\mu_{VBF}$	$1.00^{+0.36}_{-0.33}$	0.50	1.00	0.10
$\mu_{VBF}$	$1.00^{+0.34}_{-0.31}$	0.50	1.00	0.50
$\mu_{VBF}$	$1.00^{+0.33}_{-0.30}$	0.50	1.00	1.00
$\mu_{VBF}$	$1.00^{+0.36}_{-0.33}$	1.00	0.10	0.10
$\mu_{VBF}$	$1.00^{+0.34}_{-0.31}$	1.00	0.10	0.50
$\mu_{VBF}$	$1.00^{+0.33}_{-0.30}$	1.00	0.10	1.00
$\mu_{VBF}$	$1.00^{+0.36}_{-0.33}$	1.00	0.50	0.10
$\mu_{VBF}$	$1.00^{+0.34}_{-0.31}$	1.00	0.50	0.50
$\mu_{VBF}$	$1.00^{+0.33}_{-0.30}$	1.00	0.50	1.00
$\mu_{VBF}$	$1.00^{+0.36}_{-0.33}$	1.00	1.00	0.10
$\mu_{VBF}$	$1.00^{+0.34}_{-0.31}$	1.00	1.00	0.50
$\mu_{VBF}$	$1.00^{+0.33}_{-0.30}$	1.00	1.00	1.00
$\mu_{VBF}$	$1.00^{+0.36}_{-0.33}$	1.00	1.00	1.00

The measured variation of the VBF yield in the signal region with respect to the nominal conditions corresponds to the sensitivity to event-migration across categories in simulation due to systematic uncertainties in the predictions.

*CHAPTER 6. BACKGROUNDS AND SYSTEMATICS*

**6.1.5 Fake backgrounds**

**6.2 Systematic uncertainties**

## CHAPTER 6. BACKGROUNDS AND SYSTEMATICS

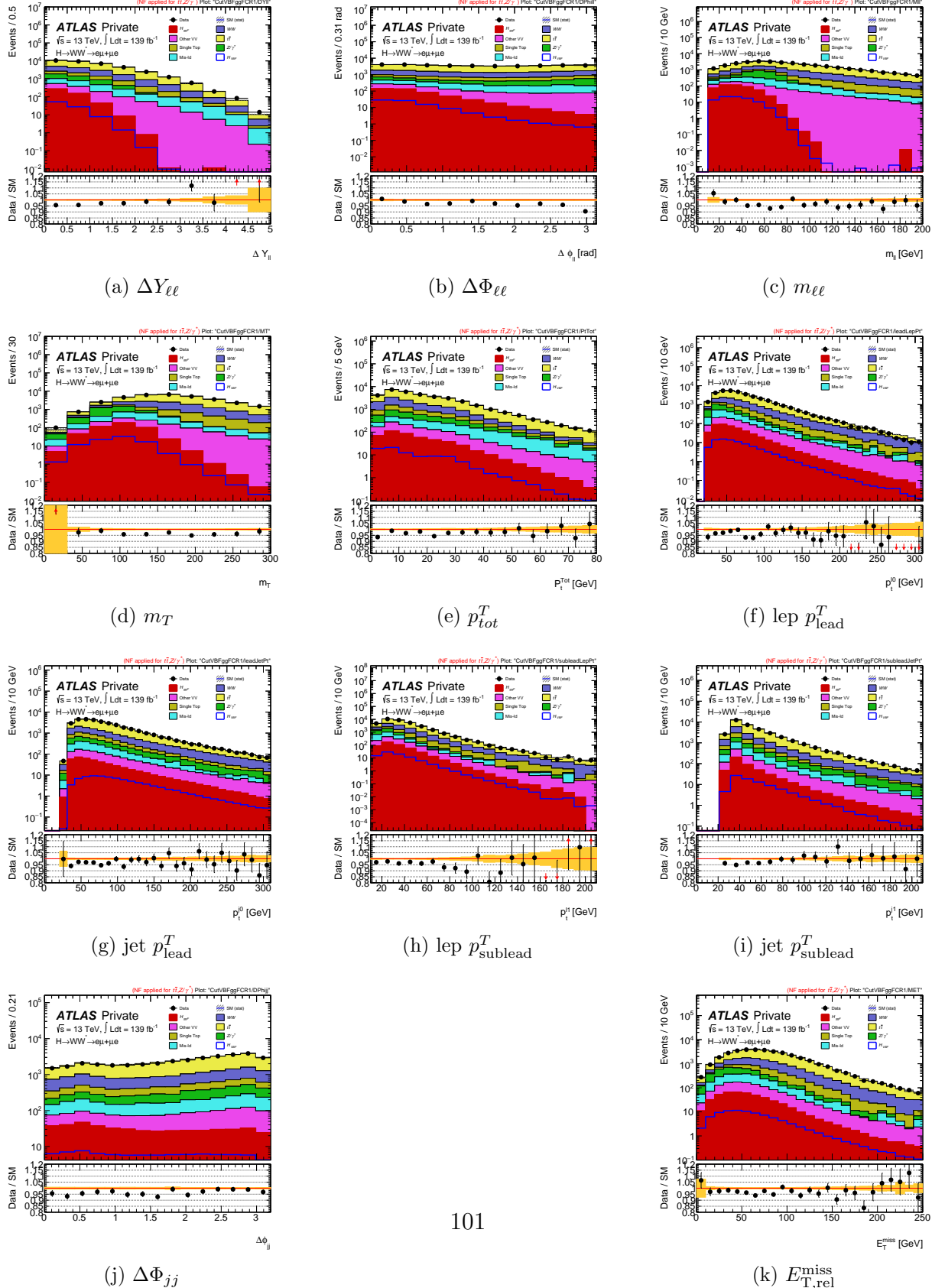


Figure 6.14: Distributions of  $\Delta Y_{\ell\ell}$ ,  $\Delta \Phi_{\ell\ell}$ ,  $m_{\ell\ell}$ ,  $m_T$ ,  $p_{\ell}^T$ , lep  $p_{\ell}^T$  sublead, jet  $p_{\ell}^T$  lead, jet  $p_{\ell}^T$  sublead,  $\Delta \Phi_{jj}$ , and  $E_{T,\text{rel}}^{\text{miss}}$  in the ggF CR1 used as input to the BDT discriminating ggF from backgrounds.

## CHAPTER 6. BACKGROUNDS AND SYSTEMATICS

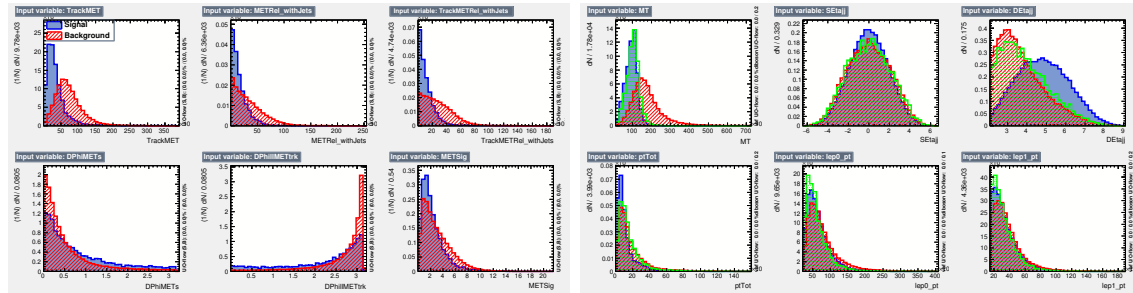


Figure 6.15: Distributions of input variables to ggFCR1 BDT. Samples are unweighted and normalized to even numbers of background and signal events. Signal represents ggF and background all other samples.

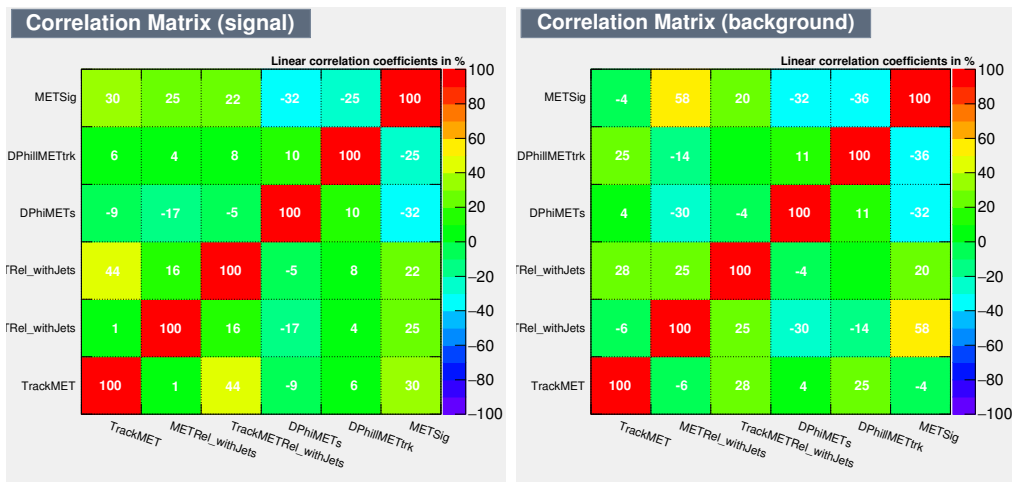


Figure 6.16: Correlations of input variables to ggFCR1 BDT. Signal represents ggF and background all other samples.

## CHAPTER 6. BACKGROUNDS AND SYSTEMATICS

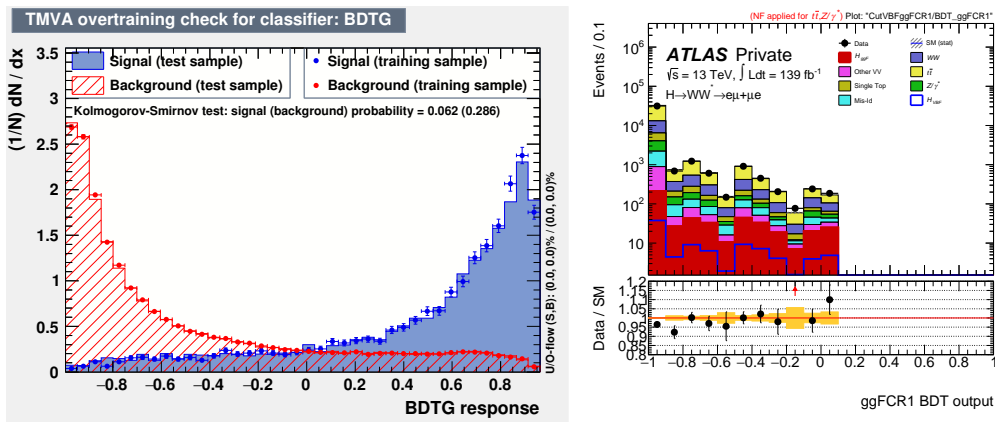


Figure 6.17: Unweighted, normalized samples of ggF (signal) and all other samples (background) plotted over BDT output distribution on left, overlaid testing and training samples shown. Right, full weighted samples of ggF signal and all other backgrounds plotted over BDT output distribution after ggF CR 1.

## CHAPTER 6. BACKGROUNDS AND SYSTEMATICS

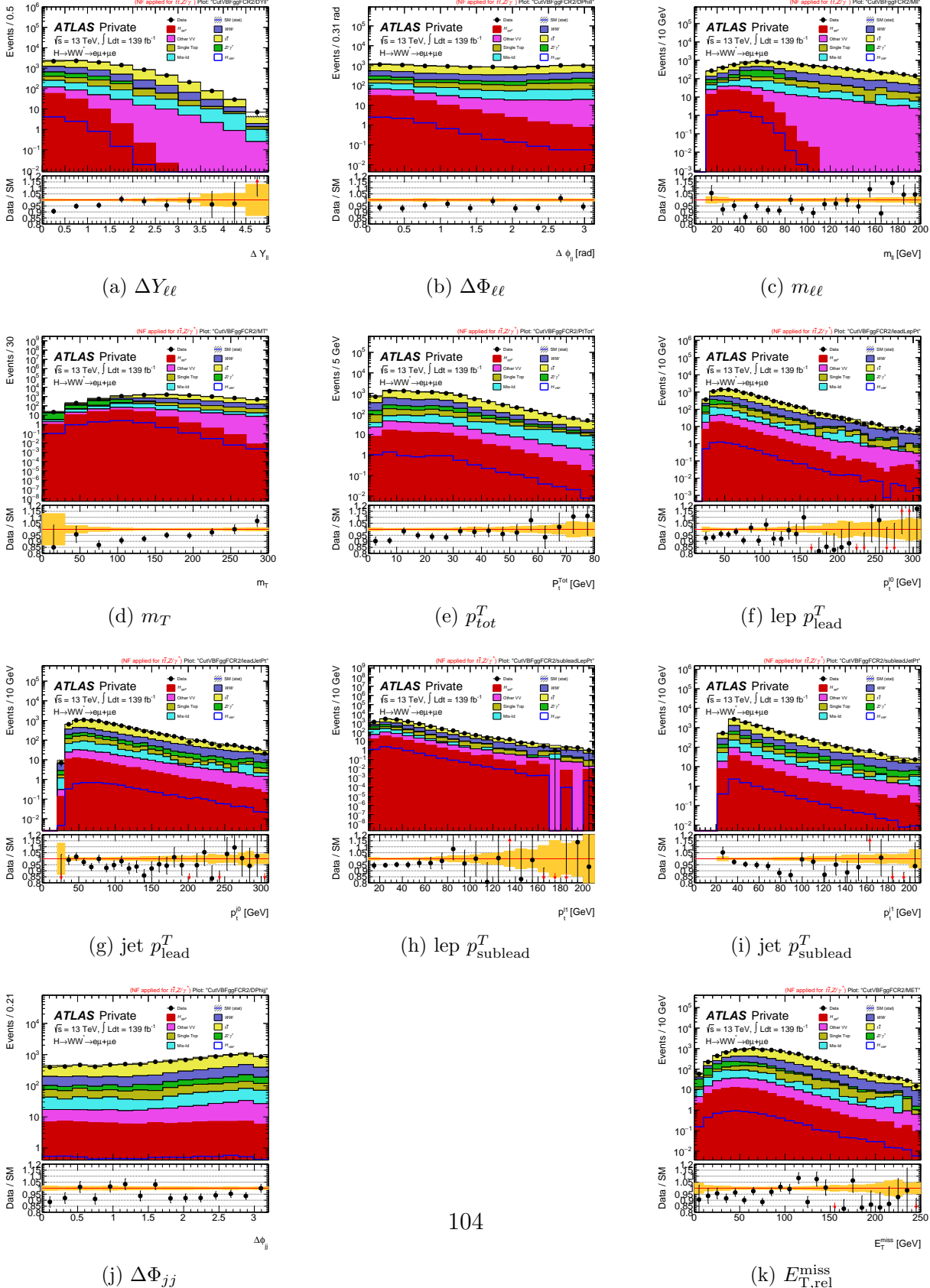


Figure 6.18: Distributions of  $\Delta Y_{\ell\ell}$ ,  $\Delta \Phi_{\ell\ell}$ ,  $m_{\ell\ell}$ ,  $m_T$ ,  $p_{\ell\ell}^T$ , lep  $p_{\text{sublead}}^T$ , jet  $p_{\text{sublead}}^T$ , jet  $p_{\text{lead}}^T$ ,  $\Delta \Phi_{jj}$ , and  $E_{\text{T},\text{rel}}^{\text{miss}}$  in the ggF CR2 used as input to the BDT discriminating ggF from backgrounds.

## CHAPTER 6. BACKGROUNDS AND SYSTEMATICS

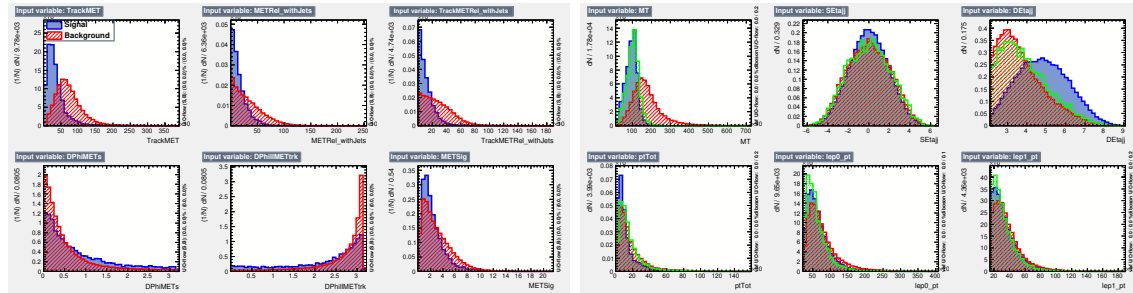


Figure 6.19: Distributions of input variables to ggFCR2 BDT. Samples are unweighted and normalized to even numbers of background and signal events. Signal represents ggF and background all other samples.

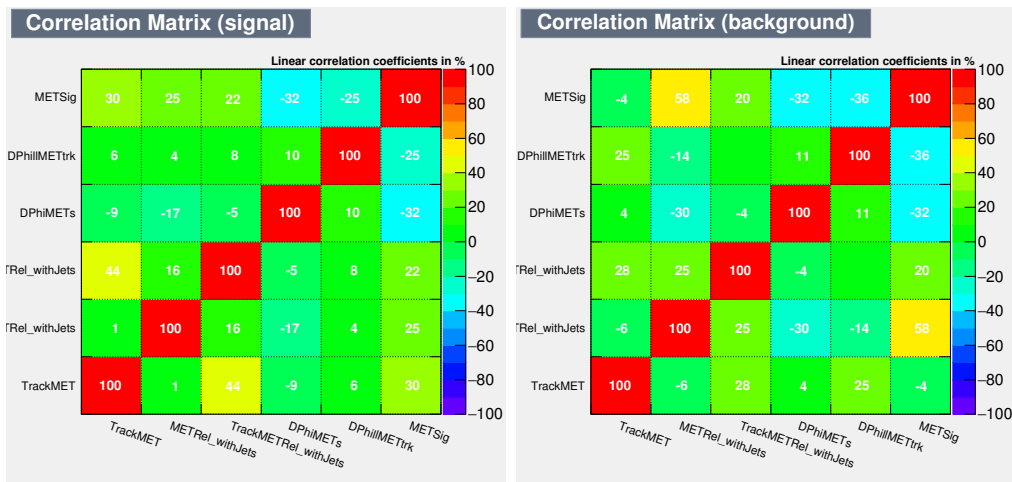


Figure 6.20: Correlations of input variables to ggFCR2 BDT. Signal represents ggF and background all other samples.

## CHAPTER 6. BACKGROUNDS AND SYSTEMATICS

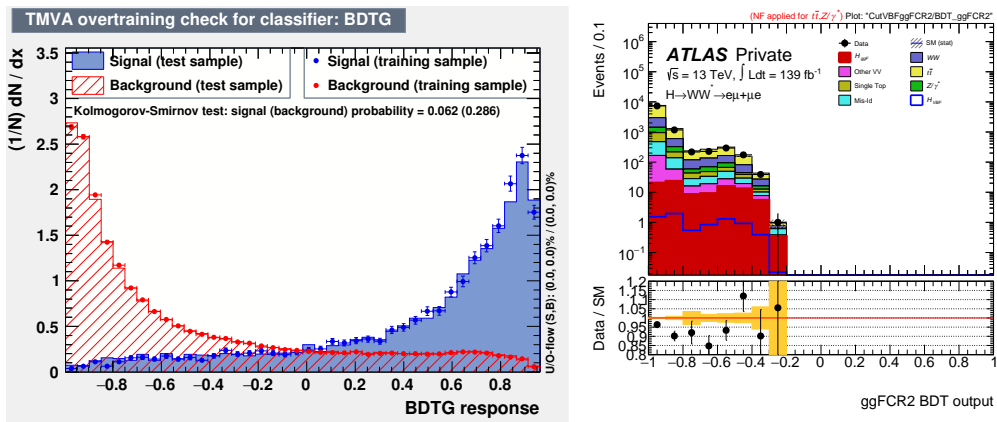


Figure 6.21: Unweighted, normalized samples of ggF (signal) and all other samples (background) plotted over BDT output distribution on left, overlaid testing and training samples shown. Right, full weighted samples of ggF signal and all other backgrounds plotted over BDT output distribution after ggF CR 2.

## CHAPTER 6. BACKGROUNDS AND SYSTEMATICS

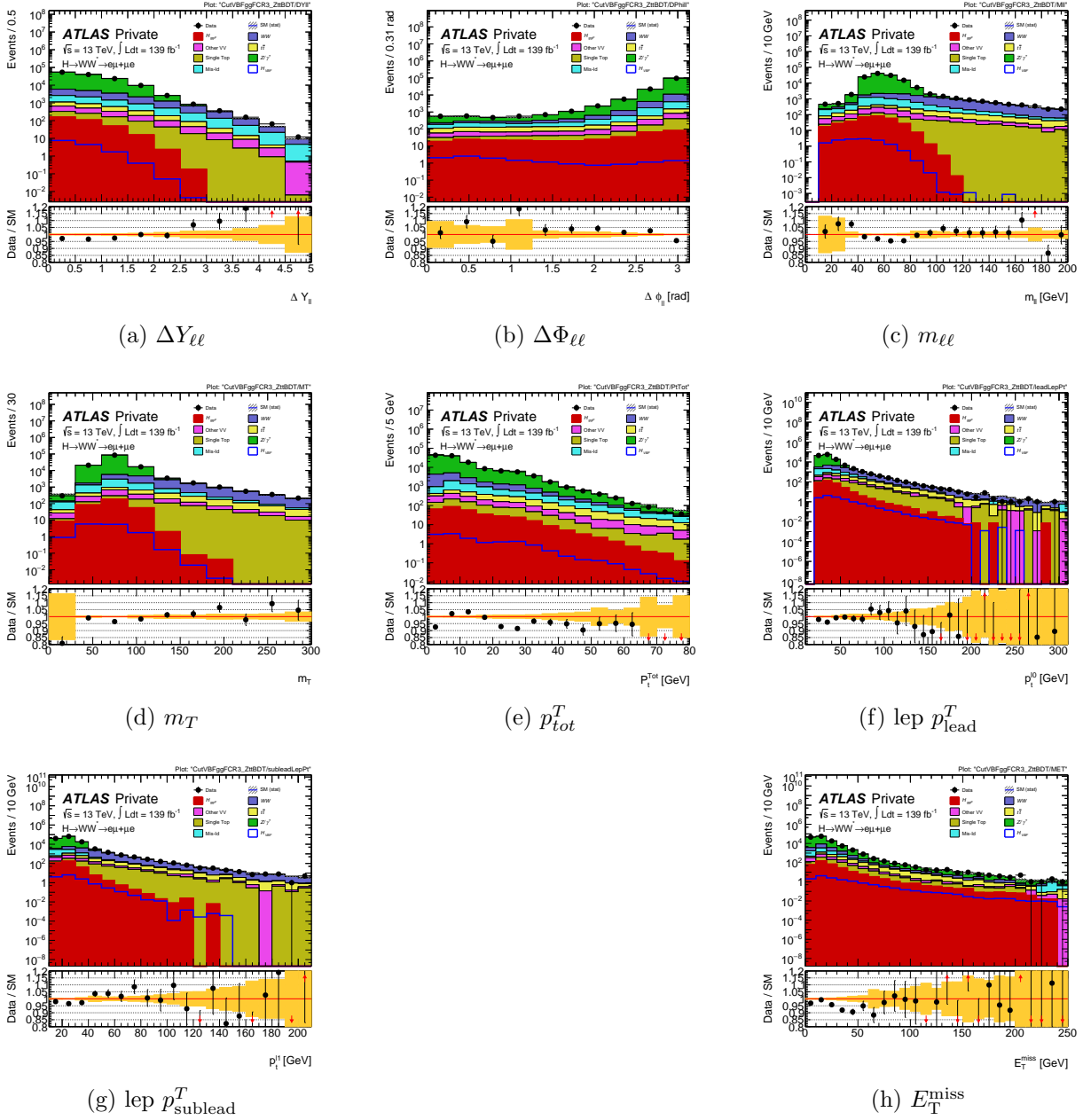


Figure 6.22: Distributions of  $\Delta Y_{\ell\ell}$ ,  $\Delta\Phi_{\ell\ell}$ ,  $m_{\ell\ell}$ ,  $m_T$ ,  $p_T^{\text{tot}}$ , lep  $p_{\text{lead}}^T$ , lep  $p_{\text{sublead}}^T$ , and  $E_{\text{T}}^{\text{miss}}$  in the ggF CR3 used as input to the BDT discriminating ggF from all other samples.

## CHAPTER 6. BACKGROUNDS AND SYSTEMATICS

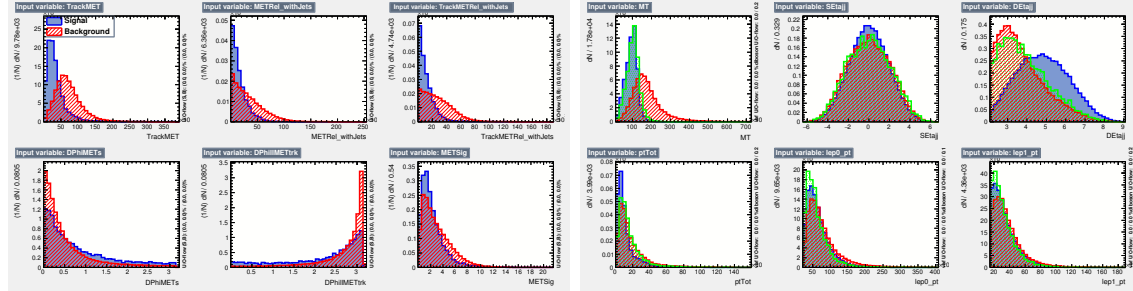


Figure 6.23: Distributions of input variables to ggFCR3 BDT. Samples are unweighted and normalized to even numbers of background and signal events. Signal represents ggF and background all other samples.

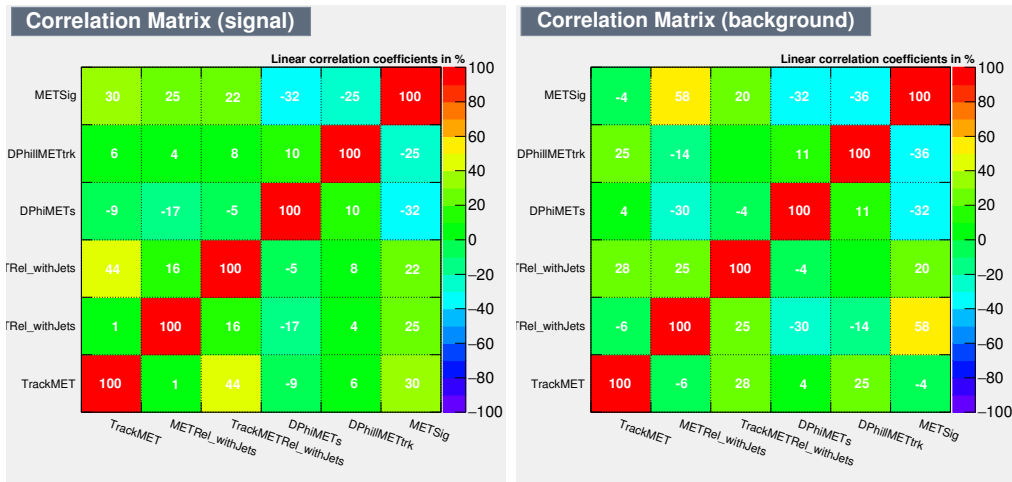


Figure 6.24: Correlations of input variables to ggFCR3 BDT. Signal represents ggF and background all other samples.

## CHAPTER 6. BACKGROUNDS AND SYSTEMATICS

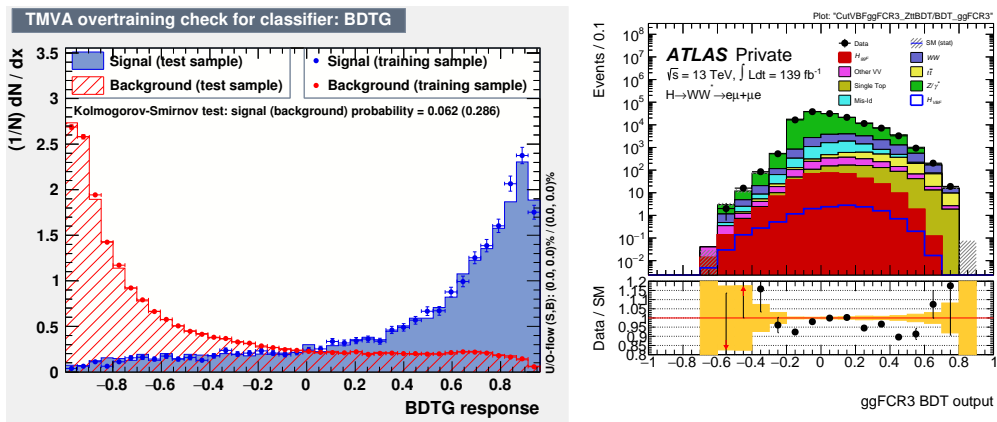


Figure 6.25: Unweighted, normalized samples of ggF (signal) and all other samples (background) plotted over BDT output distribution on left, overlaid testing and training samples shown. Right, full weighted samples of ggF signal and all other backgrounds plotted over BDT output distribution after ggF CR 3.

# Chapter 7

## Results

Thus far I have outlined all reconstruction-level inputs to our analysis including event selection, all backgrounds and their estimation methods, and all systematic uncertainties. Each of these components is critical to our final result and this section will focus on the methods used to extract differential cross-section measurements and their uncertainties from the signal and control regions previously defined.

### 7.1 Statistical analysis

#### 7.1.1 Likelihood functions

This analysis rests on the estimation of a parameter  $\mu$  which describes the statistical significance of our signal yield relative to its standard model prediction and in this particular analysis defines the signal cross-section. We build a likelihood function  $\mathcal{L}(\mu, \Theta)$  where the signal strength  $\mu$  is a parameter of interest (POI) and nuisance parameters (NPs)  $\Theta = \Theta_a, \Theta_b, \dots$  represent all relevant uncertainties. None of these values are known a priori so the likelihood is built to represent the probability of particular values for the POI and NPs.

## CHAPTER 7. RESULTS

The analysis uses a maximum likelihood estimator to find the inputs which maximize the likelihood (or equivalently and more mathematically tractable, minimize the negative log of the likelihood). Here I will briefly outline how a likelihood function can incorporate regions of interest, this discussion uses [43] as a guide. First, the Poisson distribution  $\mathcal{P}(n|\lambda)$  describes the probability of  $n$  events with a true unknown yield  $\lambda$ :

$$\mathcal{P}(n|\lambda) = \lambda^n \frac{e^{-\lambda}}{n!} \quad (7.1)$$

Next we can define a variable observable  $x$  with probability density  $f(x)$  hence with  $n$  events the probability density of each is multiplied. The likelihood of  $\lambda$  can now be written

$$\mathcal{L}(\lambda) = \mathcal{P}(n|\lambda) \prod_{\text{event}}^n f(x) \quad (7.2)$$

Our likelihood also must take into account multiple regions (the signal region as well as the control regions) and so these likelihoods are multiplied together with their own distinct Poisson distributions

$$\mathcal{L}(\lambda) = \prod_r^{\text{regions}} (\mathcal{P}(n_r|\lambda_r) \prod_{\text{event}}^n f(x)) \quad (7.3)$$

A simultaneous fit maximizes this likelihood function and so produces signal strengths  $\lambda$  for each free parameter simultaneously. The  $\lambda$  values here represent predicted yields where  $\lambda_{r,b} = \mu\lambda_{\text{sig}} + \lambda_{\text{bkg}}$ . Maximizing the overall likelihood is made simpler by applying the natural logarithm (as the products between Poisson distributions become summations) and negating the likelihood, so as to take advantage of minimizing software.

Particle physics defines discovery with rigorous standards using hypothesis testing. The null hypothesis is considered  $\mu = 0$  and is considered “background-only” while the alternative hypothesis is that there is a signal above the background. The probability that the null

## *CHAPTER 7. RESULTS*

hypothesis is rejected (or that the signal is discovered) is defined as a  $p$ -value. The  $p$ -value can be converted to a number of Gaussian standard deviations and in high energy physics three  $\sigma$  significance (or a  $p$ -value of  $1.35 \times 10^{-3}$ ) shows evidence while a five  $\sigma$  result ( $p$ -value  $2.87 \times 10^{-7}$ ) is considered a discovery.

### **7.2 Unfolding**

### **7.3 Results and future measurements**

# **Chapter 8**

## **Conclusions**

# Bibliography

- [1] M. Tanabashi, K. Hagiwara, K. Hikasa, K. Nakamura, Y. Sumino, F. Takahashi, J. Tanaka, K. Agashe, G. Aielli, C. Amsler, M. Antonelli, D. M. Asner, H. Baer, Sw. Banerjee, R. M. Barnett, T. Basaglia, C. W. Bauer, J. J. Beatty, V. I. Belousov, J. Beringer, S. Bethke, A. Bettini, H. Bichsel, O. Biebel, K. M. Black, E. Blucher, O. Buchmuller, V. Burkert, M. A. Bychkov, R. N. Cahn, M. Carena, A. Cecucci, A. Cerri, D. Chakraborty, M.-C. Chen, R. S. Chivukula, G. Cowan, O. Dahl, G. D'Ambrosio, T. Damour, D. de Florian, A. de Gouv  a, T. DeGrand, P. de Jong, G. Dissertori, B. A. Dobrescu, M. D'Onofrio, M. Doser, M. Drees, H. K. Dreiner, D. A. Dwyer, P. Eerola, S. Eidelman, J. Ellis, J. Erler, V. V. Ezhela, W. Fettscher, B. D. Fields, R. Firestone, B. Foster, A. Freitas, H. Gallagher, L. Garren, H.-J. Gerber, G. Gerbier, T. Gershon, Y. Gershtein, T. Gherghetta, A. A. Godizov, M. Goodman, C. Grab, A. V. Gritsan, C. Grojean, D. E. Groom, M. Grunewald, A. Gurtu, T. Gutsche, H. E. Haber, C. Hanhart, S. Hashimoto, Y. Hayato, K. G. Hayes, A. Hebecker, S. Heinemeyer, B. Heltsley, J. J. Hern  ndez-Rey, J. Hisano, A. H  cker, J. Holder, A. Holtkamp, T. Hyodo, K. D. Irwin, K. F. Johnson, M. Kado, M. Karliner, U. F. Katz, S. R. Klein, E. Klemp, R. V. Kowalewski, F. Krauss, M. Kreps, B. Krusche, Yu. V. Kuyanov, Y. Kwon, O. Lahav, J. Laiho, J. Lesgourgues, A. Liddle, Z. Ligeti, C.-J. Lin, C. Lippmann, T. M. Liss, L. Littenberg, K. S. Lugovsky, S. B. Lugovsky, A. Lusiani, Y. Makida,

## BIBLIOGRAPHY

F. Maltoni, T. Mannel, A. V. Manohar, W. J. Marciano, A. D. Martin, A. Massoni, J. Matthews, U.-G. Meißner, D. Milstead, R. E. Mitchell, K. Mönig, P. Molaro, F. Moortgat, M. Moskovic, H. Murayama, M. Narain, P. Nason, S. Navas, M. Neubert, P. Nevski, Y. Nir, K. A. Olive, S. Pagan Griso, J. Parsons, C. Patrignani, J. A. Peacock, M. Pennington, S. T. Petcov, V. A. Petrov, E. Pianori, A. Piepke, A. Pomarol, A. Quadt, J. Rademacker, G. Raffelt, B. N. Ratcliff, P. Richardson, A. Ringwald, S. Roesler, S. Rolli, A. Romanouk, L. J. Rosenberg, J. L. Rosner, G. Rybka, R. A. Ryutin, C. T. Sachrajda, Y. Sakai, G. P. Salam, S. Sarkar, F. Sauli, O. Schneider, K. Scholberg, A. J. Schwartz, D. Scott, V. Sharma, S. R. Sharpe, T. Shutt, M. Silari, T. Sjöstrand, P. Skands, T. Skwarnicki, J. G. Smith, G. F. Smoot, S. Spanier, H. Spieler, C. Spiering, A. Stahl, S. L. Stone, T. Sumiyoshi, M. J. Syphers, K. Terashi, J. Terning, U. Thoma, R. S. Thorne, L. Tiator, M. Titov, N. P. Tkachenko, N. A. Tornqvist, D. R. Tovey, G. Valencia, R. Van de Water, N. Varelas, G. Venanzoni, L. Verde, M. G. Vincenter, P. Vogel, A. Vogt, S. P. Wakely, W. Walkowiak, C. W. Walter, D. Wands, D. R. Ward, M. O. Wascko, G. Weiglein, D. H. Weinberg, E. J. Weinberg, M. White, L. R. Wiencke, S. Willocq, C. G. Wohl, J. Womersley, C. L. Woody, R. L. Workman, W.-M. Yao, G. P. Zeller, O. V. Zenin, R.-Y. Zhu, S.-L. Zhu, F. Zimmermann, P. A. Zyla, J. Anderson, L. Fuller, V. S. Lugovsky, and P. Schaffner. Review of particle physics. *Phys. Rev. D*, 98:030001, Aug 2018.

- [2] F. Halzen and A. Martin. *Quarks and Leptons: An Introductory Course in Modern Particle Physics*. 1984.
- [3] John Ellis. Higgs Physics. (KCL-PH-TH-2013-49. KCL-PH-TH-2013-49. LCTS-2013-36. CERN-PH-TH-2013-315):117–168. 52 p, Dec 2013. 52 pages, 45 figures, Lectures

## BIBLIOGRAPHY

presented at the ESHEP 2013 School of High-Energy Physics, to appear as part of the proceedings in a CERN Yellow Report.

- [4] Jonathan M. Butterworth, Guenther Dissertori, and Gavin P. Salam. Hard Processes in Proton-Proton Collisions at the Large Hadron Collider. *Ann. Rev. Nucl. Part. Sci.*, 62:387–405, 2012.
- [5] John M. Campbell, J. W. Huston, and W. J. Stirling. Hard Interactions of Quarks and Gluons: A Primer for LHC Physics. *Rept. Prog. Phys.*, 70:89, 2007.
- [6] W.J. Stirling. Private Communication... 2018.
- [7] Abdelhak Djouadi. The Anatomy of electro-weak symmetry breaking. I: The Higgs boson in the standard model. *Phys. Rept.*, 457:1–216, 2008.
- [8]
- [9] Jon Butterworth et al. PDF4LHC recommendations for LHC Run II. *J. Phys.*, G43:023001, 2016.
- [10] Georges Aad et al. Observation of a new particle in the search for the Standard Model Higgs boson with the ATLAS detector at the LHC. *Phys. Lett.*, B716:1–29, 2012.
- [11] Tom W. B. Kibble. The Standard Model of Particle Physics. 2014.
- [12] N.R. Council, D.E.P. Sciences, B.P. Astronomy, and C.E.P. Physics. *Elementary-Particle Physics: Revealing the Secrets of Energy and Matter*. Physics in a New Era: A Series. National Academies Press, 1998.

## BIBLIOGRAPHY

- [13] Georges Aad et al. Combined measurements of Higgs boson production and decay using up to  $80 \text{ fb}^{-1}$  of proton-proton collision data at  $\sqrt{s} = 13 \text{ TeV}$  collected with the ATLAS experiment. *Phys. Rev.*, D101(1):012002, 2020.
- [14] Georges Aad et al. Measurement of fiducial differential cross sections of gluon-fusion production of Higgs bosons decaying to  $\text{WW}^* \rightarrow e\nu\mu\nu$  with the ATLAS detector at  $\sqrt{s} = 8 \text{ TeV}$ . *JHEP*, 08:104, 2016.
- [15] L Rossi. Superconductivity: Its Role, Its Success and Its Setbacks in the Large Hadron Collider of CERN. *Supercond. Sci. Technol.*, 23(CERN-ATS-2010-006):034001. 27 p, Jan 2010.
- [16] Rende Steerenberg. Lhc report: Protons: mission accomplished, 2018.
- [17] M. Aaboud, G. Aad, B. Abbott, O. Abdinov, B. Abelos, D.K. Abhayasinghe, S.H. Abidi, O.S. AbouZeid, N.L. Abraham, H. Abramowicz, and et al. Measurements of gluon-gluon fusion and vector-boson fusion higgs boson production cross-sections in the  $h \rightarrow ww^* \rightarrow e\nu\mu\nu$  decay channel in  $pp$  collisions at  $\sqrt{(s)}=13\text{tev}$  with the atlas detector. *Physics Letters B*, 789:508–529, Feb 2019.
- [18] M. Aaboud, G. Aad, B. Abbott, O. Abdinov, B. Abelos, S. H. Abidi, O. S. AbouZeid, N. L. Abraham, H. Abramowicz, and et al. Measurement of the higgs boson coupling properties in the  $h \rightarrow zz^* \rightarrow 4\ell$  decay channel at  $\sqrt{s} = 13 \text{ tev}$  with the atlas detector. *Journal of High Energy Physics*, 2018(3), Mar 2018.
- [19] M. Aaboud, G. Aad, B. Abbott, O. Abdinov, B. Abelos, S. H. Abidi, O. S. AbouZeid, N. L. Abraham, H. Abramowicz, H. Abreu, and et al. Measurements of higgs boson properties in the diphoton decay channel with  $36 \text{ fb}^{-1}$  of  $pp$  collision data at  $\sqrt{s} = 13 \text{ tev}$  with the atlas detector. *Physical Review D*, 98(5), Sep 2018.

## BIBLIOGRAPHY

- [20] M. Aaboud, G. Aad, B. Abbott, O. Abdinov, B. Abelos, D. K. Abhayasinghe, S. H. Abidi, O. S. AbouZeid, N. L. Abraham, H. Abramowicz, and et al. Cross-section measurements of the higgs boson decaying into a pair of  $\tau$ -leptons in proton-proton collisions at  $\sqrt{s}=13$  tev with the atlas detector. *Physical Review D*, 99(7), Apr 2019.
- [21] Search for squarks and gluinos in final states with jets and missing transverse momentum using  $139 \text{ fb}^{-1}$  of  $\sqrt{s} = 13 \text{ TeV}$   $pp$  collision data with the ATLAS detector. Technical Report ATLAS-CONF-2019-040, CERN, Geneva, Aug 2019.
- [22] CERN. A new schedule for the lhc and its successor, 2019.
- [23] M. Benedikt, P. Collier, V. Mertens, J. Poole, and K. Schindl. LHC Design Report. 3. The LHC injector chain. 2004.
- [24] Radiofrequency cavities. Sep 2012.
- [25] Lyndon Evans. The large hadron collider. *New Journal of Physics*, 9(9):335–335, sep 2007.
- [26] G Aad et al. The ATLAS Experiment at the CERN Large Hadron Collider. *JINST*, 3:S08003. 437 p, 2008. Also published by CERN Geneva in 2010.
- [27] ATLAS Collaboration. Technical Design Report for the ATLAS Inner Tracker Strip Detector. Technical Report CERN-LHCC-2017-005. ATLAS-TDR-025, CERN, Geneva, Apr 2017.
- [28] Jet global sequential corrections with the ATLAS detector in proton-proton collisions at  $\text{sqrt}(s) = 8 \text{ TeV}$ . Technical Report ATLAS-CONF-2015-002, CERN, Geneva, Mar 2015.

## BIBLIOGRAPHY

- [29] Morad Aaboud et al. Jet reconstruction and performance using particle flow with the ATLAS Detector. *Eur. Phys. J.*, C77(7):466, 2017.
- [30] JET ETmiss group. Public plots, 2019.
- [31] Matteo Cacciari, Gavin P. Salam, and Gregory Soyez. The anti- $k_t$  jet clustering algorithm. *JHEP*, 04:063, 2008.
- [32] Morad Aaboud et al. Determination of jet calibration and energy resolution in proton-proton collisions at  $\sqrt{s} = 8$  TeV using the ATLAS detector. 2019.
- [33] Object-based missing transverse momentum significance in the ATLAS detector. Technical Report ATLAS-CONF-2018-038, CERN, Geneva, Jul 2018.
- [34] Morad Aaboud et al. Performance of missing transverse momentum reconstruction with the ATLAS detector using proton-proton collisions at  $\sqrt{s} = 13$  TeV. *Eur. Phys. J.*, C78(11):903, 2018.
- [35] ATLAS Collaboration. 14(12):P12006–P12006, dec 2019.
- [36] J. Illingworth and J. Kittler. A survey of the hough transform. *Computer Vision, Graphics, and Image Processing*, 44(1):87 – 116, 1988.
- [37] Performance of the ATLAS Silicon Pattern Recognition Algorithm in Data and Simulation at  $\sqrt{s} = 7$  TeV. Technical Report ATLAS-CONF-2010-072, CERN, Geneva, Jul 2010.
- [38] G. Aad, B. Abbott, J. Abdallah, O. Abdinov, B. Abelos, R. Aben, M. Abolins, O. S. AbouZeid, N. L. Abraham, and et al. Muon reconstruction performance of the atlas

## BIBLIOGRAPHY

detector in proton–proton collision data at

$$\sqrt{s}$$

$s = 13$  tev. *The European Physical Journal C*, 76(5), May 2016.

- [39] Georges Aad et al. Measurement of the muon reconstruction performance of the ATLAS detector using 2011 and 2012 LHC proton–proton collision data. Measurement of the muon reconstruction performance of the ATLAS detector using 2011 and 2012 LHC proton-proton collision data. *Eur. Phys. J. C*, 74(CERN-PH-EP-2014-151. CERN-PH-EP-2014-151):3130. 34 p, Jul 2014. Comments: 21 pages plus author list + cover pages (34 pages total), 21 figures, 2 tables, submitted to EPJC, All figures including auxiliary figures are available at <http://atlas.web.cern.ch/Atlas/GROUPS/PHYSICS/PAPERS/PERF-2014-05/>.
- [40] Johannes Josef Junggeburth. Muon identification and reconstruction efficiencies in full Run-2 dataset. Technical Report ATL-COM-PHYS-2019-1001, CERN, Geneva, Aug 2019.
- [41] G. Aad, B. Abbott, J. Abdallah, A. A. Abdelalim, A. Abdesselam, O. Abdinov, B. Abi, M. Abolins, H. Abramowicz, and et al. Jet energy measurement with the atlas detector in proton-proton collisions at  $\sqrt{s} = 7$  TeV. *The European Physical Journal C*, 73(3), Mar 2013.
- [42] Miha Zgubič, Johannes Josef Junggeburth, and K. Technical report.
- [43] Kyle Cranmer. Practical statistics for the lhc, 2015.